In situ micro-mechanical characterization and multi-scale modeling of thermo-mechanical properties of micro-architectured tungsten coatings

by
Quan Jiao

A dissertation submitted to The Johns Hopkins University in conformity with the requirements for the degree of Doctor of Philosophy

Baltimore, Maryland
June 2019

Abstract

Micro-architectured refractory metal surfaces have been recently proposed as coatings for extremely high temperature applications and for plasma facing components in the aerospace and energy industries. While ongoing research shows that such micro-architectured coatings are capable of mitigating extreme high thermal loads and withstanding radiation damages, very little is known about their microstructure, thermo-mechanical properties, and failure modes. The gap raises severe concerns for critical usage where structural integrity is of ultimate importance and restricts them from being used in a broader array of applications. In this thesis, we aim to develop a systematic and fundamental understanding of these aspects for tungsten micro-architectured coatings, which have been proposed as potential grid material coatings for ion thrusters.

A combination of advanced microstructural characterization, elevated temperature *in situ* scanning electron microscopy (SEM) micro-mechanical experiments, and image-based crystal plasticity finite element method (CPFEM) simulations are utilized to address these issues. It is shown that the micro-architectured tungsten coat-

ings are composed of columnar grains with many pre-existing voids preferentially distribute along the grain boundaries. Although the voids can alleviate thermal stresses by allowing free expansion/contraction of the coating, their effect on the mechanical properties remains unknown and the mechanical performance of the coating needs to be quantified.

From *in situ* micro-compression experiments performed from 293K to 673 K, a strong temperature dependence of strength and deformation/failure mode were observed, with a characteristic temperature between 573K and 673K for brittle-to-ductile transition. Below this range of temperature, the material is very brittle with intergranular fracture and buckling of each individual columnar grain being the predominant deformation mode, which is strongly influenced by the pre-existing voids. With increasing temperature, the strength decreases sharply, at 673 K, the catastrophic failure transitions to a steady hardening response, and the structural integrity is maintained up to 15% of engineering strain. A physics-based model is then proposed to the predict strength of the coating as a function of temperature and grain size. The CPFEM simulations incorporated with a cohesive zone model (CZM) successfully capture the deformation mode transition and further employed to explore the microstructure-property relations. Our simulations indicate the variation in the crystallographic orientation of the tested micropillars primarily contribute to the observed scatter in the experimentally observed of flow stress and fracture behavior.

This work provides experimental evidence that the micro-architectured tungsten

ABSTRACT

coatings possess a combination of excellent mechanical strength, reduced internal thermal stresses, and dramatically improved defect tolerance capability, which is ideal for high temperature applications. Moreover, the computational framework presented here demonstrates great potential to identify and prioritize the promising microstructrual parameters, which eventually accelerate the future development of such coatings.

Thesis Reader: Prof. Jaafar A. El-Awady (advisor), Prof. Somnath. Ghosh and Prof. Kevin J. Hemker

Acknowledgments

I would like to express my gratitude to the people who have guided, encouraged, and inspired me to fulfill my doctoral research.

First, I would like to express my sincere gratitude to my PhD advisor, Professor Jaafar El-Awady, for offering me unwavering support and heartfelt guidance through the last six years. He is not just a friend, a mentor, but also my role model. His vision, passion, and courage toward formidable problems have a profound influence on me, which will be the source of strength in my future quest for knowledge.

Besides my advisor, I would like to thank Professor Kevin Hemker and Professor Somnath Ghosh for reading my thesis and serving on my thesis committee. A lot of essential techniques, knowledge and ideas adopted in my research could be traced back to their awesome lectures on deformation mechanisms, microstructural characterization, and nonlinear FEM. I feel extremely fortunate to be able to learn the fundamentals from them, develop my own understanding, and finally present my work in front of them.

I would also like to express my appreciation to my lab mates and friends at JHU. I would like to special thank Steven Lavenstein for his assistance with my experimental

work and proofreading my thesis, and Jiahao Cheng for his generosity of for many thoughtful discussions on CPFEM. I am also thankful to Gi-dong Sim and Kelvin (Yuxuan) Xie for their support and guidance. I also would like to thank Meng Zhao, Qing-jie Li, Yejun Gu, and Xiaolong Ma for the many lunches we had together and the many stimulating discussions we had on research and daily life.

I am also grateful to my collaborators, including Professor Peter Liaw from University of Tennessee, Knoxville, Professfor Rajiv Mishra from University of North Texas, as well as their group members. I also would like to thank Professor Ke Lu from Institute of Metal Research, Chinese Academy of Sciences, for his long time encouragement on my scientific career.

Additionally, I would like to acknowledge MARCC administration team for their prompt technical support and all administrative staff in the Department of Mechanical Engineering for their professional assistance.

Finally, I would like to acknowledge the support from the Aerospace Materials for Extreme Environments Program (Program Manager Dr. Ali Sayir) at the U.S. Air Force Office for Scientific Research (AFOSR), through Grant No. FA9550-15-1-0070, to Johns Hopkins University.

Dedication

To my parents, for their endless love and encouragement.

Contents

List of Tables

List of Figures

Chapter 1

Introduction

1.1 Motivation

The reliable performance of materials subjected to extremely high temperature environments is critical for the development of future space exploration missions as well as many other extreme environment technologies. With the revival of NASA space programs (e.g. asteroid-capture mission in 2020s [6], and the 1st manned mission to Mars by the 2030s), electric propulsion and ion thrusters have received renewed attention as cost effective systems that requires less weight than conventional chemical propulsion systems. Ion thrusters provide longer thrust duration per unit weight of propellant, and in particular, plasma ion thrusters exhibit the highest specific impulse among all electric thrusters [7]. Advanced electric propulsion technologies have achieved a hight level of maturity and thus have been used for planet orbiting, ren-

dezvous missions, and sample return missions [8–10]. However, such missions can take 1-10 years and require materials that can withstand radiation damage for this duration of time.

Figure 1.1 shows a schematic of an electrostatic ion thruster. A propellant typically Xenon gas is first injected into the chamber where it is ionized by the bombardment/collision of high energy electrons. Negative charged electrons are emitted from the neutralizer; positive charged ions are extracted and accelerated by a set of positive and negative grids through the electrostatic field. The linear motion of the ions develops a thrust force that propels the spacecraft. During this process, the surface of the ion thruster accelerator grid (the negative grid in Figure 1.1) is where most sever damage is expected. This damage is mostly associated with erosion due to sputtering from direct ion beam impingement and charge-exchange ion bombardment [11, 12]. Therefore, in order to prolong the life expectancies of these thrusters, there is a need for coatings that have low sputter rates and can withstand extreme thermo-mechanical loads while maintaining appropriate structural integrity to assure the integrity of the mission and prolong the life-expectancies of these thrusters.

Refractory metals, such as tungsten (W) and its alloys, are primary candidate materials for coating structural components in extreme thermal and radiation environments. The particular interest in tungsten alloys arises from the fact that they have the highest melting point of all metals ($\sim 3410\,^{\circ}\mathrm{C}$) as well as their high thermal mass, which makes them ideal for radiative cooling [13]. In addition, W shows a

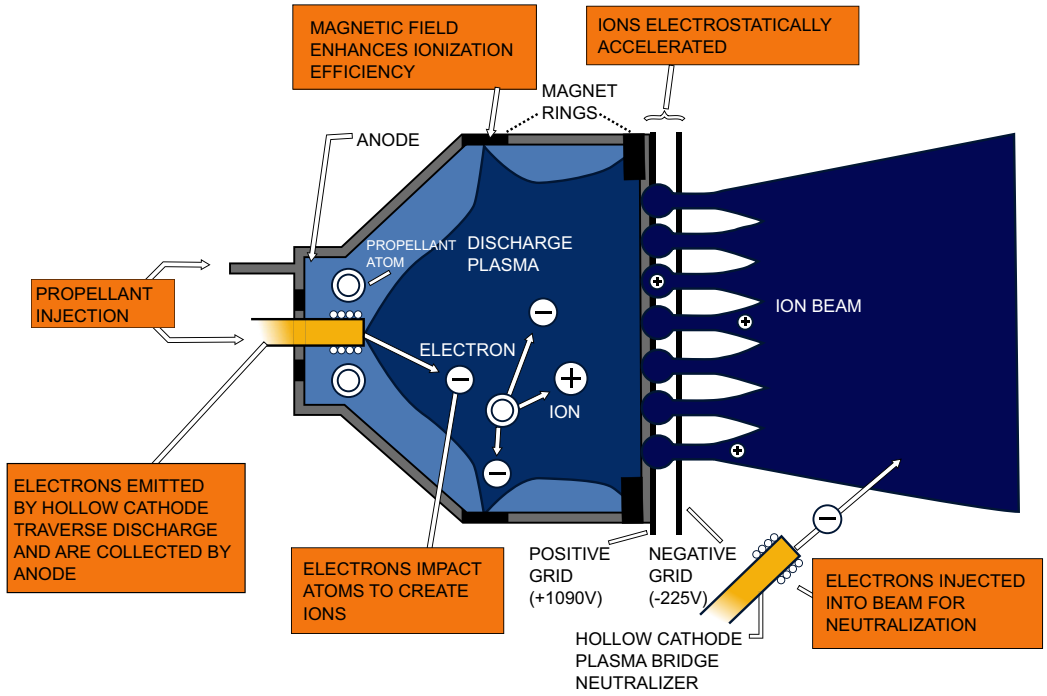

Figure 1.1: A schematic of an electrostatic ion thruster with a brief illustration of the working principle. Image is adopted from Wikipedia *https://en.wiki pedia.org/wiki/Ion_ thruster*

reduced wall erosion due to low physical sputtering rates [14]. Tungsten also demonstrates very high strengths [15]; however, the low ductility of W at room temperature and subsequently the high ductile-to-brittle transition temperature (DBTT) limits its formability. Nevertheless, ongoing studies have shown that the room temperature ductility of W can be improved by adding TiC and/or by processing ultrafine grain W [16, 17].

Nanocrystalline tungsten has been shown to demonstrate high strength, improved ductility, excellent wear resistance, and good thermo-mechanical performance due to its intrinsic microstructure characteristics [18–22]. These favorable properties can be utilized in many potential applications including high-temperature devices [21], as absorbing layers and mirrors in an X-ray field, and as diffusion barriers in semiconductor interconnect layers [22]. However, nanocrystalline tungsten has an inherent instability due to the high volume fraction of grain boundaries. Rapid grain growth and coarsening is typically observed as the temperature increases, which limits the practical applicability of these materials in sustained high temperature applications [23, 24]. A number of studies are currently progressing to develop methods to stabilize the W nanostructure by introducing alloying elements to slow the process of grain growth in these materials [25]. Thus, ultrafine-grained (UFG) metals are a promising candidate since they are a good combination of the desirable properties from nanocrystalline and coarse-grained counterparts. However, it has been shown that the basic thermo-mechanical processing results in grain sizes that are $\sim$ 5-10 µm,

and it is currently not possible to produce with grain size smaller than 1 µm [26].

Recent advances in surface and microstructural engineering have led to the development of micro-architectured (or micro-patterned) refractory metal coatings using chemical vapor deposition (CVD) and/or powder metallurgy techniques [27]. Scanning electron microscope (SEM) micrographs of the top surface of such micro-patterned coatings are shown in Figure 1.2. These CVD coatings are metallurgically bonded to the base material and the size, shape, and density of the grown micropatterned surfaces can be controlled by changing the pressure and temperature settings during the CVD process. It is also possible to deposit these micro-patterned coatings having various geometries in a reproducible manner [2]. This technique can be applied to virtually any refractory metal that can be deposited by CVD (e.g. rhenium, tungsten, tantalum, niobium, molybdenum, and various refractory metal alloys).

One of the advantages of these coatings is that the thermal stresses that develops in these coatings are small as compared to their continuous coating counterparts since the individual micro-patterned structures of these coatings are less confined than the continuous surface coatings, which make them less prone to micro-cracking. While ongoing research shows that such surfaces are capable of mitigating high thermal loads [28], there is very little known about the microstructure of these micro-patterned structures, their thermo-mechanical properties, deformation, and subsequent failure.

Another advantages of such coatings over their flat surface counterparts is that the unique architecture results in a large surface to volume ratio, which aids in vol-

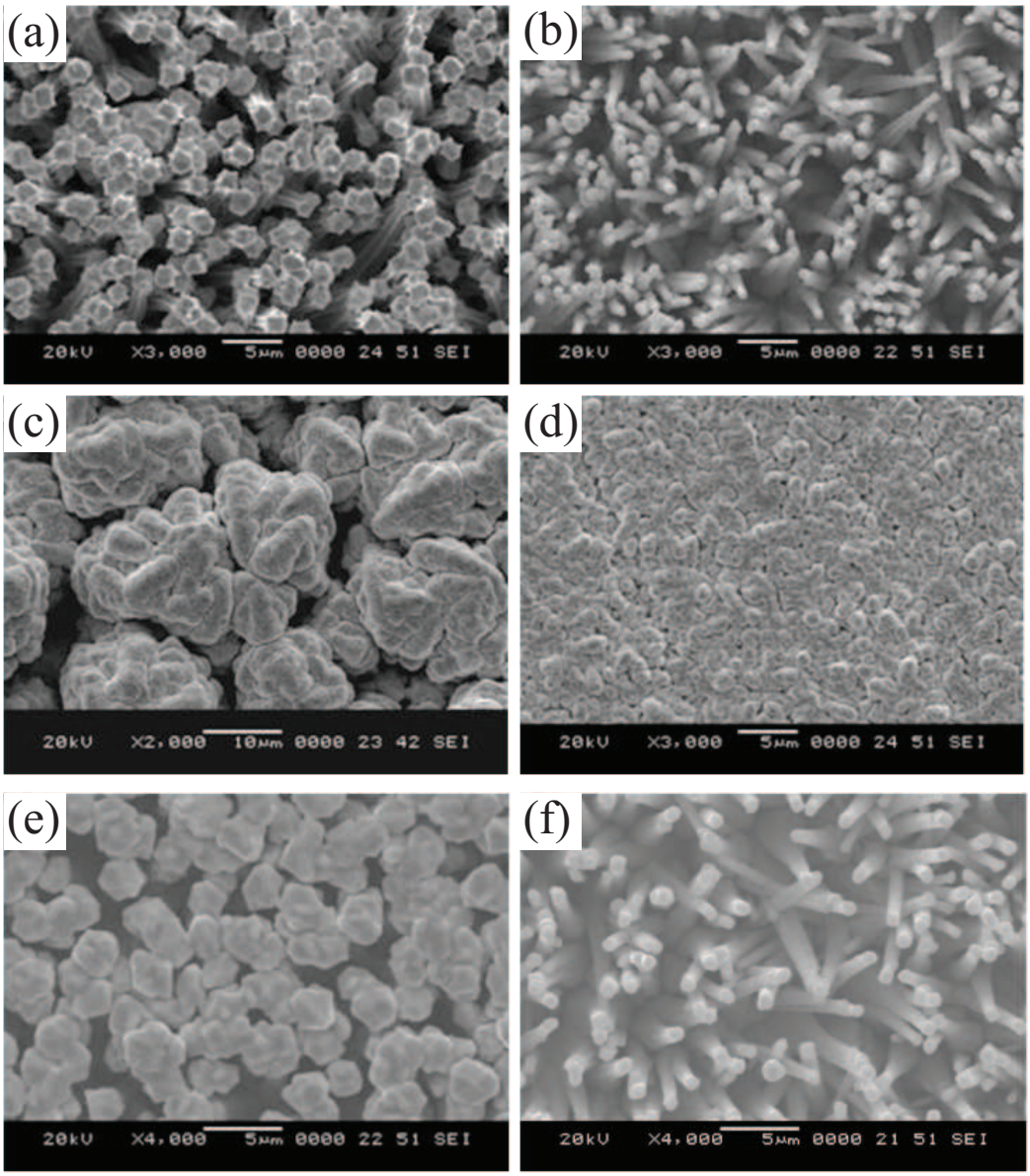

Figure 1.2: SEM micrographs of fabricated micro-architectured coatings: (a) heavy tungsten over rhenium; (b) light tungsten over rhenium; (c) coarse nodular tungsten; (d) fine nodular tungsten; (e) heavy molybdenum over rhenium; and (f) light molybdenum over rhenium [2].

umetrically distributing the incident heat flux more efficiently. Thus, these coatings exhibit improved high thermal heat load capacity and are less prone to failure under extreme temperatures [29–31]. In addition, due to the high melting point of tungsten (3410 °C), these coatings can be used for a wide range of applications with minimal erosion due to ablation or melting. These coatings have been demonstrated to be capable of mitigating extremely high thermal heat (well above 2500 °C) [28]. Another advantage of such micro-architectured coatings is their ability to reduce erosion due to sputtering [28, 32]. This reduced erosion rate is attributable to the non-planar surface topography. Ongoing research to measure the sputter erosion rates of micro-architectured coatings have shown that the quartz crystal microbalance frequency slope, which is directly proportional to a sputtering erosion rate, decreases by 20 to 40% as compared to that of flat surface bulk tungsten [33]. This decrease in the erosion rate can be explained physically by considering the increased likelihood of material recapturing and redepositing due to geometric trapping. This is schematically shown for tungsten micro-patterned coating in Figure 1.3(b). As tungsten surface atoms are knocked out by an incident ion from the surface of the coating, there is a high probability that these atoms will be re-deposited at the surface of a neighboring micro-patterns due to the irregular micro-patterned shapes and large surface to volume ratio.

The use of micro-architectured refractory metal coatings is already on the rise in a number of high temperature applications. High-emittance micro-patterned rhenium

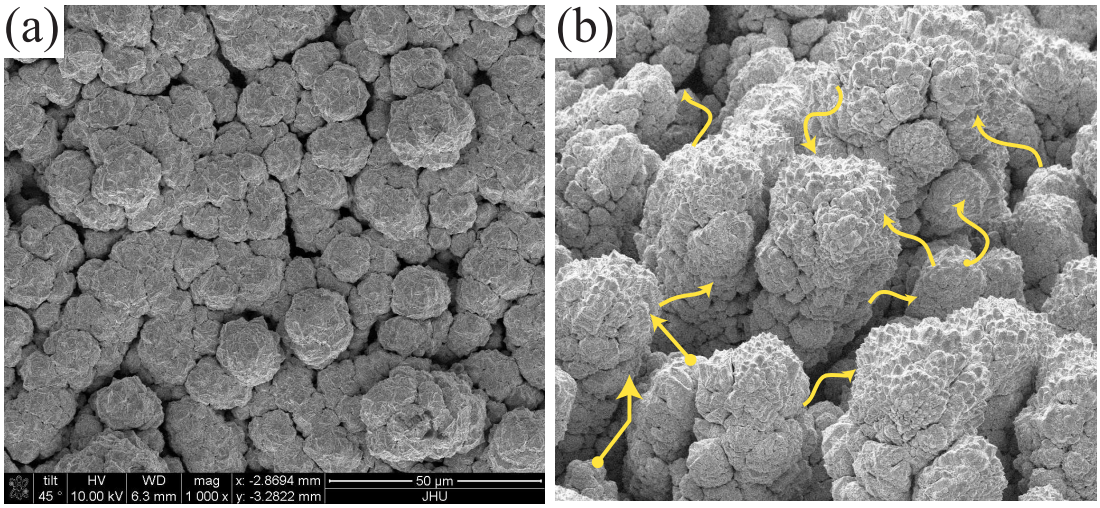

Figure 1.3: SEM micrographs of a W cauliflower-like micro-patterned coating: (a) top view; (b) 3D view showing the W curds grown vertically from the substrate. Yellow dots and arrows show schematically sputtered tungsten atoms being redeposited on their neighbors.

coatings are being applied to tungsten cathodes used in high-wattage (up to 8000 W) mercury short arc lamps (see Figure 1.4(a)) for semiconductor microlithography. The ultra high surface area micro-patterned rhenium coating (see Figure 1.4(b)) acts to significantly increases thermal radiation. The operating temperature of these components is 2700 °C with a lifetime of $\sim$ 100,000 hours.

Thin micro-patterned rhenium coatings are also applied to the outer surface of radiation-cooled, iridium-lined rhenium combustion chambers used for satellite propulsion systems, which operates at a peak temperature of 2200 °C (see Figure 1.4(c)). Rhenium micro-patterned coatings are also used on the outside of chemical rocket engines to help keep the walls cool and minimize thermal soakback [2]. Cooling the walls enablesthe operating temperature of the gases to be increased, which in

turn increases the engine performance. It is also interesting to note that in the 1970's, micro-patterned tungsten coatings having a WO_3 amorphous outer layer were first developed as solar-absorbing and enhanced photothermal energy collection coatings [34, 35].

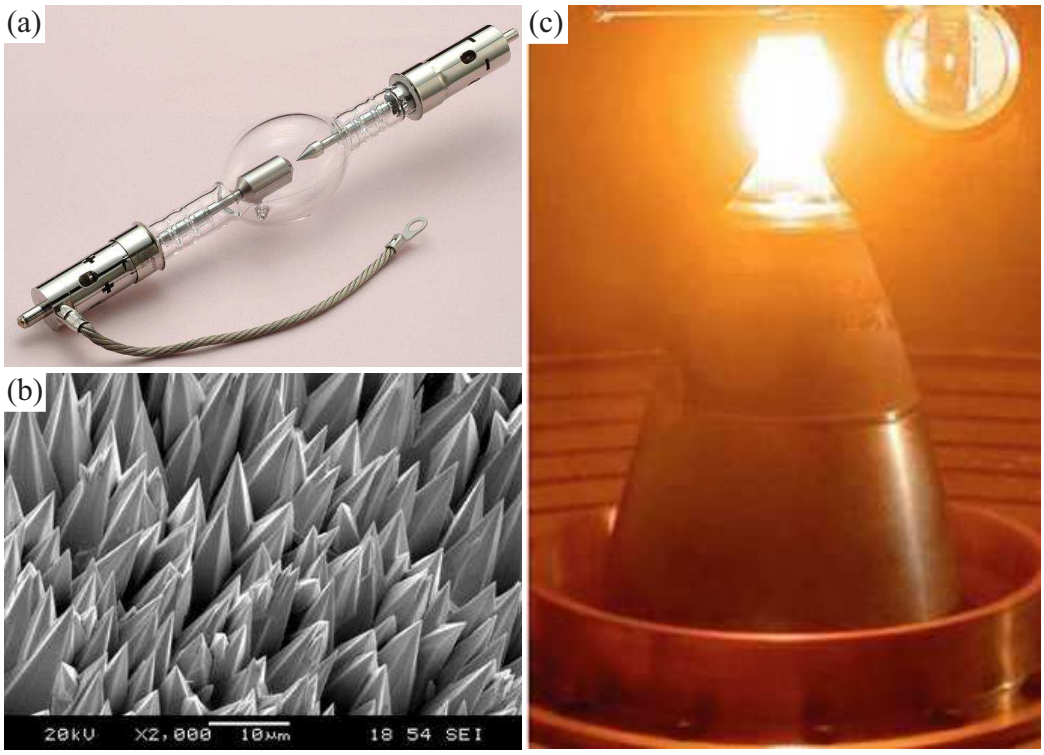

Figure 1.4: (a) Mercury short arc lamp. (b) High-emittance micro-patterned rhenium coating. (c) Chamber during hot-firing of Aerojet liquid apogee engine (peak surface temperature: 2200 °C [2]). Figures are adopted from *http://ultramet.com*

Finally, while ongoing research shows that such micro-patterned surfaces are capable of mitigating high thermal loads with low sputtering rates, ***there is very little known about the microstructure of these coatings, their thermo-mechanical properties, deformation, and failure***. Current thesis work is targeting on de-

veloping a systematic knowledge and fundamental understanding on these aspects through advanced material characterization techniques, *in situ* micro-mechanical experiments, as well as microstructure based computational simulations. Eventually, the proposed integrated experimental-numerical approach will help in accelerating the future development of such coatings.

1.2 Short Background on Microscale Experiments Using Nanoindentaion Based Techniques

Studies on the micro-mechanical response of metals with reduced dimensions can be traced back to 60 years ago. In one of the most earliest studies, Brenner grew metallic whiskers with diameters ranging from a few micrometers to tens of micrometers and length of a few millimeters, and then tested them using an ad-hoc tensile apparatus [36, 37]. It was shown that whiskers with diameter less than a few micrometers exhibited a high resolved shear strength up to 2-6% of the shear modulus, which is close to the theoretical limit. With an increase in size, the average strength was observed to decrease linearly with respect to the inverse of diameter with increased scattering. Although Brenner's study provided a unique insight into size effects in metals, his experimental method is limited to whisker geometries.

Around the same time, Suzuki et al. [38] tested single crystal copper with diameters ranging from 60 micrometers to 1 millimeter, and showed that with a decrease in sample dimension, the range of easy glide increases and work-hardening rate in this regime decreases. In contrast, work-hardening in the rapid hardening regime is less affected by sample size but strongly dependent on crystal orientation. They rationalized the observations by introducing the concept of mean free path of dislocations.

The advent of surface nanoindentation techniques have allowed for easy and fast extraction of micro-mechanical properties of materials [39, 40]. In traditional indentation testing, a maximum load is set for each experiment, and imaging of indentation impression after each test is required for contact area calculation, which limits such method only to large scale samples. Moreover, the displacement and load is not recorded, and only hardness is determined as dividing the load by contact area. In the 1990s, Oliver and Pharr [41] demonstrated a practical and robust methodology along with associated apparatus that is able to extract both the Young's modulus and hardness. In this technique, a self-similar 3-sided pyramid Berkovich tip is used, and this well-defined geometry allows contact area to be determined by indentation depth using the so-called area function. During nanoindentation, the indenter exerts a force with resolution below 0.1 µN on the sample surface, while recording the displacement data with a resolution around 0.1 nm. The modulus can then be back calculated based on the experimentally measured contact stiffness during unloading through linear elastic analysis. Alternatively, continuous stiffness measurement (CSM), which is

achieved by superposing a small harmonic force during the indentation, can also be used to sense the contact stiffness during the loading [42]. CSM enables the quantification of mechanical properties as a function of depth even less than 50 nm below the sample surface.

It should be noted self-similar nanoindentation techniques induce a non-uniform and complex stress state on the material, which leads to inhomogenous geometrically necessary dislocations (GNDs) evolution to accommodate the plastic strain gradient [43]. This leads to difficulties in resolving fundamental dislocation mechanisms, which are commonly investigated in uni-axial stress state tests. Moreover, as the deformed region is embedded in the bulk sample or thin film, surface nanoindentation does not easily allow for the exploration of deformation mechanisms associated with reduced sample dimensions.

To address such issues and to enable the study of plasticity in small volumes, Uchic et al. [44] developed a new experimental methodology by combining focused ion beam (FIB) fabrication with a slightly modified nanoindentaion technique [45]. The FIB was used to fabricate cylindrical or rectangular specimens with diameters ranging from a few hundreds of nanometers to tens of micrometers within the surface of a bulk crystal sample. The test is carried out on a conventional nanoindenter outfitted with a flat punch, so that recorded load-displacement data could be converted to a uniaxial engineering stress-strain curve in a straightforward manner.

Inspired by this seminal work of Uchic et al. [44], a large number of small-scale

mechanical experiments have been subsequently performed to study different aspects of the deformation of micron-sized specimens on many different material systems [46–48]. Kiener et al. [49] extended the idea and presented a method to conduct tensile testing at micro- and nano-scales. The miniatured samples and tensile grippers were fabricated using FIB, and a nanoindention system is used to apply a tensile force. For accurate alignment between specimen and the gripper, the experiments were conducted inside of a secondary electron microscope (SEM). Later, to directly observe dislocation evolution in submicron-sized crystals, *in situ* experiments inside of an transmission electron microscope (TEM) have also been carried out [50–53].

Beyond micro-scale unixial compression/tension experiments, Di Maio and Roberts [54] performed micro-scale fracture toughness measurements on coatings using micro-cantilever beams and nanoindentation. The micro-beams were fabricated using FIB and were made with a sharp pre-notch near the fixed end. A point or load was then applied on the free end of cantilever. The fracture toughness/stress intensity factor is finally calculated by inserting the experimentally measured maximum load into a numerical model and solving the linear elastic problem using either the boundary-element method (BEM) [54] or finite element method (FEM) [55, 56]. This approach was then used to measure the fracture toughness of different coatings [55, 57] and also applied to quantify the fracture behavior of local microstructrual features (e.g., grain boundary properties [58, 59]). More recently, combining cantilever geometry and small harmonic oscillations exerted by a nanoindenter, Lavenstein et al. [60] also

developed a micro-scale high frequency fatigue testing methodology to quantify crack initiation and fatigue damage at the small scale.

Recently developments in micro-mechanical testing have also enabled small-scale studies to be performed at cryogenic [61, 62] and elevated temperatures [63–65], as well as at high strain rate [66–68]. New approaches that incorporate testing in an environmental SEM have also led to the *in situ* investigation of hydrogen embrittlement [69, 70].

1.3 Computational Techniques for Modeling Metallic Materials

The evolution of imperfections inside crystalline solids is a multi-scale problem that involves physical processes that span multiple temporal and spatial scales. Due to computational limitations, it is not practical to utilize a single computational technique for all time and length scales; thus, multiple computational techniques, each addressing a single time/length scale, have been developed as shown in Figure 1.5.

One of the well-established simulation methods at the finest time/length scales in computational material science is density functional theory (DFT), which is based upon Hohenberg-Kohn theorems [71]. The major applications of DFT calculations is to predict materials properties (e.g., modulus, crystal structure, etc.) [72] and

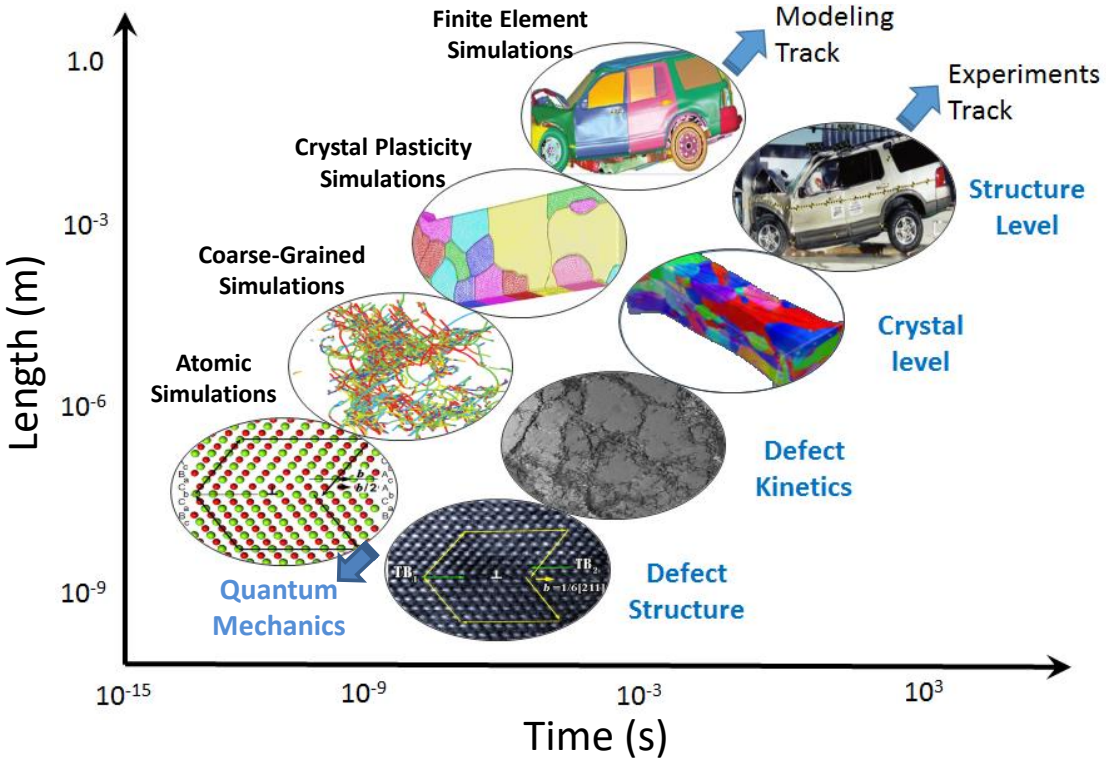

Figure 1.5: Computational and experimental techniques for a variety of length and time scales. This image is courtesy of Prof. Jaafar El-Awady.

to develop interatomic potentials that can then be used for higher length scale for molecular dynamics (MD) simulations [73]. The major limitation for such simulations is not the complexity of physics, but the size of simulation volume, which is limited to a few hundreds of atoms.

MD simulations have been widely used to study deformation mechanisms in materials and typically can model systems up to a few hundred nanometers in size over time intervals of a few microseconds at most. The trade-off is that the electron structure is neglected, and an interatomic potential function is used to describe the interaction between atoms. In MD simulations, atomic arrangement and evolution are explicitly described, which allows for the investigation of a wide range of defects, such as dislocation nucleation [74], twin formation [75] and propagation [76], diffusion [77], grain boundary activities [78, 79].

On the other hand, discrete dislocation dynamics (DDD) simulations originate from the observation that atoms in a perfectly arranged lattice do not contribute to plasticity, and dislocations can be idealized as lines without considering the exact atomic details of their core space [80]. Using this idea, DDD has emerged as a powerful coarse-grained method that allows simulations of volumes up to tens of micrometers which the aligns with length scale probed by micro-mechanical experiments [81**?** , 82]. In their simplest form, DDD simulations rely on stress/force calculations of discretized dislocation segments/nodes and mobility laws extracted from atomistic simulations. At each time step, forces on each dislocation node/segment are first computed using

the linear elastic theory that comprises the elastic interaction of each dislocation in the simulation volume and an externally applied stress field. The total force is then resolved on the dislocation slip system and used to calculate velocity based on the mobility law. During this process, topological evolutions (e.g., junction formation, dislocation annihilation) that enable strain hardening/softening are directly modeled. Unlike other N-body simulations, dislocation density increases dramatically when the material is plastically strained, and the current computational power limits 3D DDD simulations to a few percent of strain. One triumph of DDD simulation has been credited to elaborate the long-debated interplay between sample size and dislocation density in dislocation-mediated plasticity [83]. Recent progress has been focused on improving computational efficiency by using a sub-cycling method [84] and graphic processing unit (GPU) acceleration [85] as well as incorporating dislocation interaction with various of types of defects such as grain and twin boundaries [86, 87].

Crystal plasticity (CP) finite element method (FEM) is another powerful tool that can probe larger volumes and time scales than DDD. In this method, FEM is used to solve a boundary value problem (BVP), which enables the consideration of complex loading/boundary conditions and geometries. On the other hand, crystal plasticity theory provides a mathematical description of material constitutive responses. During the past three decades, a considerable amount of improvement in CP thoery has been made to incorporate more physics and microstructral details. Recent progress includes the development of models that explicitly consider dislocation evo-

lution [88, 89], deformation twinning [90, 91], and interface mechanisms to account the dislocation pile up and transmission at grain/twin boundaries [92]. Beyond these advancements in CP models, the emergence of image-based CPFEM framework is another powerful extension of CPFEM that investigates microstructure-property relationships and guides material designs [93]. In this method, simulation volumes are statistically reconstructed from experimentally measured crystallographic morphological information. These material microstructural information are commonly obtained by combining electron back scatter diffraction (EBSD) and 3D serial sectioning techniques [94]. Finally, it is worthwhile to point out the development of robust mesh algorithm/software and locking-free formulation for linear tetrahedron element (C3D4 or TET4) [95] are also the key progresses of this framework.

1.4 Thesis Objectives and Organization

The objective of this thesis is to provide a systematic and fundamental understanding of the microstructure, thermo-mechanical properties and their correlation with one another for the W micro-architectured coatings. First, the microstructure and surface morphology of these coatings will be discussed. The coating local response is then investigated using micro-mechanical testing techniques as a function of temperatures. These experiments are carried out *in situ* inside an SEM, with a focus on micro-tension, micro-cantilever deflection, and micro-compression studies, which are performed from 293-673 K. In parallel, quasi-3D statistically equivalent virtual

microstructures were generated based on the experimental characterization. Image-based crystal plasticity finite element method (CPFEM) simulations coupled with the cohesive zone model are then performed to rationalize experimental observations and develop better understanding of the microstructure-property relationship.

In Chapter 2, the materials and experimental methods of the investigation are discussed. Microstructural and morphological characterizations of the W micro-architectured coating are first presented. The focused ion beam machining procedures and recipes for micro-compression/tension specimen fabrication are then introduced. Details regarding the micro-mechanical testing apparatus with attention to issues related to high temperature during experiments are then discussed. Finally, techniques and necessary corrections that are applied in post-processing of load-displacement are introduced.

In Chapter 3, the experimental results and discussion of the micro-mechanical response on the W coatings are presented in two steps. First, the effect of sample size and aspect ratio on the mechanical responses and failure mode at room temperature are elucidated. The temperature-dependent deformation is then explored. Finally, a physics-based model to predict the flow stress of tungsten microcrystals is proposed based on the present work and micro-mechanical studies in literature.

To obtain a quantitative understanding of the experimental results and to elucidates deformation mechanisms in the coating, a computational framework that utilizes image-based CPFEM simulations is presented in Chapter 4. Efforts to construct

a statistically equivalent representative 3D polycrystalline microstrucure, develop a constitutive relationship, generate a mesh, and incorporate a cohesive surface/contact are also described. Utilizing this framework, roles of crystallographic texture, grain boundary properties, and microstructure are quantified.

Finally, in Chapter 5, a summary of the present thesis work including key results and findings are listed. To conclude, future work/directions that build on this work are discussed.

Chapter 2

Materials and Experimental Techniques

The unique properties of micro-architectured coatings originate from their sophisticated microstructure. In order to understand their mechanical properties, a prior knowledge on the microstructure is the first and most critical step. This chapter introduces the micro-architectured coatings considered in this study and summarizes the experimental procedure and test apparatus, including, sample preparation, microstructural characterization/analysis, and miniature specimen fabrication using focused ion beam (FIB). Specific details regarding the high temperature *in situ* nanoindentation setup as well as best practices for accurate experimentation will be provided.

2.1 Materials

The as-received micro-architectured W coating were grown at Ultramet Inc. by chemical vapor deposition (CVD) on molybdenum (Mo) circular discs. As shown schematically in Figures 2.1(a), the discs are 10 mm in diameter and 5 mm thick with the W coating being about 50 µm in thickness. Scanning electron microscopy (SEM) micrographs of the disc are shown in Figure 2.1(b). The surface morphology is characterized using SEM and shown in Figure 2.1(c).

A preliminary examination of small features using SEM is shown in Figure 2.2. The surface exhibits a rough cauliflower-like architecture with "curds" having in-plane diameters ranging from 15-30 µm. The top of one of the "curds" was then FIB milled to reveal its internal microstructure as shown in Figure 2.2(c), and the change in slight contrast from the SEM micrograph indicates a polycrytalline microstructure with an in-plane grain diameter of 1-2 µm. In addition, some pre-existing voids/cracks are also observed at grain boundaries.

2.2 Sample Preparation

To prepare the W coating surface for ion channeling contrast analysis and electron backscatter diffraction (EBSD) orientation mapping analysis, a small area with dimensions 100 $\times$ 200 µm^2 on the top surface of the coating was milled using FIB

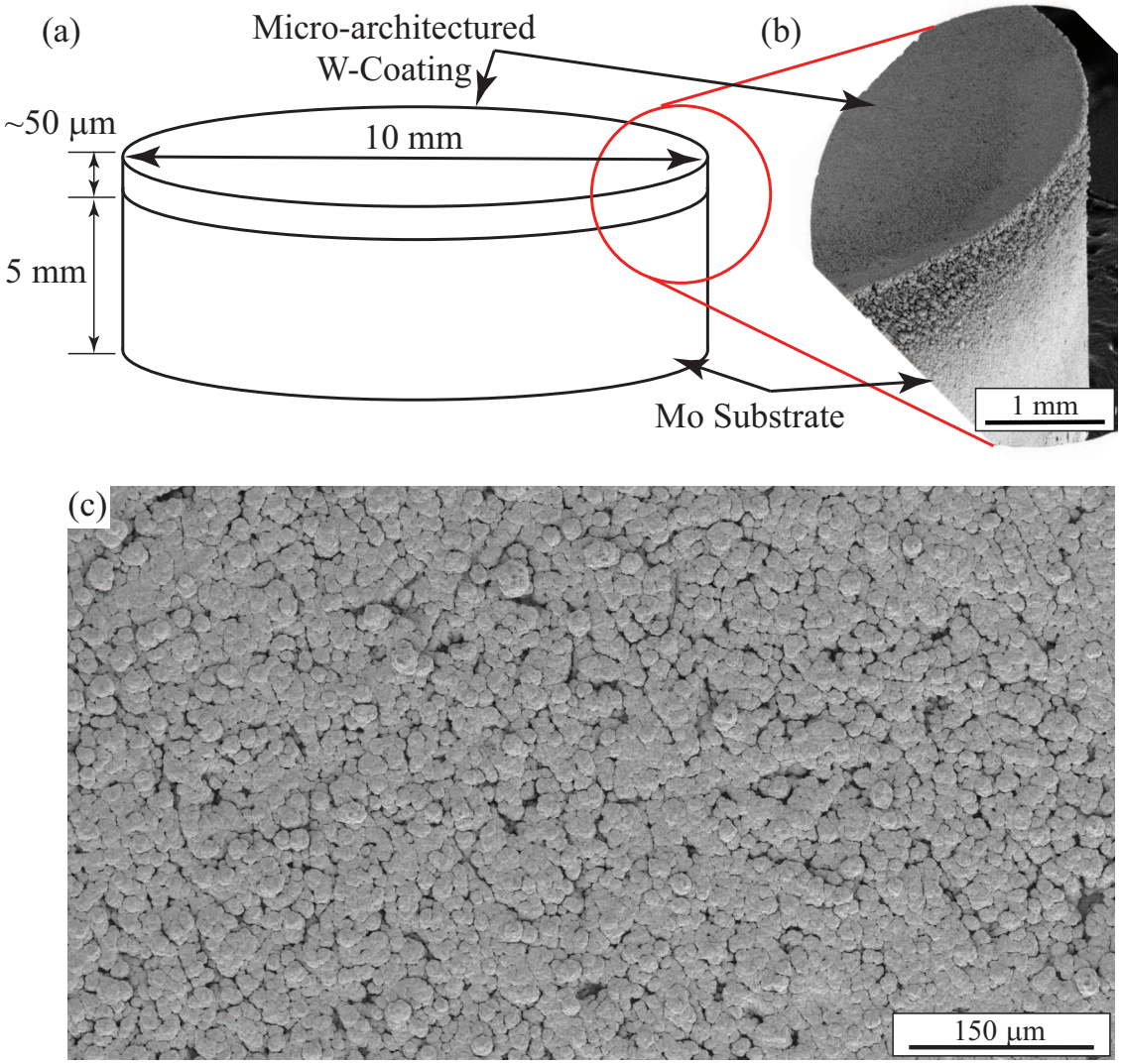

Figure 2.1: Characterization of the as-received W micro-architectured coating: (a) schematic showing the dimensions of the as-received Mo disc coated with micro-architectured W; (b) SEM micrograph that shows the top and side surface of the disc; (c) SEM micrographs of the coating to show the surface morphology.

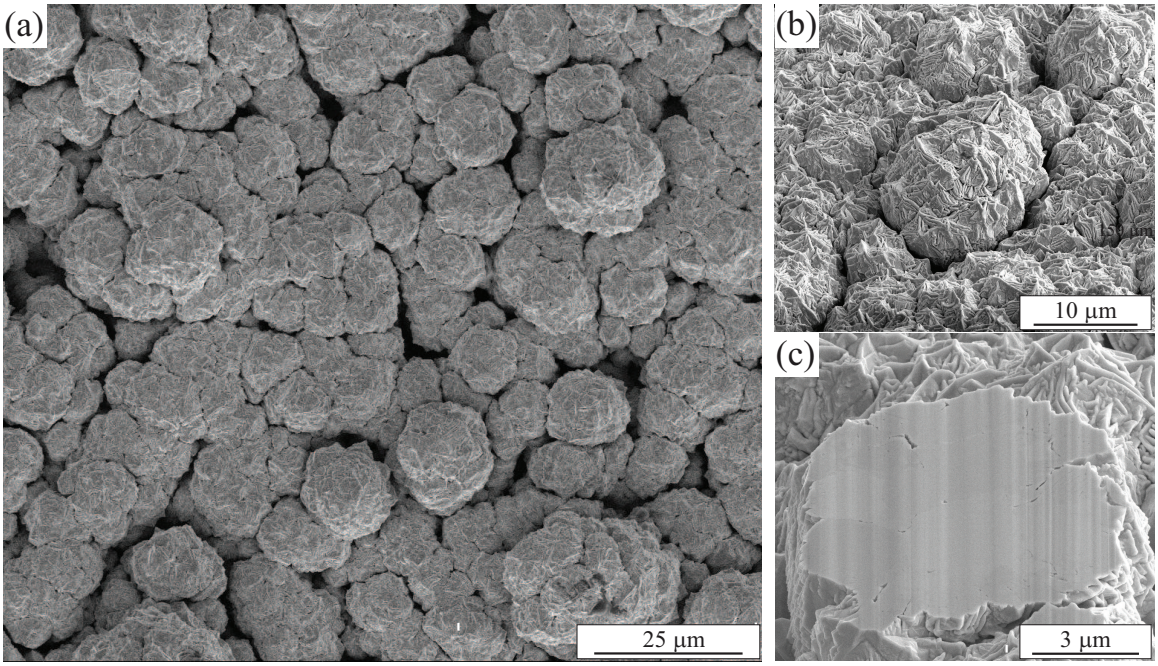

Figure 2.2: SEM micrograph of pristine and sectioned cauliflower-like architectures. (a)-(b) Micrograph of coating surface at different magnifications. (c) Details of FIB'ed top surface, exhibiting polycrystalline microstructure with porous distributed along grain boundaries.

to create a flat region parallel to the surface of the W coating. A through thickness FIB rectangular cut was also made in the middle of the sample to reveal a flat region through the cross-section of the coating with dimensions of 10×20 µm^2.

For microstructural characterization through the entire cross-section of the coating, a second sample was sectioned using a metallurgical low speed diamond saw then mounted in an epoxy risen. After the epoxy was fully cured, the sample was grinded using 800 and 1200 grit metallurgical abrasive discs followed by a 20 minute final polishing using cloth impregnated with a 0.05 µm colloidal silica suspension. A final ion milling step was performed before EBSD analysis using Fischione Model 1060 SEM Mill at an accelerating voltage of 5 kV for 30 minutes.

2.3 Microstructural Characterization

Ion channeling contrast micrographs of the W coating top surface and cross-section using an accelerating voltage of 30 kV and a beam current of 93 pA are shown in Figure 2.3. For the top surface (see Figure 2.3(a)), micron-sized grains are observed along with many pre-existing voids/cracks that are distributed along the grain boundaries. The cross-sectional view reveals that the individual grains in each curd are elongated and the pre-existing voids extend through the coating thickness along the grain boundaries as shown in Figure 2.3(b). It should be noted that the vertical "scratches" are attributed to the so-called FIB curtaining effect due to irregular non-flat surface.

Grain and orientation characterization was performed using a Tescan Mira3 field-

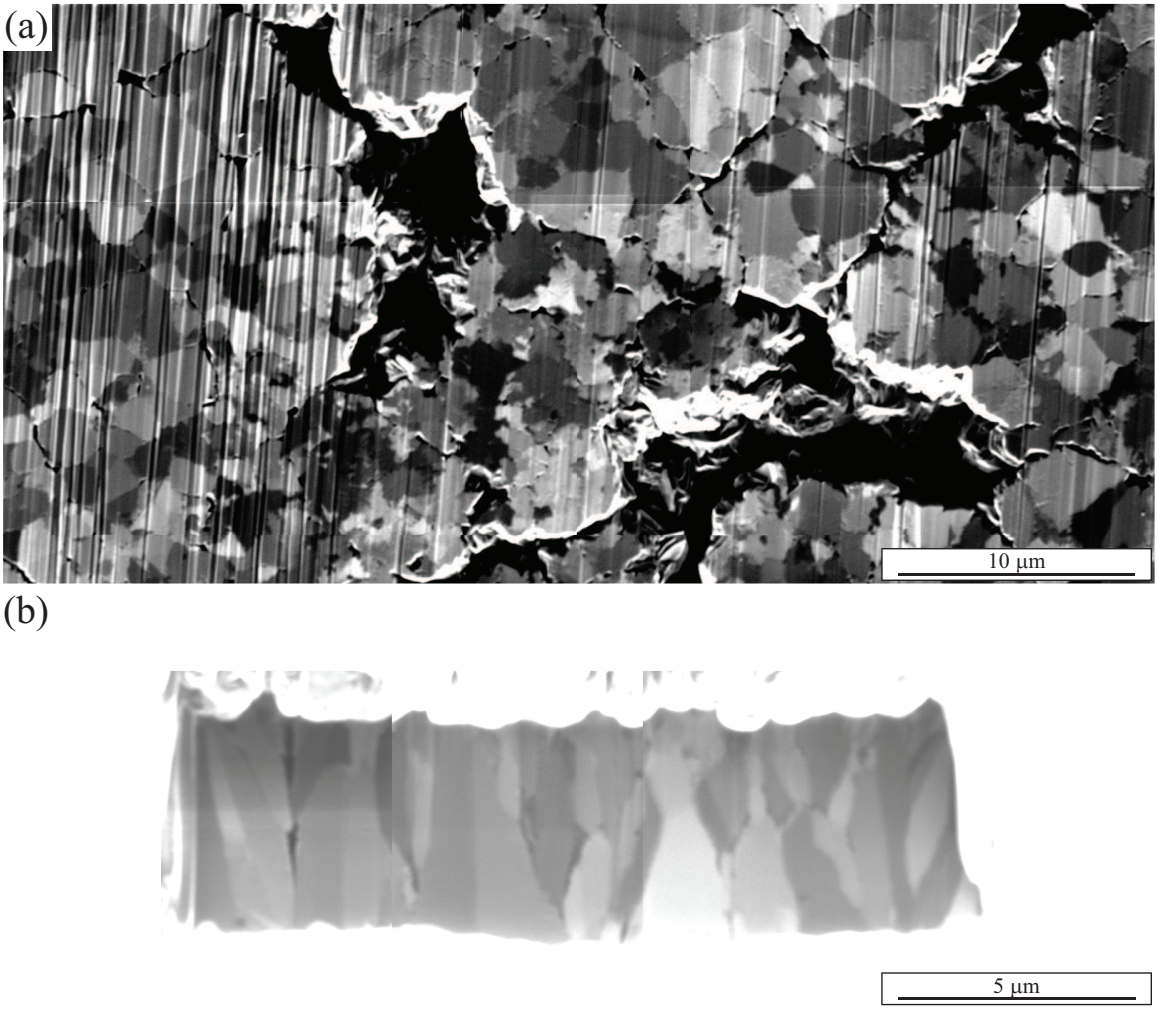

Figure 2.3: FIB channeling contrast micrographs that are taken from the top and cross-sectional surfaces of the coatings that reveal columnar-grain microstructure with pre-existing voids locate at grain boundaries.

emssion gun SEM (FEG-FEM) equipped with an EDAX Hikari EBSD detector. The sample was tilted 70°with respect to the electron beam, and a working distance of 20 mm was chosen for an optimal electron backscattered pattern (EBSP) quality. A step size of 0.1 µm was chosen in order to have at least 100 pixels within each grain and the pattern was collected at a rate of 75 frames per second and indexed using TEAM^{TM} software. These parameters ensure enough exposure time for good EBSP quality while still being able to complete a scan in a reasonable amount of time.

An EBSD inverse pole figure (IPF) orientation map along with the SEM micrographs of the same region before and after FIB polishing from the surface are shown in Figure 2.4. The EBSD map reveals a multiple grains in each curd with a random crystallographic texture. Also, many pre-existing cracks along the grain boundaries are evident from the SEM microgrph (see Figure 2.4(b) . The black non-indexed region is associated with the valley between individual curds.

An SEM micrograph of the cross-section of the W coating is shown in Figure 2.5. It is observed that the coatings consist of two micro-architectured layers on the top of a dense continuous W layer. This dense continuous W layer serves as a bonding layer between the micro-architectured layer and the substrate. The top and second micro-archetectured layers have thicknesses of 12 µm and 18 µm, respectively, while bonding layer is 25 µm in thickness.

The EBSD map of the dashed area in Figure 2.5(a) is shown in Figure 2.5(b), and it indicates that the two micro-architectured layers are predominantly composed

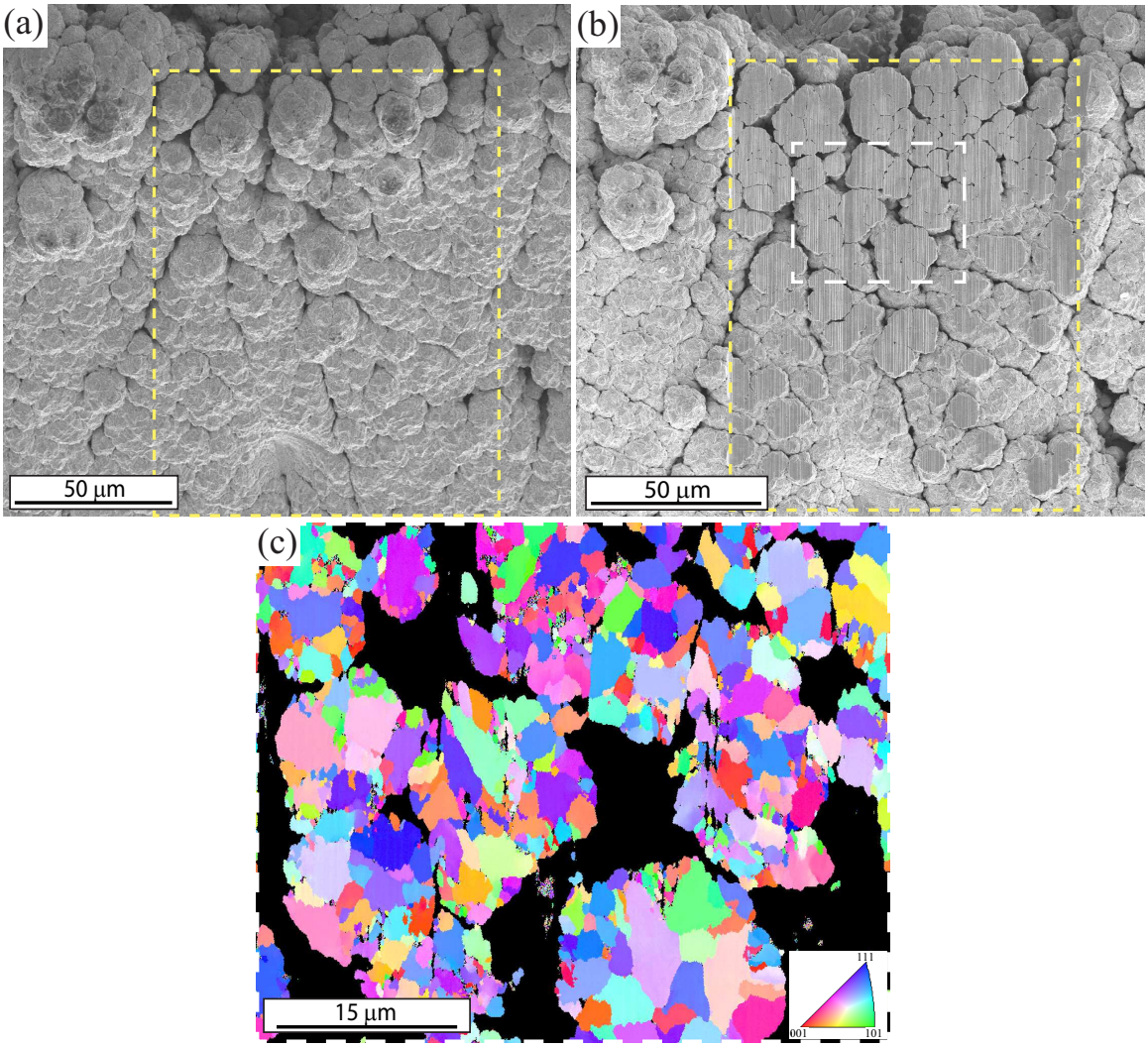

Figure 2.4: An SEM micrograph of the top surface of the as-received micro-architectured W-coating is shown in (a). The area bounded by the dashed yellow box was then FIB'ed to create a flattened surface for EBSD. The EBSD map of the $50 \times 60\,\mu m^2$ area indicated by a while dashed box in (b) is shown in (c). The black regions indicate non-indexed regions between neighboring curds or at cracks/voids along the grain boundaries.

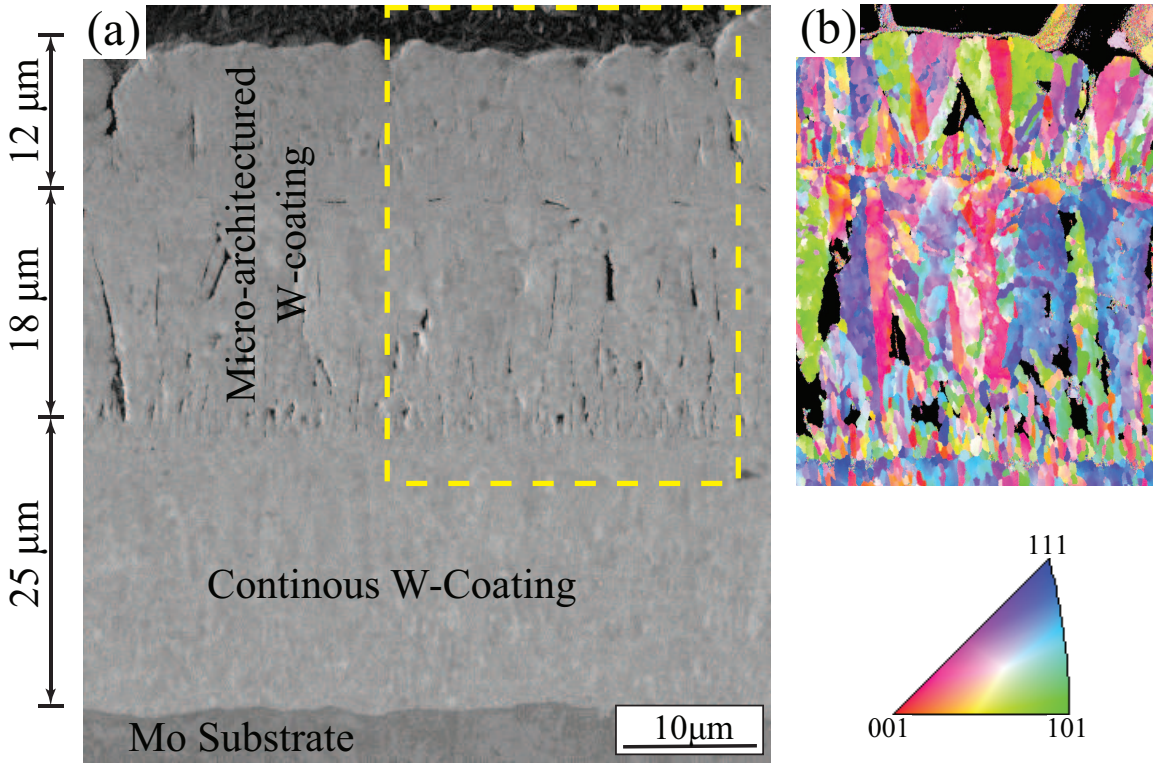

Figure 2.5: (a) SEM micrograph of a cross-section through the W-coating, showing two layers of micro-architectured coatings on top of a continuous W-layer. (b) EBSD map of the area shown by the yellow dashed box in (a). The black regions indicate non-indexed regions at cracks/voids along the grain boundaries.

of nontextured elongated grains that vary in height from $\sim$ 1 µm to the height of the entire layer. Furthermore, many visible pre-existing cracks and voids are also clearly observed along the grain boundaries in both the micro-architectured layers as compared to the dense CVD-grown coatings [96]. These voids can potentially mitigate in-plane thermal stresses and strain incompatibilities by reducing the coating confinement and allowing it to expand and contract more freely during cyclic thermal loading. The deposition of two micro-architectured layers instead of a thick single layer can potentially help achieve the desired grain size, since the grain size continuously increases along the growth direction. This is evidenced by the larger grain sizes near the top of each layer versus the smaller grain sizes near the base of each layer.

Finally, the grain size analysis is performed on a 50 $\times$ 60 µm^2 area containing $\sim$1300 grains. The raw EBSD orientation data is first "cleaned up" through grain dilation with a tolerance angle of 2° and minimum grain size of 10 pixels using OIM Analysis 7 software. The grain size information is then exported, and the histogram is generated using a bin size of 0.28 µm shown in Figure 2.6. The mean grain diameter is 1.26 µm and the standard deviation is 0.86 µm.

2.4 Micro-specimen Fabrication

Inspired by the first micro-compression experiment by Uchic et al. [44], tremendous amount of attention has been directed towards conducting micro-mechanical testing with this cylindrical geometry to extract the thermo-mechanical properties of

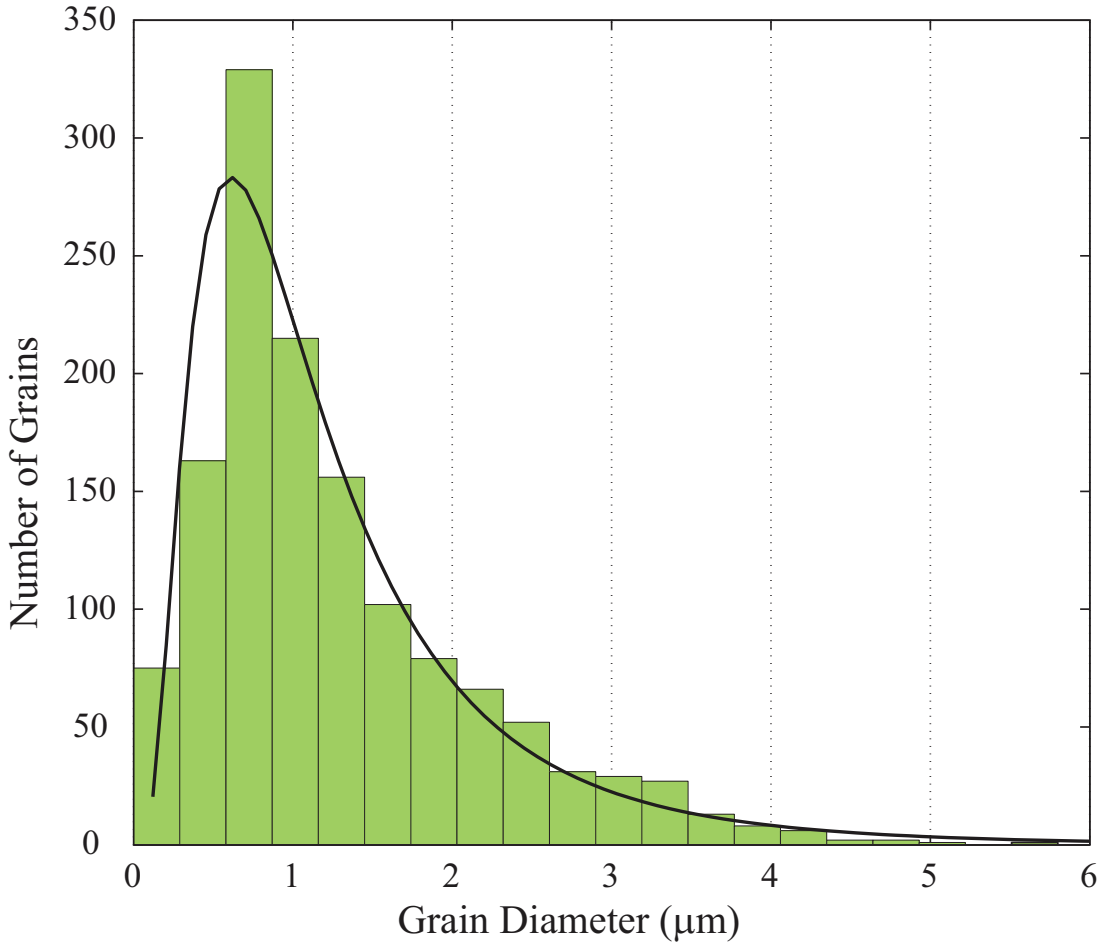

Figure 2.6: Grain size distribution for micro-architectured tungsten coating based on EBSD IPF map from top surface. The region has a area of $50 \times 60\,\mu m^2$ and contains $\sim$ 1300 grains for statistical significance. A lognormal fit to the data is also shown.

materials. In such experiments, preparing high quality specimens is of the utmost importance for obtaining reliable results. Among all the methods, FIB micro-machining is the most widely accepted and used technique due to its high precision (on the order of tens nanometers) and ability of fabricating samples with different geometries having size up to tens of micrometers. Here, the fabrication process of micropillars, micro-tensile specimens (dog bone shaped), and cantilever beams, are introduced.

2.4.1 Micropillar Fabrication

There are two commonly adopted FIB micro-machining techniques for micropillar fabrication, namely, lathe and annular milling. In lathe milling, a large circular trench is firstly created using a high ion beam current, which leaves a tapered column at the center that has dimensions close to the final dimensions of the desired micropillar. The sample surface is then tilted such that the FIB is now directed at the sidewall of the column at an oblique angle. A rectangular pattern is then milled at the side of the column. This process is repeated by rotating the micropillar along the column axis a few degrees at a time until the final cylindrical geometry is achieved. This results in a well-defined, taper-free pillar geometry. This method is typically automated using a fiducial mark and image recognition capabilities built into the FIB software [45]. For annular milling, the ion beam is directed such that it is normal to the sample surface and several successive concentric circular ring pattern with decrease outer and inner diameter are utilized to gradually remove the material. The current is gradually

reduced as the inner milling diameter starts to reach the desired pillar diameter in order to reduce ion implantation and to better control the final taper angle.

The major advantage of lathe milling is the ability to fabricate micropillars without taper along the height of the pillar. However, depending on the material, it should be noted that this method lead to excessive ion exposure that may significantly affect the mechanical properties of the material. This is particularly important for materials that are susceptible to ion implantation, such as Fe and Mg. Hütsch and Lilleodden [97] showed the 5 % flow strength of [1 1 0] oriented 5 µm Mg micropillars increased from 70 to 270 MPa by switching from annular milling to lathe milling . Additionally, regarding deformation morphology, they also reported annular-milled micropillars show deformation by a single slip band without any surface cracking, however, lathe-milled micropillar show a couple of fine slip bands with surface cracking. However, for materials with larger atomic number (e.g., Ni), the two different methods yield similar results [45, 98]. Kiener et al. [99] showed that, for Cu, the Ga concentration reduces to less than 2 % at a depth beyond 50 nm from free surface. Furthermore, a recent study using atom probe tomography indicates the effect of Ga implantation is limited for Ni [100]. Thus, ion implantation is only of relevance for materials with low atomic numbers, and it can be alleviated by carefully choosing ion beam currents and optimizing the automation process.

Annular milling is more widely used in the community due to its quicker fabrication time and ease of implementation. However, the disadvantages include: (1) slight

taper angles ranging from 1° to 2° are commonly observed; (2) non-uniform base geometry, which complicates the height measurement; and (3) the rounded edge. These issues becomes more severe when the micropillar size is in the submicron region.To alleviated such issues, square cross-section micropillars have also been introduced [101, 102], which have two advantages: (1) the taper angle can be eliminated achieved by tilting the stage by 1∼2°; and (2) slip trace angle measurements are straightforward due to the planar side walls.

In the current work, all micropillars were annularly milled on a FEI DB235 FIB-SEM dual beam workstation. The whole process involves three steps that are briefly discussed here taking the fabrication of a D = 5 µm micropillar as an example. At the first step, a large trench is created with an exterior diameter of 50 µm and interior diameter of 12.5 µm using the highest available ion current (20 nA). In the second step, similar to previous step, two ring patterns with gradually decreasing diameters are milled using currents of 5, and 3 nA respectively. This results in a column with diameter $\sim$ 5.5 µm and the desired hight. Finally, a small current of 0.5 nA is used for final polishing to minimize the taper angle and reach the final diameter. This recipe gives very good pillar geometry. It should be mentioned that creating a trench with an exterior diameter of 50 µm in the first step is time consuming, but it's necessary in our case for following reasons: (1) avoid potential contact between punch and trench sidewalls; (2) provides a clear viewing of the deformation process during *in situ* experiments; (3) facilitates searching and aligning the micro-specimen with the

flat punch in optical *ex situ* nanoindentation system where magnification is limited; and (4) reduces redeposition of sputtered atoms on the micropillar surface.

It should be noted that the annular milling can lead to varying milling rates due to the polycrystalline and porous microstructure of the W coating as shown in Figure 2.7. To address the issue, hard amorphous Pt "caps", having diameters equal to the desired "pillar-like" microcrystal diameters, were first deposited onto the polished coating surface before the FIB milling process. These Pt caps help in fabricating microcrystals with smooth tops and side surfaces by avoiding varying milling rates due to the polycrystalline porous microstructure of the W coatings as shown in the insert of Figure 2.8. The Pt cap thickness is less than 50 nm and is not expected to affect the mechanical response of the micropillars.

2.4.2 Micro-tensile Specimen Fabrication

Dog bone shaped micro-tensile specimen and a dedicated gripper were also fabricated for testing the interface strength of multi-layered W coatings. The specimens were fabricated at the edge of the parent sample and followed a three-step FIB process. In the first step, rough cuboidal geometries were milled at the edge of the sample using a Clark-MXR Ti-Sapphire femtosecond laser. During this process, the laser beam is perpendicular to the sample top surface, and the final shape is shown in Figure 2.9(b). In the second step, the sample is rotated 90° such that the cross-section is facing the FIB beam. This positioning allows mlling of the dog bone shape

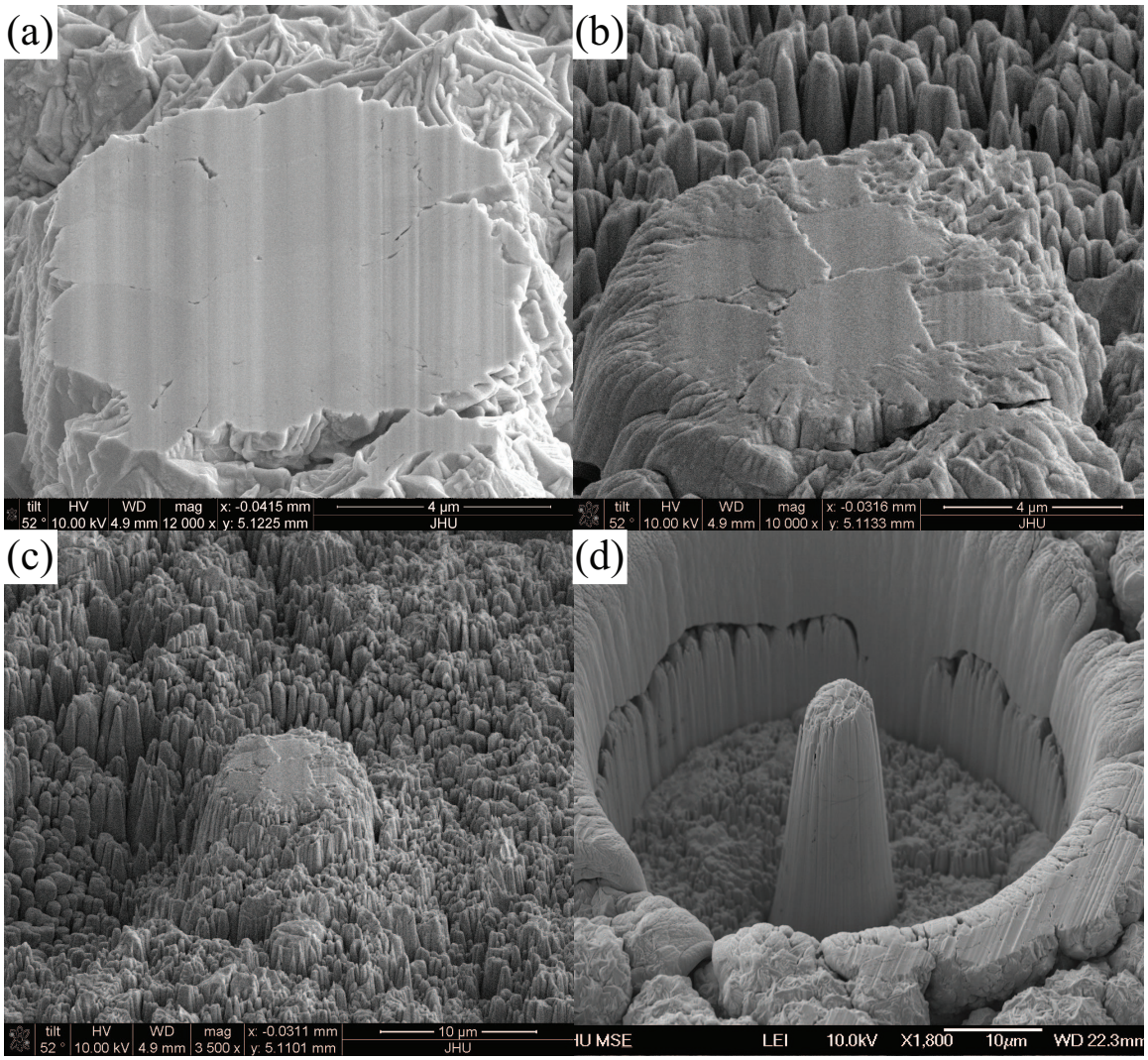

Figure 2.7: (a) A single W "curd" after it was FIB milled parallel to the sample surface, showing a seemingly flat surface. (b) The same W "curd" after being exposed to annular milling (i.e., milling perpendicular to the flat surface) for a short time. The different milling rates of the different grains is clearly observed. (c) SEM snapshot of milling process (d) An unfinished 5 µm micropillar fabricated from the center of a W "curd" without pre-depositing Pt coating to even out the surface.

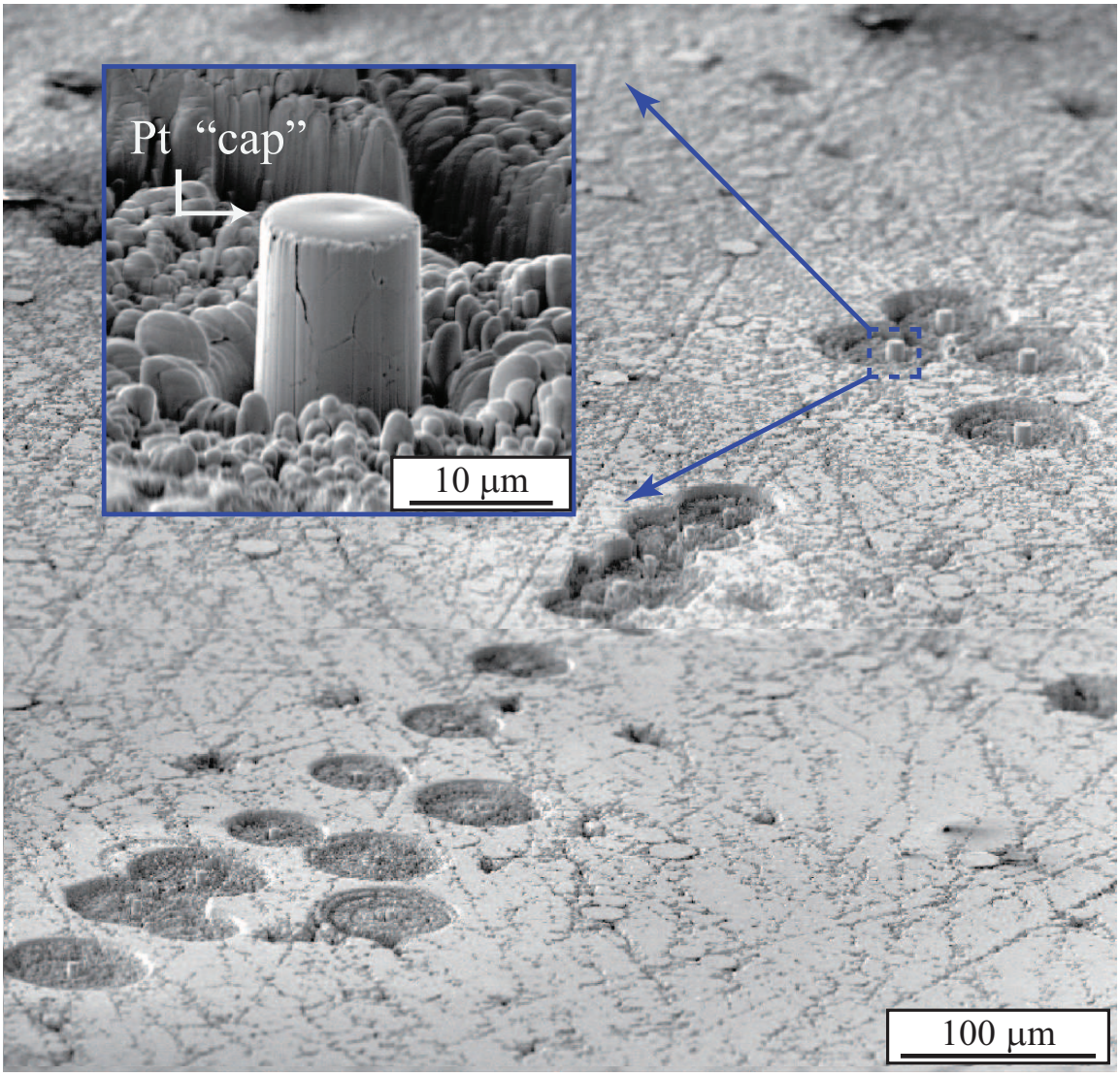

Figure 2.8: SEM micrograph of the top surface of a mechanically polished micro-archetectured W-coating. Several FIB'ed micropillars were fabricated into the coating. The insert shows a zoom in of a D=8.6 µm pillar with a Pt "cap".

specimen with pre-defined polygon patterns in the FIB software. In the last step, the sample is thinned down to the desired thickness from the top. Extra steps may be required to remove the re-deposited material to achieve a better geometry. The final geometry is shown in Figure2.9(c).

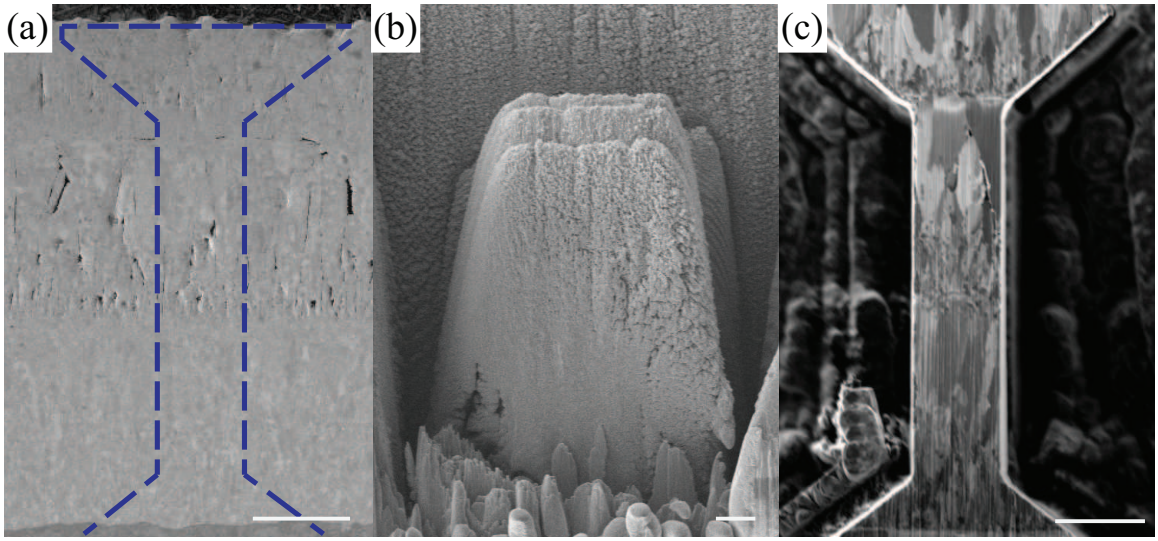

Figure 2.9: Micro-specimen fabrication. (a) Cross section view of micro-architectured tungsten coating along with the dog-bone FIB milling pattern. (b) Cuboidal geometry created with femto-second laser for next step FIB micromachining. The debris on surface comes from the re-deposited materials, which is then cleaned by using ultrasonic cleaner bath. (c) A finished tensile specimen having dimensions $10.3 \times 5.8 \times 42\,\mu m^3$ imaged in FIB channeling contrast mode to reveal the microstructure. The scale bars are 10 µm for (a)(b)and(c).

The gripper is also micro-machined using FIB. The grip is fabricated from an W needle used on nanomanipulators (i.e., Omniprobe) used in FIB and SEM. The tip is first removed to have a flat end with a diameter of 50 µm which gives enough space

to fit the pre-designed shape. Another 2-3 mm length was then cut from the flat-ended needle and was used for gripper fabrication using FIB. At the end, W gripper is bonded to the SiC fiber tip using conductive epoxy. The SiC fiber has a diameter of 50 µm with a tungsten core to enhance the electrical conductivity. It is cut from a long fiber and brazed onto an indenter holder made by Micro Star Tech. The combination of tungsten gripper and SiC offers low lateral stiffness and good griping on specimen. It should be note that low lateral stiffness is very critical to maintain the uni-axial stress state and minimize the possibility of distorting the sample [103].

2.4.3 Micro-cantilever Beam Fabrication

Cantilever microbeams having a cross-sectional areas of $\sim$ 70 µm (width) $\times$ $\sim$ 45 µm (depth) and aspect ratio of 5$\sim$6 were fabricated using femtosecond laser at the straight edge of the parent crystal as shown in Figure 2.10(a)). In the first step, a femtosecond laser raster cut on the top surface gives the shape of the beams. In the second step, parent sample was flipped 90° to allow a second laser cut to remove the material at the bottom. Finally, the samples was submerged into acetone solution and was cleaned using ultrasonic cleaner for 30 seconds to remove redeposited debris. The final shape is shown in Figure 2.10(b) and (c).

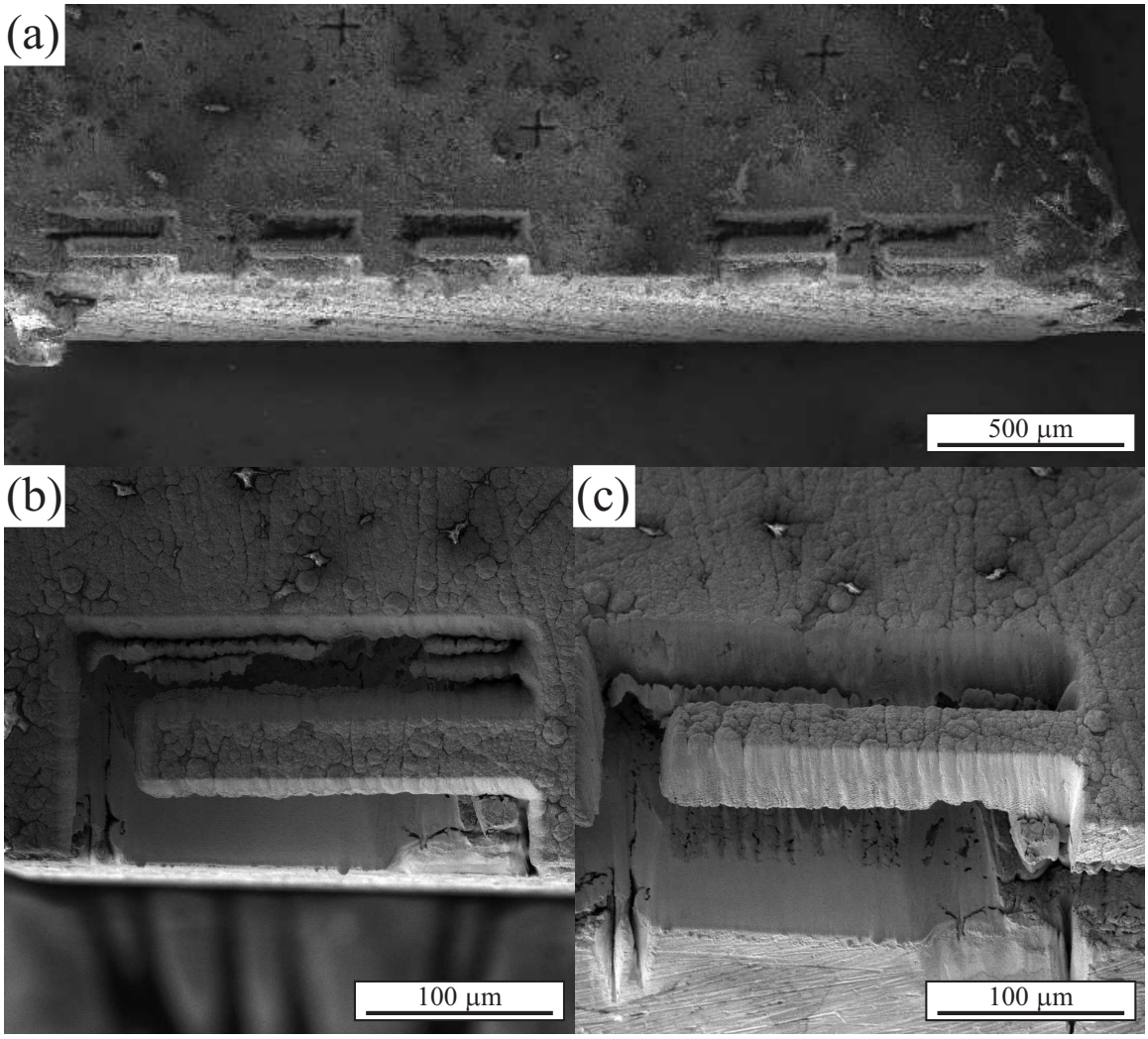

Figure 2.10: Micro-cantilevers fabricated using femtosecond laser. (a) Five beams were fabricated at the edge for the parent sample. The "+" shaped markers are laser cuts used for laser and stage calibration. (b) Top and (c) 45° views of a laser-fabricated micro-cantilever.

2.5 Micro-mechanical Testing at Elevated Temperatures

2.5.1 Overview of the InSEM HT System

All *in situ* experiments were performed using the InSEM HT nanomechanical testing system at Johns Hopkins University, which is installed on the Tescan Mira 3 FEG-SEM, as shown in Figure 2.11(b). This *in situ* setup allows for: (1) accurate positioning indenter tip; (2) real time visualization; and (3) high vacuum chamber minimizes the possibility of sample or tip oxidization and thermal convection.

The InSEM HT system comprises four major components : (1) the *in situ* tester, (2) the temperature and positioning controllers, (3) the water cooling system, and (4) a computer running InView software.

The tester module includes a high-precision InFroce 50 nanomechanical actuator and sample mounting stage which are mounted on cradle before testing. The InForce 50 actuator utilizes a voice-coil design and comprises a built-in capacitive gauge for displacement measurements. The actuation force is generated based on the principle of Lorentz force equation, and the attendant displacement is measured by a capacitive gauge. The actuator is inherently load-controlled but pseudo-displacement control can be achieved through a software level proportional–integral–derivative (PID) con-

troller. The actuator has a maximum load of 50 mN with a resolution of 3 nN, and a displacement range of 50 µm with a low electronic noise less than 0.1 nm.

This high temperature indenter head module is designed based on the InForce 50 actuator and is equipped with independent active heating and water cooling circuits as well as multi-location thermocouple feedback, as shown in Figure 2.12. The thermocouple is bonded to a ring-shaped metal, which is attached to the end part of tip. This proximity allows accurate measurement of the tip temperature. To limit the thermal flow to the tip region, the indenter column is coated with a low thermal conductivity and thermal expansion ceramic. A metal foil is also added before the spring and connector to provide effective shielding to radiation. A thermoelectric peltier is glued to the bottom of this module, which water-cools the block during experiments. This design is able to extract surplus heat in order to protect sensitive electronics and maintain steady thermal flow. To monitor the temperature near the heat sink, a second thermocouple is added that is sandwiched between the cooling block and the peltier. This isothermal heating design allows a tip temperature 600 °C to be reached, while the actuator stays below 60 °C.

The module for sample mounting adopts a similar design as the head module and is shown in Figure 2.13. The ring-shaped clamp is designed to ensure full contact between the sample and heater to reduce the temperature gradient and base compliance. The sample thermocouple will be inserted into the groove pre-fabricated on the heater surface. The major disadvantage of this design is temperature measured by

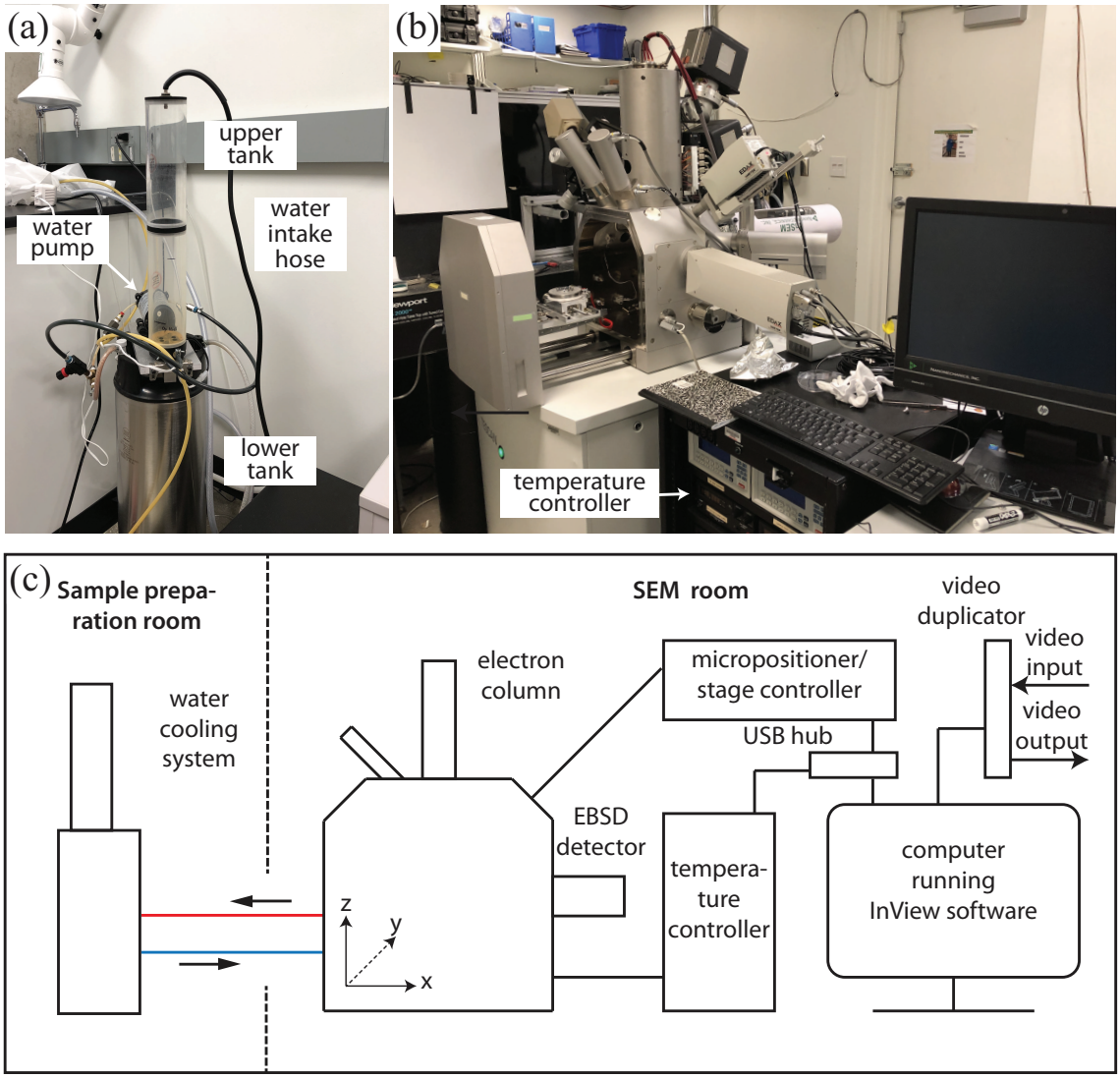

Figure 2.11: Images and schematic of the InSEM HT installed on a Tescan Mira 3 SEM used for this thesis work. (a) Water cooling system in the sample preparation room next to the SEM room; (b) picture of InSEM HT system; (c) schematic of InSEM HT system.

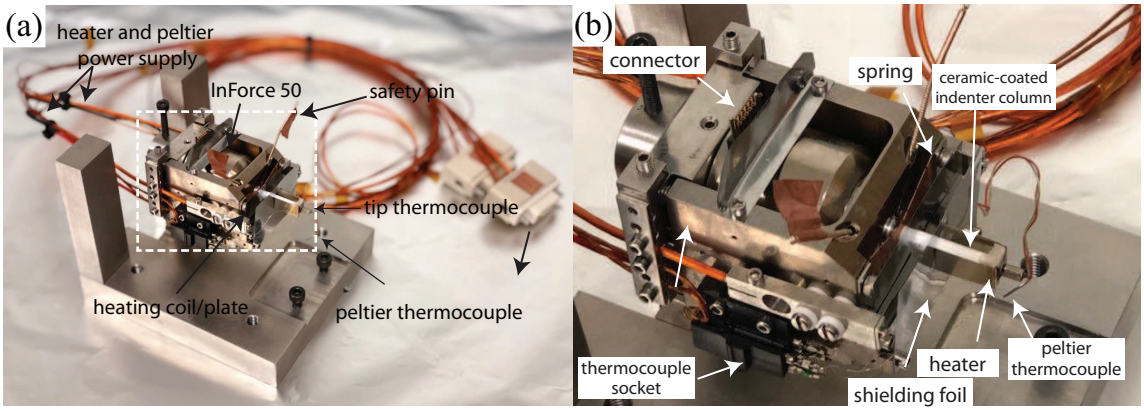

Figure 2.12: Images of InSEM HT head module. (a) indenter head module (b) zoom in of dashed lined region for better illustration of key components. Safety pins serve as limiter of indenter column to avoid potential damage during installation or transportation and are removed before experiments.

the thermocouple may not necessarily represent sample top surface temperature due to thermal gradient. This difference could be governed by a few factors, including, testing temperature, sample thermal conductivity, and sample bottom surface finish etc.. Thus, a method to minimize this difference is neccesary and will be discusses later.

The temperature control modules includes two Lake Shore® Model 335 cryogenic temperature controllers for the tip side and sample side, respectively. Both controllers support two sensor inputs and two closed loop PID outputs for external power supplies. The temperature readings from sensors are sent to the InView software for real time monitoring and recording through the USB port.

A water cooling system is located in the sample preparation room and connects to

the tester from the back of the SEM through a water hose. This reduces the physical vibration generated by the water pump and avoid potential damage to the SEM due to water leaking. The water cooling system contains two water tanks that require $\sim$ 3 gallons of distilled water for normal operation.

A desktop PC running InView software is utilized to control the indenter stage and record the testing data. To store the video from SEM observations during the experiments, a video duplicator is added that splits the ouput from the SEM computer to both the InSEM computer and the SEM monitor.

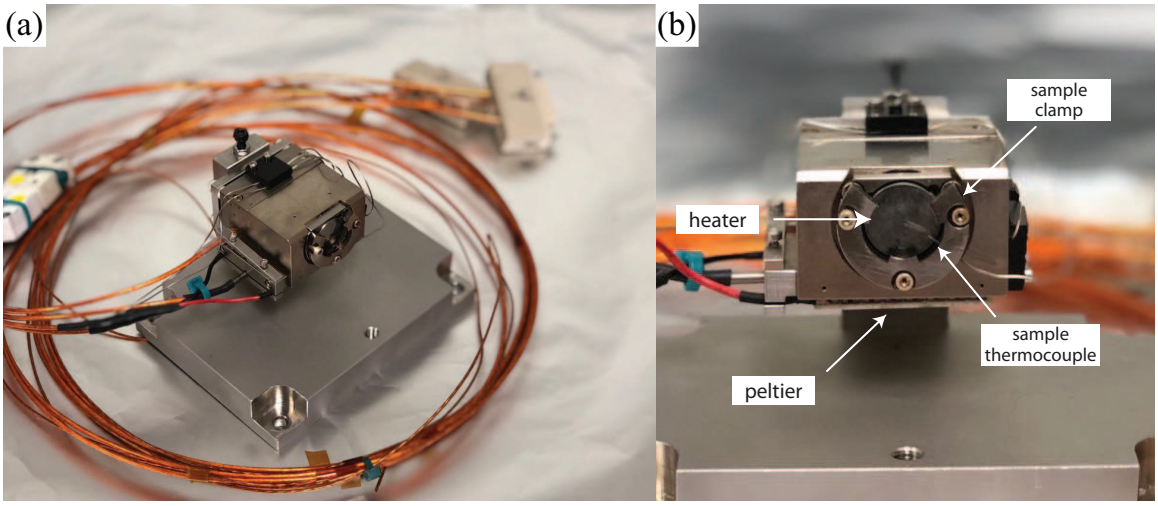

Figure 2.13: Images of the InSEM HT sample module. (a) A 3D view indenter sample module. (b) Side view of the module with a description of key components.

2.5.2 Sample and actuator mounting configuration for InSEM HT system

A cradle mounting setup is used for our experiment as shown in Figure 2.14. In the remaining of this chapter, uppercase X, Y, Z indicate the SEM three-orthogonal coordinate system, as shown in Figure 2.11, lower case x, y, z indicate cradle three-orthogonal coordinate system, as shown in Figure 2.14. The cradle is designed to directly mount the SEM stage in order to take the full advantage of the X and Y direction translation and Y-axis tilting capabilities of the SEM. This setup allows 15° of tilt along the Y-axis at a working distance less than 25 mm, which ensures good image quality. Additionally, the stage-mounted cradle has two high precision piezoelectric based micropositioners, which enables accurate alignment of the tip with the micro-specimens. The indenter head module is mounted on the arm with z-axis movement capability (see Figure 2.14), and the sample side module is mounted on a plate, which can freely move in the x-y plane. The z-axis motor has a maximum displacement range of 1 cm which can adapt to samples with different thickness. The xy-axis micropositioner has a maximum range of ± 1 cm, which covers all of the positions within the sample mount area and allows accurate positioning of the micro-specimen bellow the indenter tip. The micropositioners are controlled through the InView software using a controlling box.

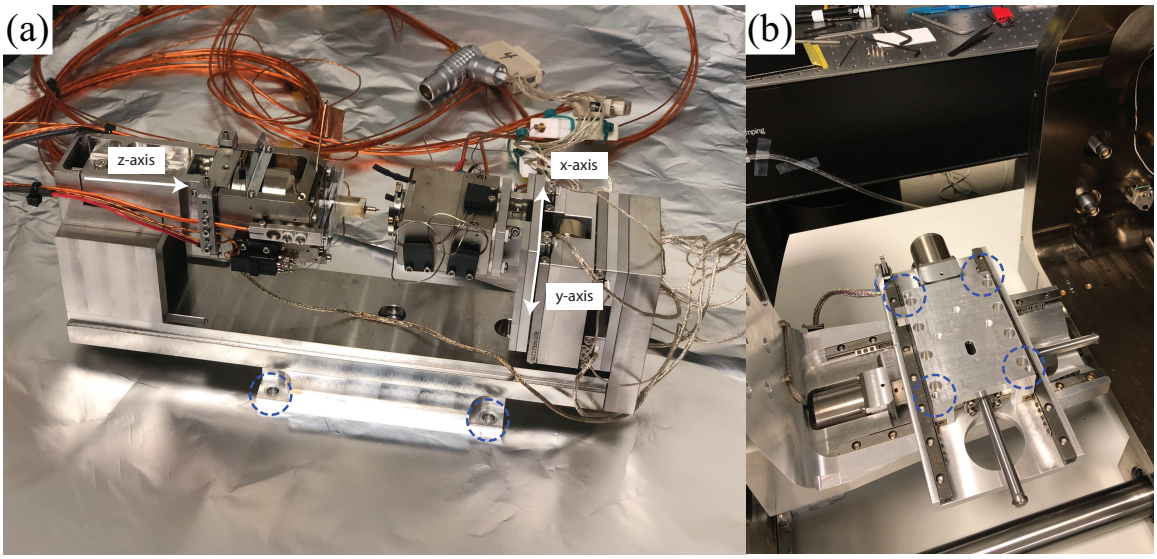

Figure 2.14: The InSEM cradle setup and mounting scheme. (a) Actuator and sample heater are installed on the cradle. The tip side is able to extend/retract along the z-axis, and the ample side allows movements on the x-y plane for accurate align tip with the micro specimen. (b) The SEM stage after the rotational substage has been removed, revealing a flat area for mounting the cradle. The holes, marked by dashed circles in (a) and (b), are for the mounting screws.

2.5.3 Issues Associated with High Temperature Nanomehcanical Testing

In situ nanomechanical testing of materials at elevated temperature has been an emerging field that attracts an impressive amount of attentions for its scientific and economical significance. However, there are a few challenges/issues that need to be addressed/alleviated in order to get accurate measurement of material properties.

First of all, thermal drift, including frame drift and contact drift, will be exaggerated at elevated temperatures due to the magnified inhomogeneous distribution of temperature within the system [63]. Secondly, the determination of true contact temperature, which comes from engineering difficulties of measuring temperature at the tip contact location. Last but not least, oxidization of the sample and indenter tip is largely suppressed if testing is carried out in high vacuum, for example, inside an SEM chamber [104]. The methods and protocols to tackle the first two issues are discussed in this subsection.

Frame drift is caused by expansion or contraction of components due to thermal gradients and fluctuations and exists at both room and elevated temperatures. At room temperature, this can be minimized by thermally buffering the tester from its surroundings, and corrected by incorporating a hold period [**?**]. Our SEM based testing system is less susceptible to this issue due to its the high vacuum and high thermal conductivity of the frame at room temperature. At higher temperatures, due

to the active heating and cooling, the thermal gradient can not be eliminated. Thus, a stabilization period is required until the thermal gradient becomes steady. It has been reported that the actual time is on the order of 1 to a few hours and dependent on the testing temperature, and the physical design of the system [63]. Generally, if the testing period is small compared to the time required for stabilization, its effect will be limited.

Contact drift is the most significant and common issue for achieving accurate measurements at high temperature. It is attributed to the temperature difference between tip and sample and occurs when heat transfer happens during contact. Consequently, it causes local temperature and volumetric variations which are undesirable. At room temperature, this effect is almost negligible; however, at elevated temperature, it's practically impossible that the sample and tip are heated to identical temperatures just by simply setting them to the same temperature on the temperature controller.

To eliminate such issues, an explicit temperature matching procedure is required. There are two methods proposed by Wheeler et al. [63] and both are based on indentation. In the first method, the sample temperature is maintained and a series of indentations are performed at various tip temperatures until a minimum drift is found. In the second method, the indenter side heat is set to a constant power, while indenting and recording the temperature variation on the tip. The relative temperature can be interpolated based on the direction of the shift. A (near) zero shift will be achieved when isothermal contact is reached, thus thermal mismatch is eliminated.

The above method can effectively avoid the thermal mismatch, however, it does not guarantee both sides are heated exactly to the target temperature. This is due to the fact that the tip side thermocouple is attached to the base of the tip and not at the very end of tip, the actual tip temperature will be lower than target temperature. For systems where the thermocouple is placed far way from the tip, this difference will be magnified. Wheeler and Michler [105] introduced two methods to quantify the gradient and to calibrate the true contact temperature. The first method is to indent on thermocouple, and with the surface temperature of thermocouple being known, the relative temperature can be determined by either the displacement or temperature shift in the tip [106]. The second approach is to use non-contact techniques, including Raman spectroscopy and an infrared camera.

2.5.4 Minimization of Thermal Mismatch

The previous subsection presented the main issues in high temperature testing and ways to combat them. However, the design of indentation systems, especially the temperature controlling components can vary significantly. In this subsection, the best protocols, as inspired by above described methods, which appl to the InSEM system are discussed to minimize the thermal mismatch.

The general idea proposed by Phani and Oliver [107] is to use a cyclic indentation experiment, while monitoring temperature shift. The following description and data are based on microcompression tests at 300 °C. It should be noted it is assumed that

the tip nominal temperature is the true contact temperature because the thermocouple is designed to locate very close to the tip (as shown in Figure 2.12). The procedure is summarized here:

1. Turn on water pump and ensure the water is flowing and pump the SEM chamber.

2. Turn on the temperature controllers and activated the outputs. The red light indicating active outputs are on. (shown in Figure 2.16)

3. Set the tip to the testing temperature, 300 °C in this case, and let it stabilize for 5 min.

4. Heat the sample to the testing temperature at a rate of 20 °C/min to 30 °C/min and let it stabilize for 5 min.

5. Adjust the PIDs in the controllers until stability is reached. Suggested parameters are:

Tip heater	Tip cooler	Sample heater	Sample cooler
P=1 I=2 D=0	P=5 I=5 D=0	P=1 I=2 D=0	P=5 I=5 D=0

6. Ramp up sample side temperature at a rate of 1 °C/min to 2 °C/min.

7. Run cyclic indentation method on a location far enough from the location for actual testing and record data.

8. Determine the isothermal contact temperature based on the recorded data in cyclic indentation and use it as the input temperature for experimentation.

In this cyclic indentation method, the indenter starts with an instantaneous force of 25 mN to achieve full contact between the punch and sample surface. After holding it for 30 s, a negative 25 mN force is applied to fully retract indenter column. Another 90 s holding period is used to allow the tip return to the original temperature (i.e., 300 °C in this case), the same procedure will be repeated until the sample side temperature is high enough.

During contact, heat transfer will happen immediately if the tip and sample temperatures are different. If the tip is hotter than the sample, a drop in tip temperature will be observed along with an increase in actuator displacement. This is because a decrease in temperature will lead to thermal contraction of the indenter tip and the displacement will have to accommodate this contraction. Either thermal drift or temperature shift direction can be used to quantify the relative temperature, since the InSEM HT system has very good temperature sensitivity, so the temperature change is used as a indicator for relative temperature between the tip and sample.

Recorded data from the above experimental procedure are shown in Figure 2.15. It is observed that sample side temperature is gradually increase from 305 °C to 370 °C in $\sim$ 45 min, while the tip was cyclically indented into the sample surface. Figure 2.15(b) shows when the sample temperature is low (i.e., below 330 °C), and once the tip the touches sample, a significant drop in sample temperature is observed. As the

temperature increases, the temperature variation becomes smaller. When the sample exceeds 360 °C, an increase in tip temperature is observed which indicates that the sample is hotter than the tip. Using this temperature variation data, the isothermal contact temperature can be determined, and in this case is 358 °C. This also suggests a big thermal gradient (358 °C at bottom and 300 °C at the top of a 5 mm thick sample) and a temperature calibration and matching process is necessary.

A brief introduction of the temperature controlling module for easy operation is also included here. As shown in Figure 2.16(a), two temperature controllers are located on the top level with four power supplies beneath them. Each controller has a display, which gives the current temperature acquired from thermocouple and target temperature (shown in Figure 2.16(b)). The buttons in white dashed lined region are used to set the PID parameters and the target temperatures for both heating and cooling circuits. There are two power indicators (red dashed line region) that shows the status of heating and cooling loops, respectively. Current status in the figure shows controller is on but output has not been activated.

2.5.5 Stress-strain Calculation

In this subsection, a few commonly used concepts, measurements and calculations for small-scale testing are summarized.

Engineering stress/strain

Engineering stress, σ, is defined as the applied load divided by the original cross-

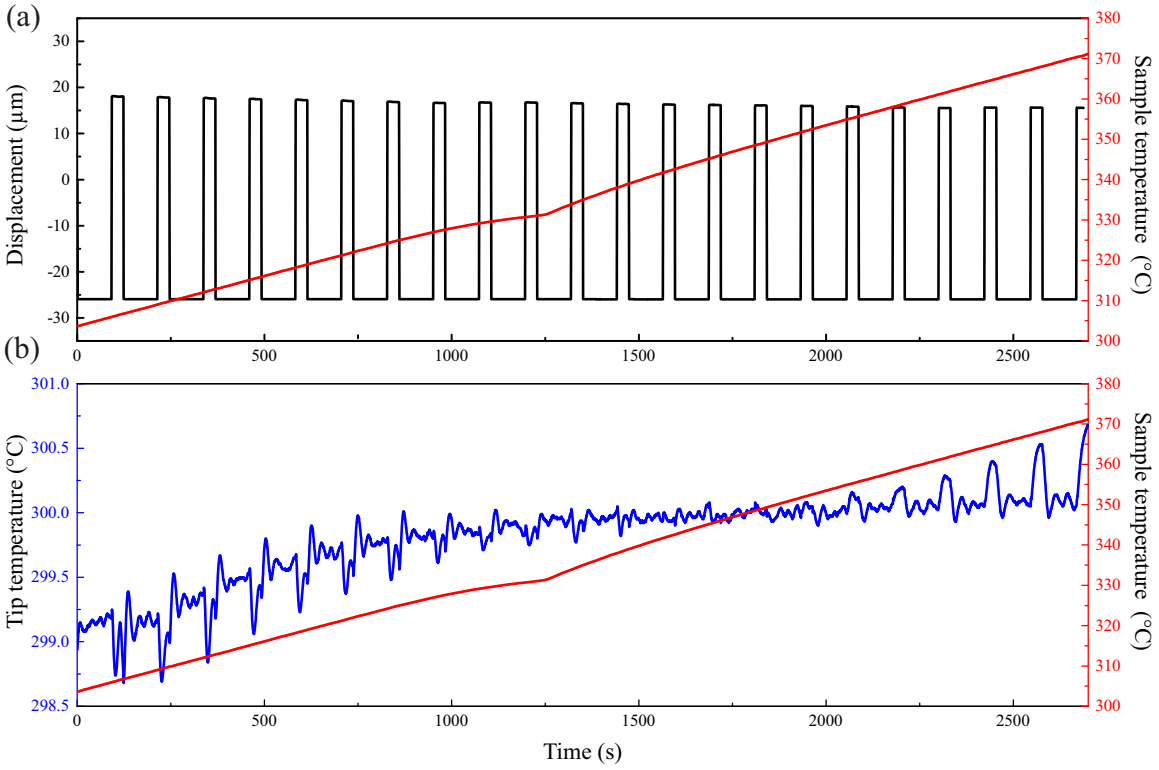

Figure 2.15: Displacement, tip temperature and (nominal) sample temperature data collected during the cyclic indentation process used for minimizing the tip and sample surface temperature mismatch. (a) Displacement and (nominal) sample temperature are plotted as a function of time . (b) Tip temperature and (nominal) sample temperature is plotted are a function of time.

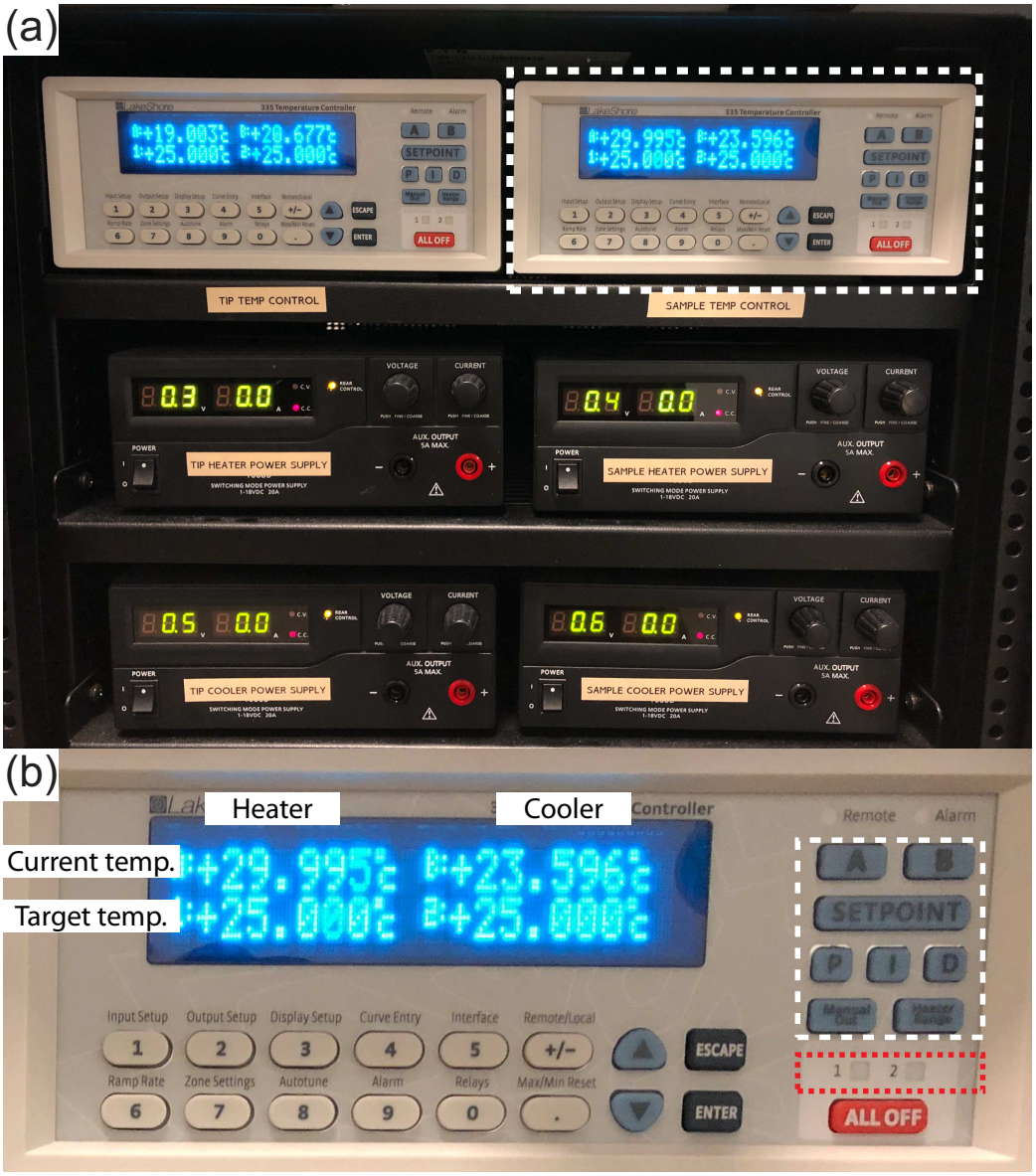

Figure 2.16: The InSEM temperature control tower/module: (a) Full view of Lakeshore temperature controller on the top level and heater/cooler power supply on second and third levels; (b) zoom-in of dashed line region to show the detail of the panel.

sectional area of the material which is also named as nominal stress. Accordingly, the engineering strain, e, is defined as the ratio of total deformation to the initial dimension of the material, for a uniaxial load, this is expressed as

$$e = \frac{\Delta L}{L} = \frac{l - L}{L} \tag{2.5.1}$$

where L is original length of the specimen.

True stress/strain

True strain, ε, also called *logarithmic strain*, which represent the rate of instantaneous increase in the gauge length during a unixial test:

$$\delta\varepsilon = \frac{\delta l}{l} \tag{2.5.2}$$

Integration of both sides gives,

$$\int \delta\varepsilon = \int_L^l \frac{\delta l}{l} \tag{2.5.3}$$

Finally,

$$\varepsilon = \ln(\frac{l}{L}) = \ln(1 + e) \tag{2.5.4}$$

Accordingly, the true stress, σ_t, is given as

$$\begin{aligned} \sigma_t &= \frac{P}{A} \\ &= \frac{P}{A_0} \times \frac{A_0}{A} \\ &= \sigma \times \frac{l}{L} \\ &= \sigma(1 + e) \end{aligned} \tag{2.5.5}$$

Base compliance correction

For microcompression experiment, the measured raw displacement from the indenter is comprised of two components, including that accommodated by the pillar and that by the base, such that

$$u_{tot} = u_{pillar} + u_{base} \tag{2.5.6}$$

The component u_{base} is based on Sneddon's solution of Boussinesq problem, where an rigid punch imposing a force on a semi-infinite flat isotropic surface [108]. The relationship between the load is F, and penetration depth is u, can be shown to be

$$u = \frac{F(1-v)}{4\mu a} \tag{2.5.7}$$

where μ is the shear modulus and v is the Poisson's ratio. With mathematical manipulation and using the linear elastic theory, the base compliance can be shown to be [109]

$$C_{Sneddon} = \frac{\sqrt{\pi}(1-v^2)}{2E\sqrt{A}} \tag{2.5.8}$$

where E is the Young's modulus and A is the instantaneous cross-sectional area of the micropillar. Thus, d_{pillar} can be calculated as

$$u_{pillar} = u_{tot} - \frac{\sqrt{\pi}(1-v^2)}{2E\sqrt{A}} * F \tag{2.5.9}$$

The engineering strain can then be calculated using Equation 2.5.1. The indentation system used in the current work is inherently load-controlled, so a constant loading rate is used in all the experiments.

Chapter 3

Micro-mechanical characterization of tungsten coating: from ambient to elevated temperature

3.1 Micro-compression Response at Room Temperature

Microcompression experiments were conducted on micropillar specimens FIB milled into individual curds in the micro-architectured W coating to investigate its stress-strain response, fracture, and mechanical properties at room temperature.

The microspillars have diameters, D, in the range of $2.0 \leq D \leq 10.0\,\mu m$ and

aspect ratios from 2 to 4.6. The micropillar diameter is measured from the top surface based on SEM micrographs. The experiments were conducted first *ex situ* using an MTS Nano XP nanoindenter equipped with a 30 µm × 30 µm square flat-ended diamond tip and at a nominal strain rate of 10^{-4} s^{-1}. In addition, an *in situ* microcompression test was performed on a $D = 8.5\,\mu m$ micropillar specimen using an InSEM HT nanoindenter inside a Tescan Mira 3 SEM as described in Chapter 2.

3.1.1 Response of Micropillars Having D ∼ 2.5 µm

The engineering stress-strain response of microcrystals having $D \sim 2.3\,\mu m$ are shown in Figure 3.1. The flow stress at 2% strain is observed to be in the range of 1.5 to 1.9 GPa. The wide scatter in the yield stress can be attributed to variations in the local microstructure, since the crystal size is only twice the average grain size of the coating, and the number of grains in the pillar are limited. Additionally, it should be noted that since the aspect ratio of all tested pillars is in the range of 2.0 to 4.8, all pillars are exclusively in the top most layer of the micro-architectured W coating.

Two distinct deformation modes are observed based on the pillar aspect ratio. Pillars having an aspect ratio of $L/D \leq 3.0$ are observed to deform plastically with continuous linear work-hardening as shown in Figure 3.1. While preexisting voids and cracks are observed in the predeformed microcrsytals (c.f., Figure 3.2(a)), no fracture is observed in any of the tested microcrystals and the deformed microcrystals is observed to be barrel-shaped, as shown in Figure 3.2(b). It should be noted that

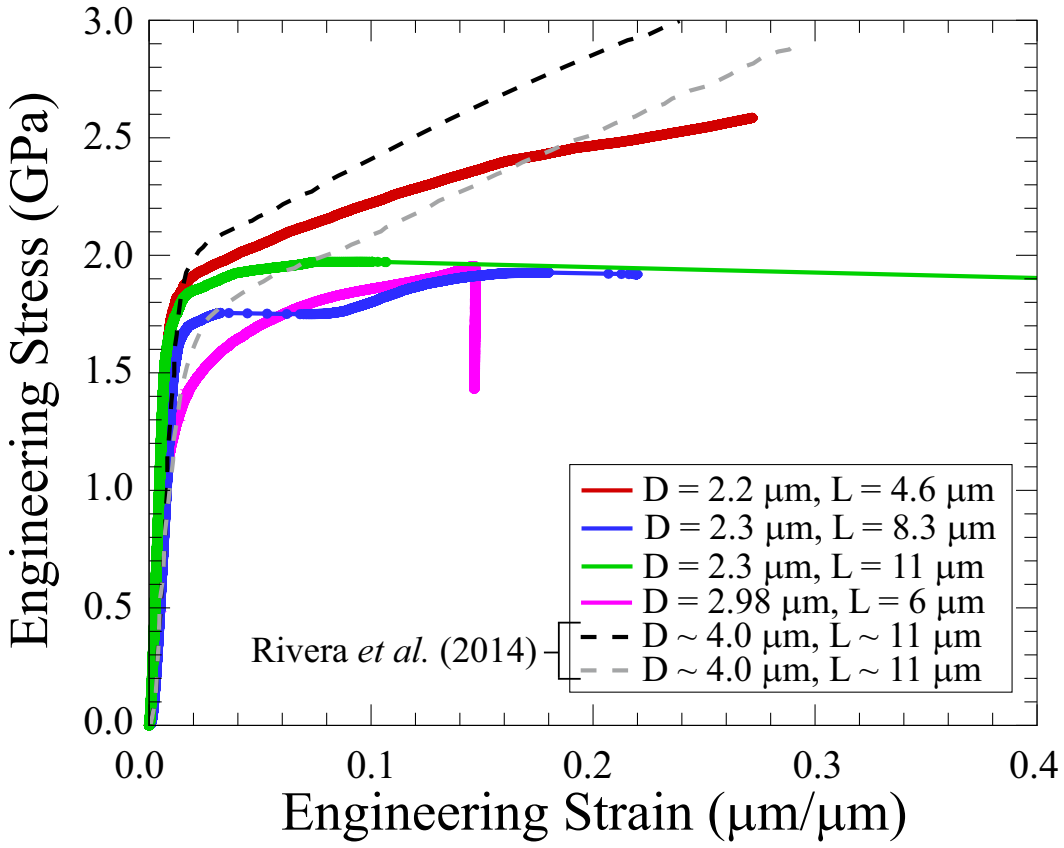

Figure 3.1: Engineering stress versus strain curves for microcrystals having D $\simeq$ 2 µm. Experimental results of micropillars fabricated into a dense UFG polycrystalline W are shown as dashed lines for comparison [3].

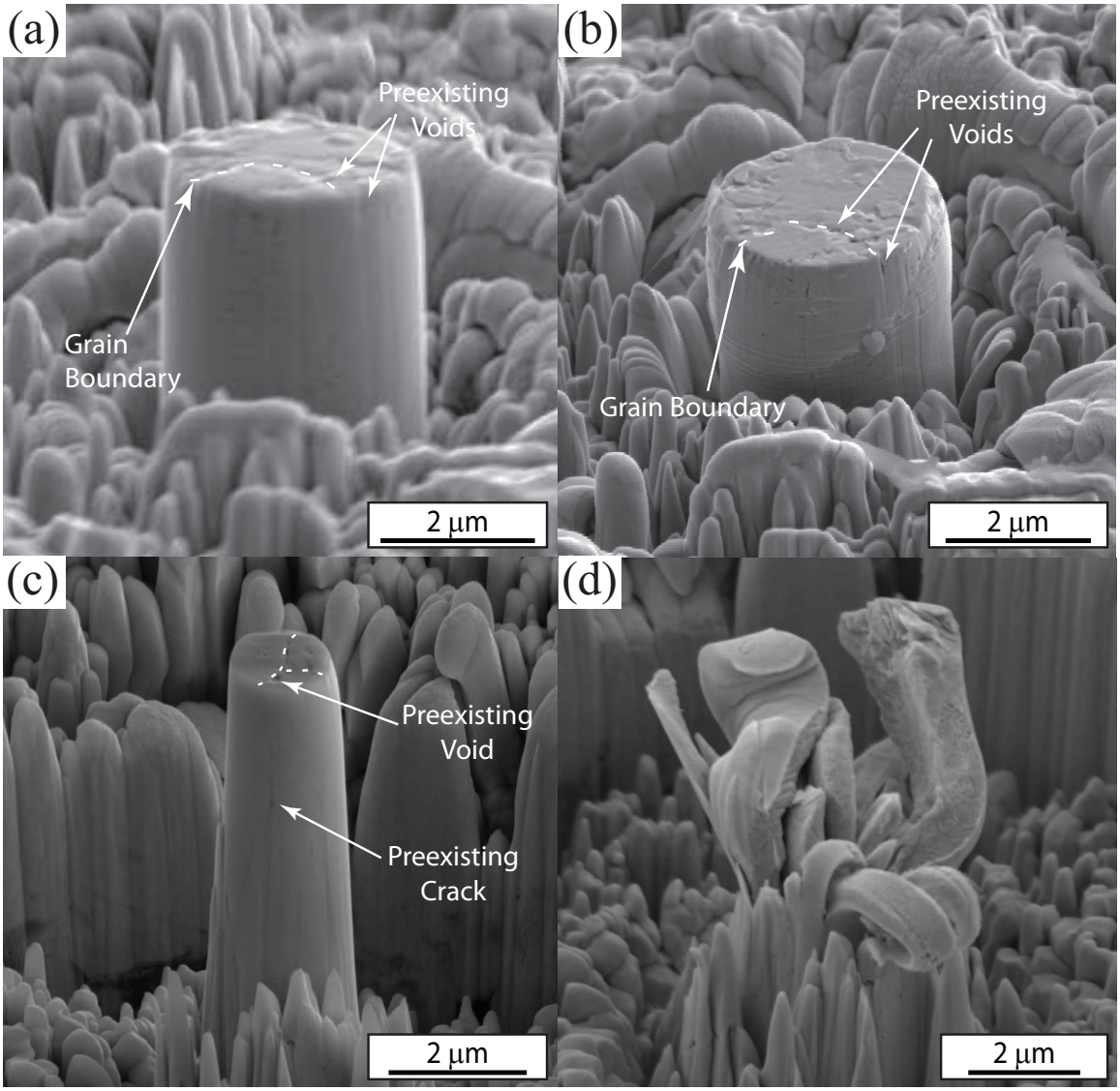

Figure 3.2: (a) and (b) show the SEM micrographs of the D = 2.2 µm and L = 4.6 µm microspecimen pre- and post-deformation, respectively. (c) and (d) show the SEM micrographs of the D= 2.3 µm and L=11 µm pre- and post-deformation, respectively. The dashed lines in (a) through (c) indicate apparent grain boundaries on the top surface of the micropillars. Apparent cracks and voids along the grain boundaries on the top surface and side surface are also indicated.

the flow stress at 2% strain of these microcrystals are in good agreement with those reported for $\sim 4\,\mu m$ micropillars fabricated in dense UFG W samples but with a lower hardening rate [3]. This lower hardening rate in the current experiments can be attributed to the voids present along the grain boundaries in the current study. Additionally, the texture is different and the average grain size is much smaller ($\sim 0.3\,\mu m \times 2.5\,\mu m$ along loading and transverse directions) in the dense polycrystalline micropillar case (i.e., more grains through the cross-section).

On the other hand, microcrystals having an aspect ratio $3.0 \leq L : D \leq 4.8$ show a different engineering stress-strain response and post-mortem deformation shape. After yield, no strain hardening is observed and strain bursts are frequent. Furthermore, in some cases a significant strain burst is also observed leading to an instantaneous collapse of the microspecimen. The SEM micrographs of the pre- and post-deformed micropillar of the latter case are shown in Figures 3.2(c) and (d), respectively. The postmortem deformation shape shows that each individual grain that comprised the microcrystal has deformed independently and the microspecimen has catastrophically failed with cracks propagating along all grain boundaries. The observed "S" shape of each defromed grain indicates that plastic buckling of each grain was predominant. The different deformation modes are attributed to the inherent columnar microstructure and is explained as follows. The grain structure in the current W coatings are elongated and have an average in-plane grain size of $\sim 1\,\mu m$, so only a few grains are expected through the micropillar cross-section. As shown in Figure 2.5(b), the elon-

gated grains have a length in the range of 10-12 µm. Thus, in microcrystals having $D \leq 3.0$ µm with an aspect ratio $2.0 < L : D \leq 4.8$ only very few grains are expected. For microcrystals with aspect ratio $3.0 < L : D \leq 4.8$, the microcrystal height is on the order of $6 \leq L \leq 14.5$ µm. This means that the aspect ratio of individual grains in these microcrystals will be in the range of 6.0 to 14.0. Furthermore, given the existence of voids and cracks along the grain boundaries, when the applied stress is high enough for these cracks to propagate along the grain boundaries, each grain will subsequently act as an individual pillar with a high aspect ratio leading to plastic buckling dominated deformation, as shown in Figure 3.2(d). The strain bursts observed can be attributed to grains slipping onto each other after crack propagation, or the plastic buckling of individual grains. On the other hand, for microcrystals having an aspect ratio of $L : D \leq 3.0$, the aspect ratio of individual grain will be at most 6. In this case individual grains will have less susceptibility for plastic buckling, and instead each grain deforms plastically. The presence of grain boundaries are expected to contribute to the observed hardening behavior without strain bursts.

3.1.2 Response of crystals having D $\sim$ 4.5 µm

The engineering stress-strain curves for microcrystals having diameters ~ 4.5 µm are shown in Figure 3.3. All tested microcrystals had an aspect ratio of ~ 2.6, thus, they are exclusively in the top most micro-architectured layer. For this micropillar size, no strain hardening and large strain bursts are typically observed. Pre-

deformation SEM micrographs of the pillars indicate the presence of many cracks and voids along the grain boundaries. Post-mortem SEM micrographs show that these microspecimens have failed by intergranular fracture along the grain boundaries, followed by plastic buckling of the columnar grains, as clearly indicated by the S-shape of the deformed grains shown in Figures 3.4(b) and (d).

3.1.3 Response of Samples Having D $\sim$ 8.5 µm

The engineering stress-strain curves for microcrystals having $D \sim 8.5\,\mu m$ are shown in Figure 3.5. All micropillars exhibit a continuous stress-strain response with parabolic work-hardening and very few strain bursts that are only observed at high strain levels. The post-mortem deformation shape of two different microspecimens are shown in Figure 3.6(b) and (d). As in the case of smaller-sized micropillars, all microspecimens failed by intergranular fracture along the grain boundaries. The deformed shape displays a petal-like morphology, where the microcrystal top is fully opened, while the bottom is partly intact with fracture not propagating through the entire hight. For all the tested crystals, the aspect ratio is on the order of 1.8 to 2.2, which indicates that these microspecimens span through the two top micro-architectured layers of the W coating. This can be identified from the outer surface of the microcrystals before deformation, as shown in Figures 3.6(a) and (c). At least a couple of columnar grains can be observed through the height of the microcrystals, with most grain boundaries decorated with large voids. In addition, a few grains are

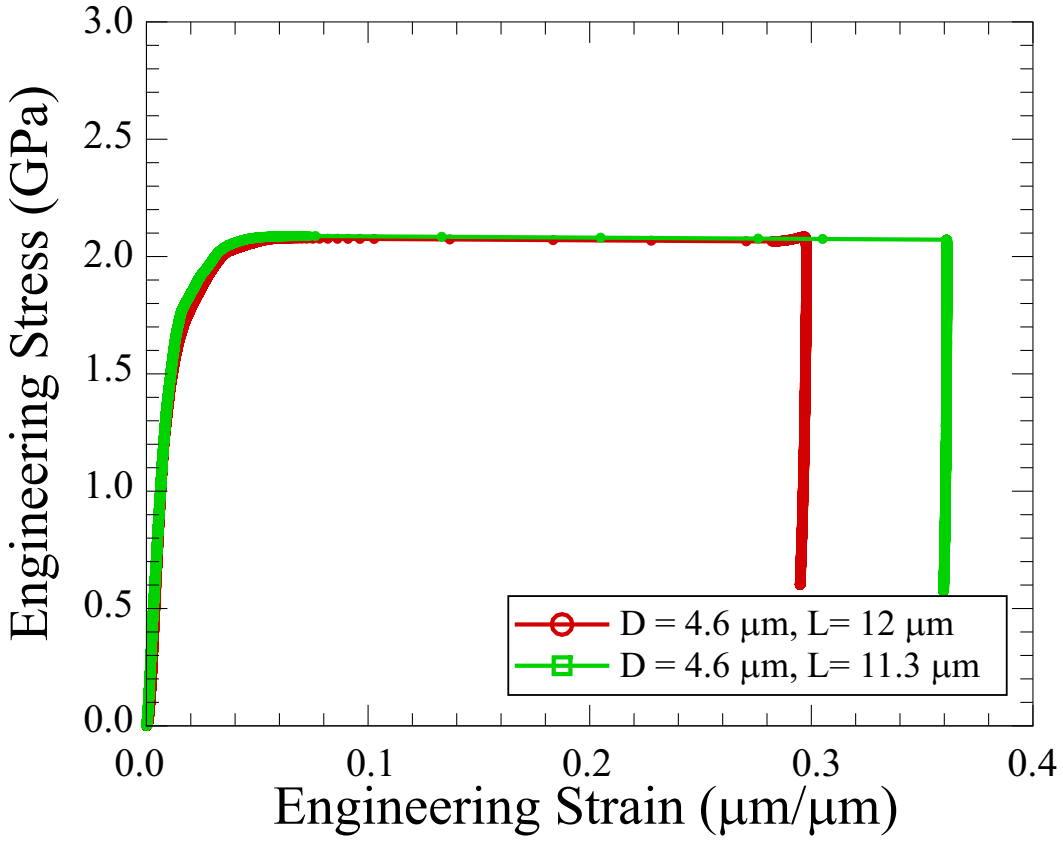

Figure 3.3: Engineering stress versus strain curves for microcrystals having D$\sim$ 4.5 µm.

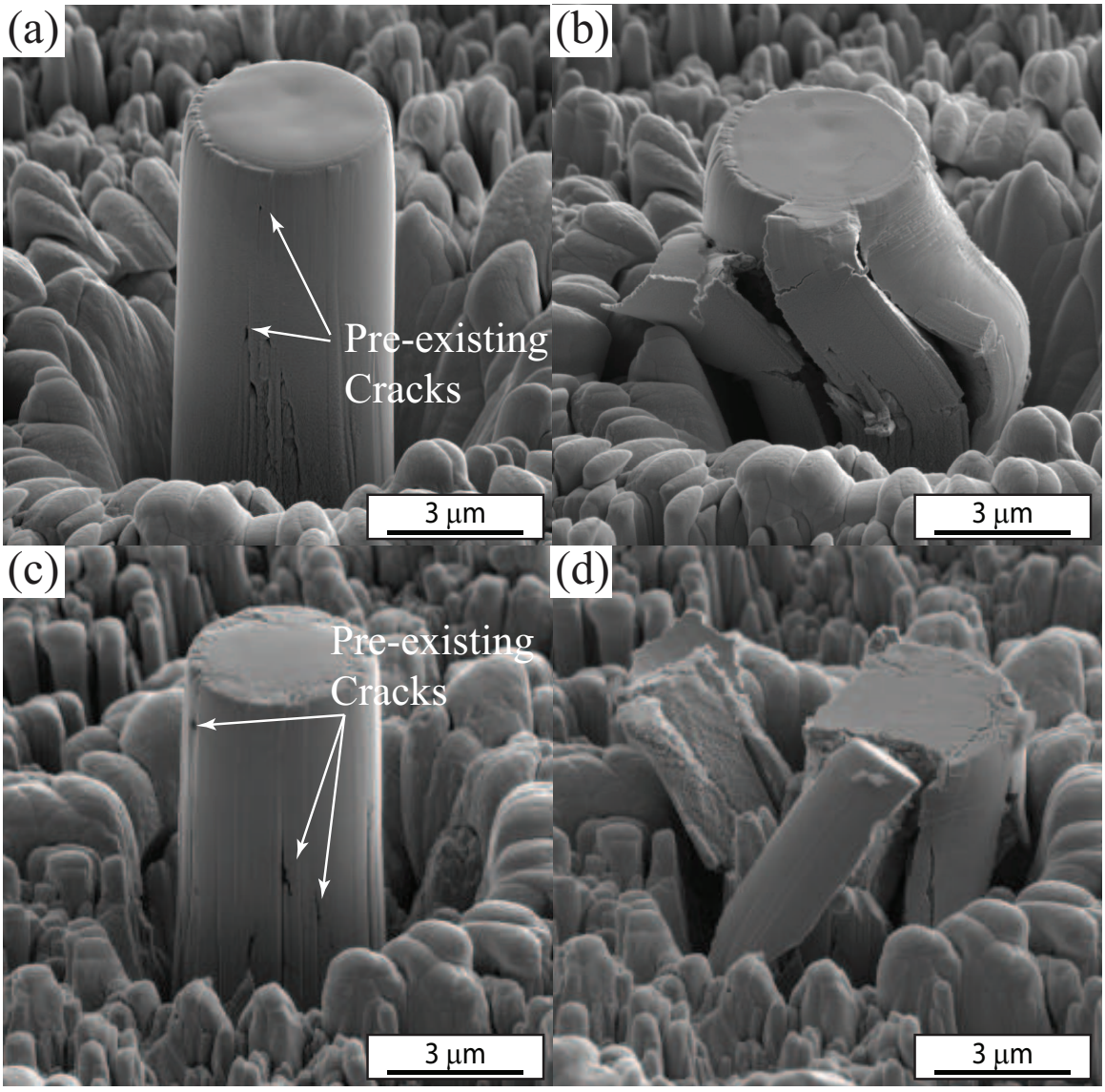

Figure 3.4: (a) and (b) show the SEM micrographs of the D=4.6 µm and L=12 µm microcrystal pre- and post-deformation, respectively. (c) and (d) show the SEM micrographs of the D=4.6 µm and L=11.3 µm microcrystal pre- and post-deformation, respectively. Arrows indicate pre-existing cracks along different grain boundaries.

expected through the diameter of these microcrystals.

To further understand the deformation, an *in situ* experiment was performed on a micropillar having $D = 8.2\,\mu m$ with an aspect ratio of 2.0. The engineering stress-strain response and the SEM micrographs at different stages during the deformation are shown in Figure 3.7. It is shown that no apparent change is observed on the microcrystal other than slight change in length between during elastic loading regime (i.e., ① to ②). Starting from ② the stress-strain response starts to deviate from linear which indicats the onset of plastic deformation. At ③, the microspecimen is observed to be slightly barrel-shaped to accommodate the deformation but no sign of crack can be identified. As the micropillar continues to be strained, the first intergranular crack is observed to initiate at ④ on the outer surface, and these cracks propagate vertically along the grain boundaries (as shown in ⑤). Subsequently, at point ⑥, full delamination of surface grains are observed followed by bucking of these exterior grains.

3.1.4 Size Effects on the Flow Strength

The microcrystal size versus the flow strength at 2% strain for all the tested microspecimens are shown in Figure 3.8. It is observed that the smaller crystals show a stronger response, and the scaling relationship for the flow strength with the diameter is a power law with an exponent of -0.18. It is worth noting that for single crystal W microcrystals the flow strength versus crystal size exponent at

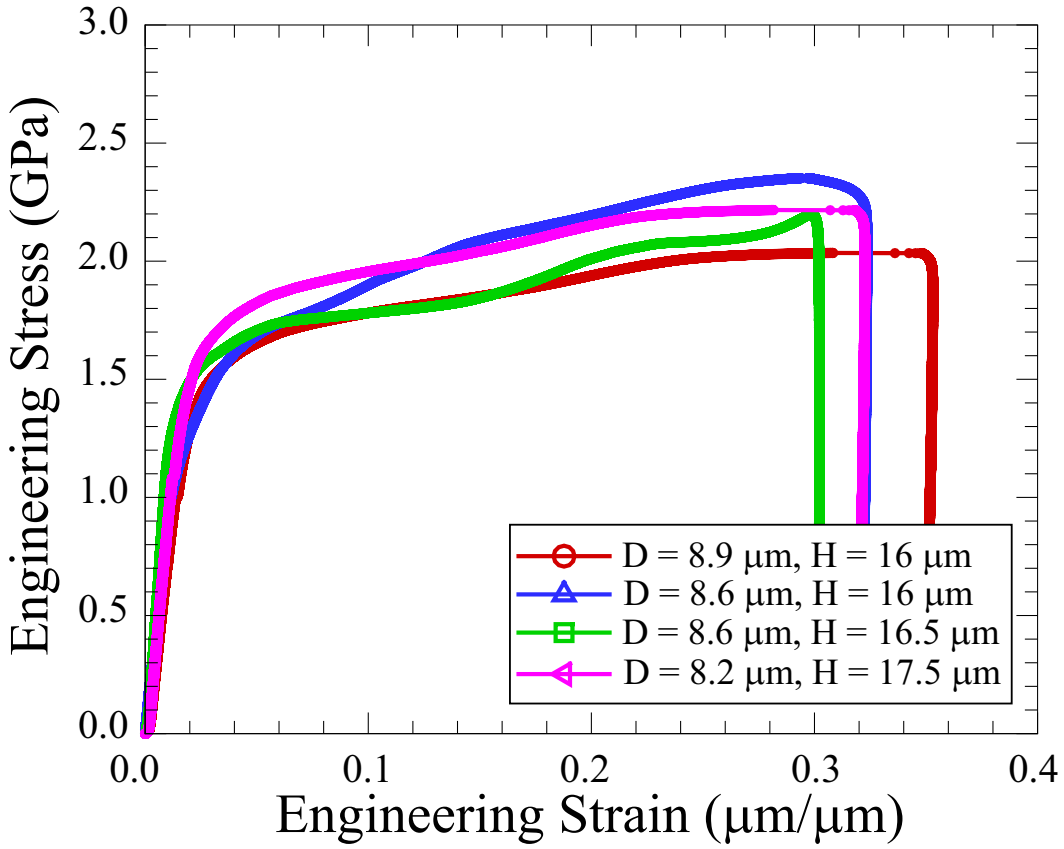

Figure 3.5: Engineering stress versus strain curves for microcrystals having D$\sim$ 8 µm.

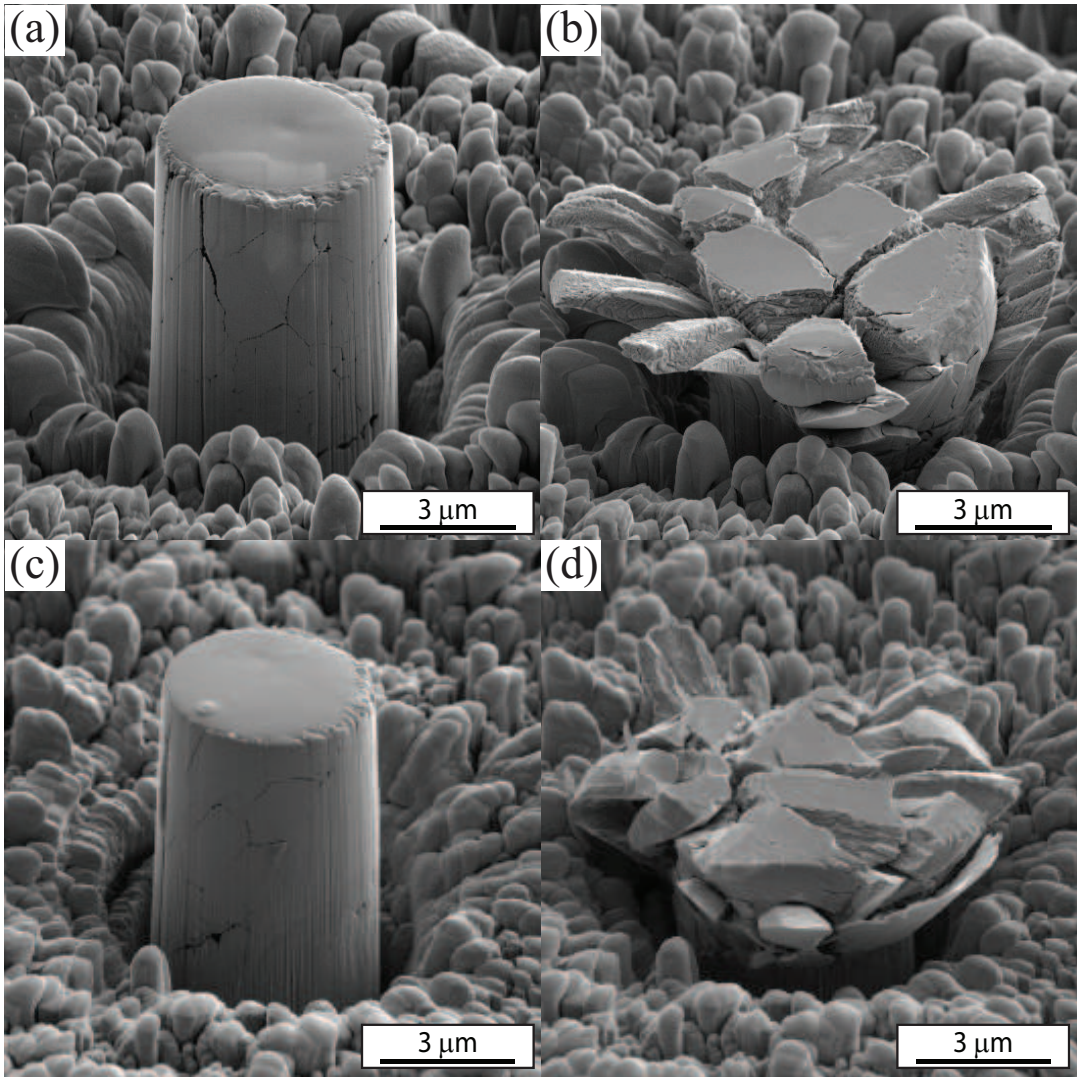

Figure 3.6: (a) and (b) show the SEM micrographs of the D=8.6 µm and L=16 µm microcrystal pre- and post-deformation, respectively. (c) and (d) show the SEM micrographs of the D=8.9 µm and L=16 µm microcrystal pre- and post-deformation, respectively.

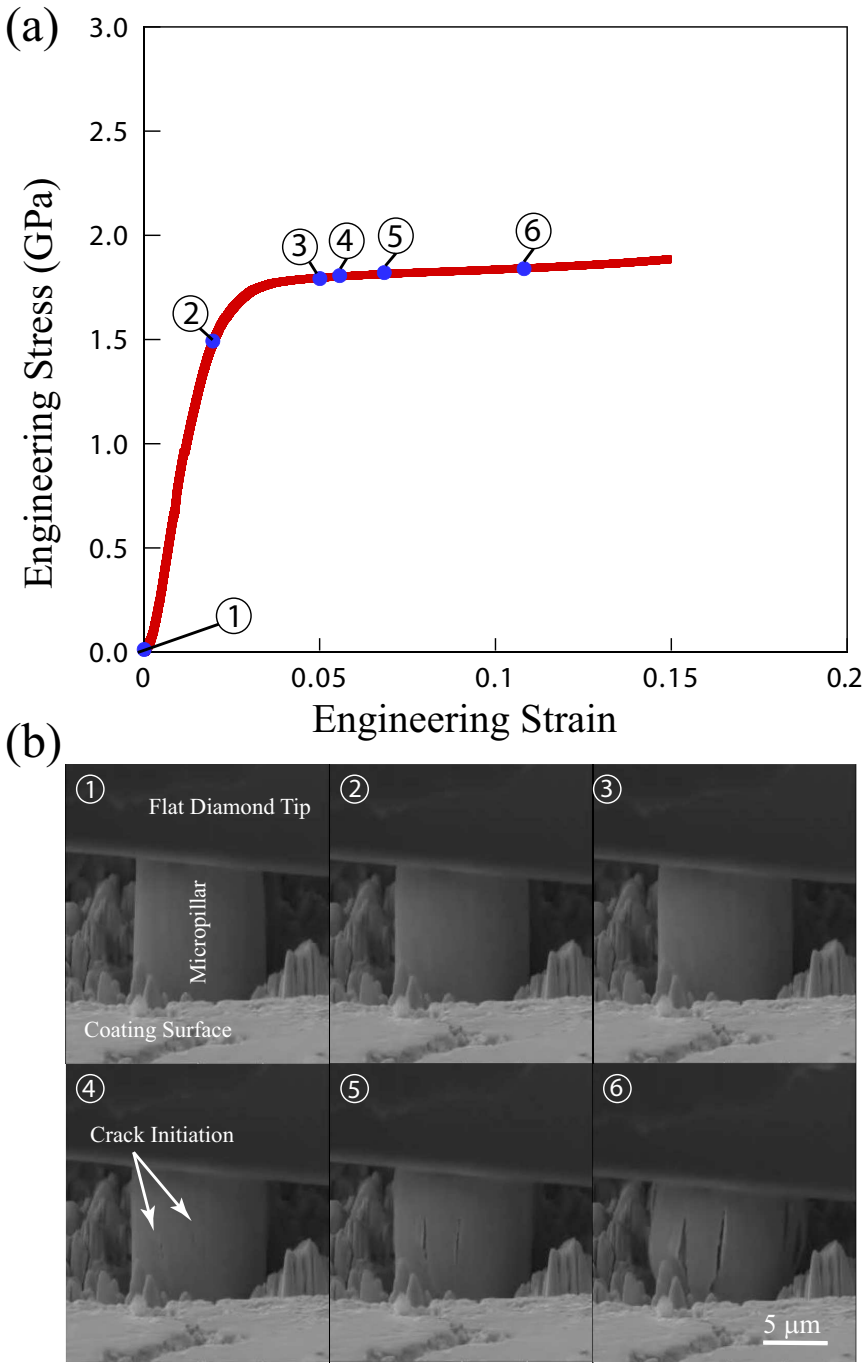

Figure 3.7: (a) The engineering stress-strain curve from *in situ* microcompression experiments for a microspecimen having D=8.2 µm and an aspect ratio of 2. (b) The SEM micrographs at different strains during the deformation process. The circled numbers in (a) and (b) show the strain level at which the corresponding SEM micrograph was taken at.

room temperature is typically in the range of ~ -0.3 [4, 19]. However, it should be noted here that the observed size effects in the current study is unlikely due to size-dependent dislocation-mediated plasticity typically observed in single crystals [83]. Instead, it is more likely attributed to the variations in the local microstructure (i.e., grain size, texture, pre-existing voids at grain boundaries, etc.). In addition, the large scatter in the results indicates that this local microstructure varies significantly from one position to another, which indicate the need to quantify the statistical variations of the pre-existing voids and their effect on the mechanical properties.

3.1.5 Summary of the Room Temperature Micro-compression Response

Based on the *ex situ* and *in situ* observations, we propose the following mechanisms of deformation in these micropillars. Initially, in the elastic regime, the deformation is relatively homogeneous and grain boundaries are strong enough to carry the applied force. As the load increase the grain boundaries are weakened leading to local decohesions at pre-existing cracks/voids along the grain boundaries, which act as stress concentrators. In smaller micropillars, only a couple of grains span the diameter of the microcrystal, and most grains have a free surface. Thus, after the initiation of intergranular fracture along the longitudinal grain boundaries, plastic buckling of each grain is relatively unconstrained. On the other hand, for large microcrystals only

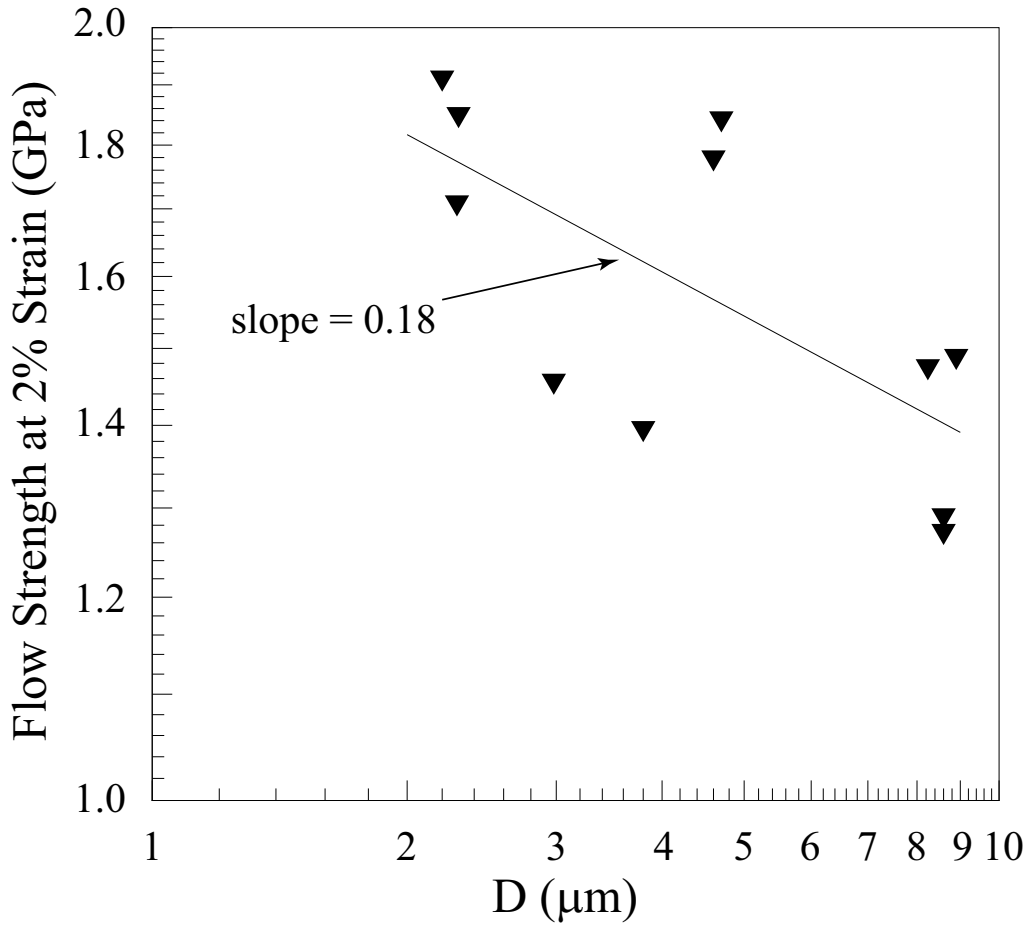

Figure 3.8: The microcrystal size, D, versus the flow strength at 2% strain for all the tested microcrystals. The solid line shows the best power law fit to the data with an exponent of -0.18.

grains on the outer surface of the microcrystal are unrestricted, while the internal ones are confined. After fracture initiates along the grain boundaries, the surface grains can buckle, while the inner grains can still carry the applied load. As such, no strain bursts are observed. When the applied load is large enough to overcome the friction between the top surface of the microcrystal and the nanoindenter punch, the surface grains that are plastically buckling will begin to open up allowing the interior grains to subsequently buckle. At this stage the strain bursts are observed. Furthermore, the number of grain boundaries in larger microcrystals are more than those in smaller microcrystals. As such, it is expected that the fracture along the grain boundaries and subsequent instabilities/buckling events will initiate in a consecutive way instead of spontaneously as observed in smaller microcrystals. Thus, the large strain bursts observed in smaller microcrystals are no longer exhibited.

3.2 Micro-compression Response at Elevated Temperature

In the previous section, room temperature micro-compression has been carried out on the micropillar specimens FIB milled into the micro-architectured W coating's individual curds in oder to quantify the mechanical response. It is shown the W coating exhibits an excellent mechanical strength above 1.5 GPa at room temperature, and that failure occurs catastrophically by buckling-assisted intergranular fracture.

Additionally, we have shown that this failure initiates shortly after the onset of plastic deformation and is predominantly due to the high aspect ratio of the coating's columnar grains, the high fraction of pre-existing defects at the grain boundaries, and the inherent brittleness of W at room temperature.

While such studies are informative regarding the deformation and failure modes of these coatings at room temperature, the true potential of these coatings is at elevated temperatures. Thus, it is crucial to extend such studies to further quantify the deformation and failure modes of these coatings at elevated temperatures. Accordingly, here, we utilize elevated temperature micro-compression *in situ* SEM experiments to quantify the thermo-mechanical properties and deformation of these coatings. Such elevated temperature *in situ* micro-compression experiments have also been previously used to study the temperature-affected deformation mechanisms of thin films [64, 110].

It should be noted along with a strongly temperature-dependent yield strength, W usually experiences a so called brittle-to-ductile (BDT) transition at a characteristic temperature, $T_{BDT} \sim 600 - 700$ K [111]. At room temperature, brittle failure is commonly observed in tension; however, with increasing temperatures the fracture mode gradually transitions to ductile due to the activation of thermally activated mechanisms (e.g., dislocation slip). In general, the BDT temperature reflects the macroscopic mechanical behavior of the material. Moreover, many experimental efforts have shown that the T_{BDT} temperature cannot be considered as an inherent

physical property of the material, and instead it depends in general on the material microstructure, sample geometry, and testing method [111, 112].

In this section, *in situ* micro-compression experiments were conducted using the InSEM HT (Nanomechanics Inc., Oak Ridge, TN) indenter inside a Tescan Mira 3 SEM as described in Chapter 2. As the instrument is inherently load-controlled, all experiments were carried out with a preset loading rate that is equivalent to a nominal strain rate of $\sim 10^{-3}$ s^{-1}. The experiments were conducted at four different temperatures: T = 293 K, 423 K, 573 K, 673 K, and 3 to 5 samples were tested at each temperature. The engineering stress was calculated by dividing the load by the initial mid-plane cross-sectional area, and the engineering strain was computed from the corrected raw displacement of the indenter tip using the method described in Chapter 2.

3.2.1 Experimental results

The engineering stress-strain curves for all tested microspecimens are shown in Figure 3.9. For completeness, the room temperature (RT) response presented previously are also included. A certain amount of scatter on the yield strength is shown at each temperature and it is observed to be more pronounced at lower testing temperature. This scatter is attributed to variations in the microstructure between different microcrystals (e.g., grain size, grain shape, void size and distribution, grain boundary strength, etc.). Nevertheless, these results clearly show that the strength decreases

sharply with increasing temperature, with the yield strength decreasing by 50% from 293 K to 673 K. This trend is commonly observed in W as well as other BCC materials, and is in general attributed to the process of dislocations overcoming the Peierls barrier through thermal-activation [113].

Moreover, a post-yielding transition from limited strain-hardening at low temperatures, characterized by large strain bursts, to a moderate linear strain-hardening response at elevated temperatures is observed in Figure 3.9. At 293 K and 423 K, nearly all tested microcrystals exhibited catastrophic failure marked by large strain bursts, which corresponds to the loss of load-bearing capability after buckling of the individual grains. Even for the ones that exhibited relatively continuous flow without large strain burst, the post-yielding curve is nearly flat indicating that the hardening and load-bearing capability is very limited. On the other hand, at 573 K, the strain bursts are fully suppressed, and instead, continuous plastic flow is always observed.

At 673 K, all tested samples exhibited a noticeable strain-hardening with a slope of $\sim 0.005\ \mu$, where μ is the shear modulus. In contrast, Torrents Abad et al. [4] showed single crystal micropillars having diameters $1\,\mu\text{m} \leq D \leq 5\,\mu\text{m}$ exhibit reduced strain-hardening rate with increasing temperature, and at 673 K, they observed a negative strain-hardening rate in these microcrystals. This distinct difference between the current experiments and previous single crystal W microcrystals is attributed to the polycrystalline microstructure of the micro-architectured tungsten coating. At elevated temperature, dislocation mobility is enhanced due to the decrease in

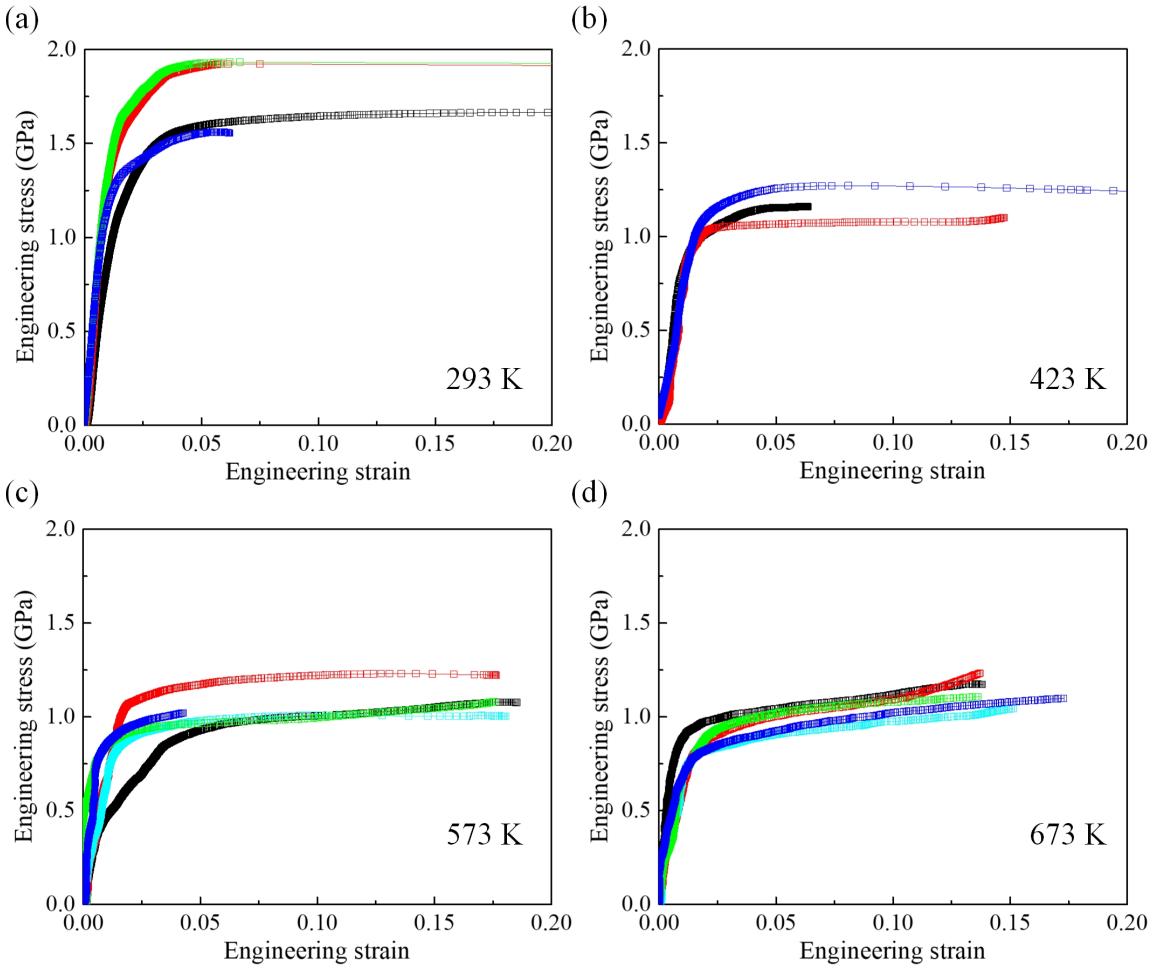

Figure 3.9: Engineering Stress-strain curves of D $\approx$ 5 µm microcrystals at: (a) room temperature; (b) 423 K; (c) 573 K; and (d) 673 K. A few tests were stopped at $\sim$ 5 % strain for later SEM examination of slip traces on the surface. For each temperature, 3-5 stress-strain responses are shown using different color scheme for better visualization.

the critical resolved shear stress (CRSS), and dislocations pile up at GBs instead of escaping from surface which subsequently lead to hardening. A similar behavior has been reported for ultrafine-grained (UFG) body-centered-cubic (BCC) chromium when the testing temperature exceeded the a critical temperature, T_c, above which the flow stress becomes athermal [114].

Representative SEM micrographs at different strain levels during *in situ* deformation at 423 K, 573 K, and 673 K are shown in Figures 3.10, 3.11, and 3.12, respectively. For T $\leq$ 423 K, the microcrystals fracture along the GBs into individual columnar grains that subsequently collapse into the characteristic buckled S-shape (see for example Figure 3.13). This failure mode is attributed to the observed pre-existing voids/pores that are distributed along the GBs as well as the high aspect ratio ($\sim$ 12) of each individual columnar grain. In addition, SEM investigations of the microcrystal surface did not show any clear slip bands forming prior to buckling, which is attributed to the limited plasticity in W at RT [115]. The deformation of a microcrystal at 423 K is shown in Figure 3.10. At 3% strain a crack initiates at one of the pre-existing GB voids and propagates along the GB leading to "peeling off" of that surface grain from the microcrystal. With further deformation, more cracks intiate along the GBs, and if the grain is in contact with the nanoindenter tip it buckles plastically due to the large aspect ratio of the grain, as shown at 9% strain. Eventually, when most of the GBs have fractured the microcrystal catastrophically fails by plastic buckling of the remaining grains. For the microspecimen shown in Fig-

ure 3.10(a) this occurrs shortly after 9% strain and the microcrystal collapses within less than 0.33 seconds, leading to a total of 24% strain. This deformation process is characteristic of all deformed samples at T $\leq$ 423 K.

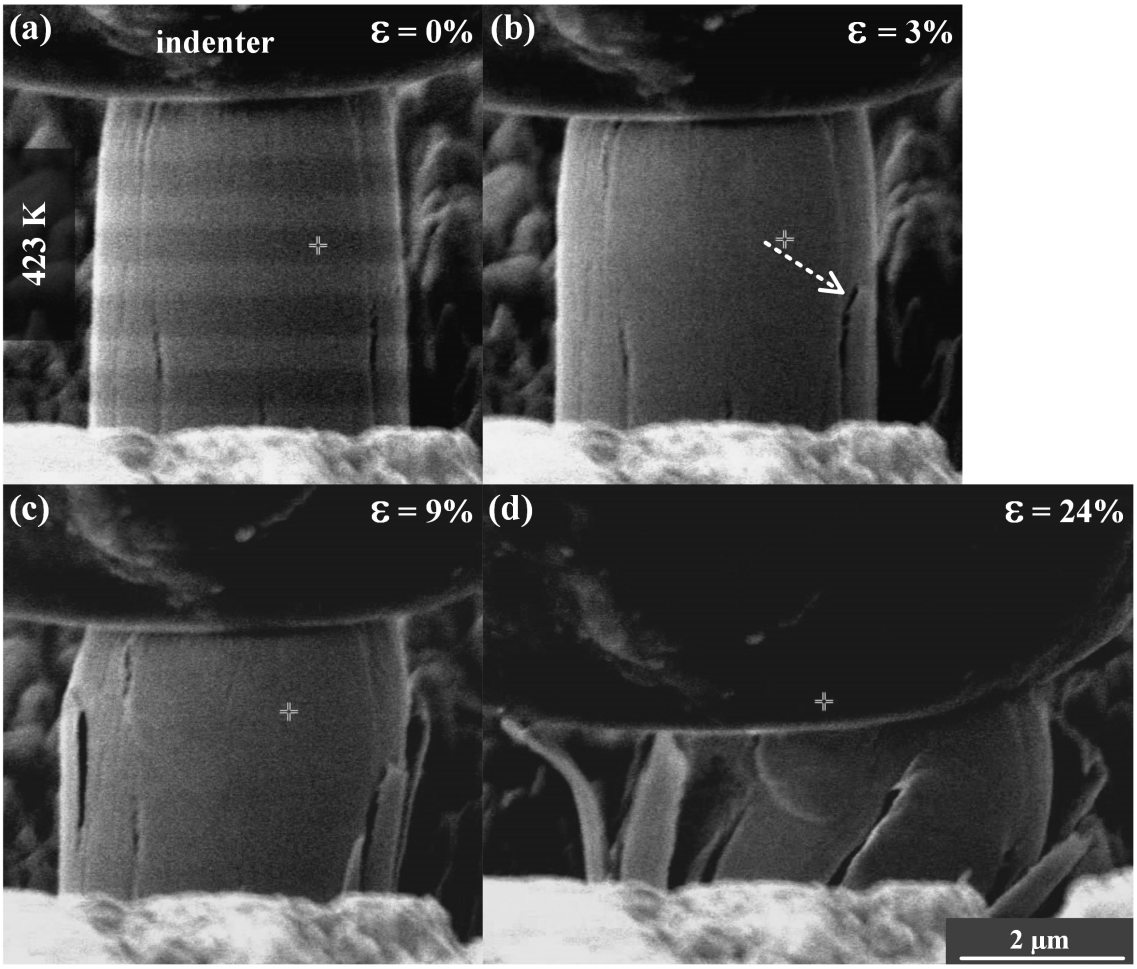

Figure 3.10: Sequential *in situ* SEM snapshots of the a micropillar which is deformed at 423K at different engineering strain levels : (a) 0%, (b) 3%, (c) 9%, and (d) 24%.

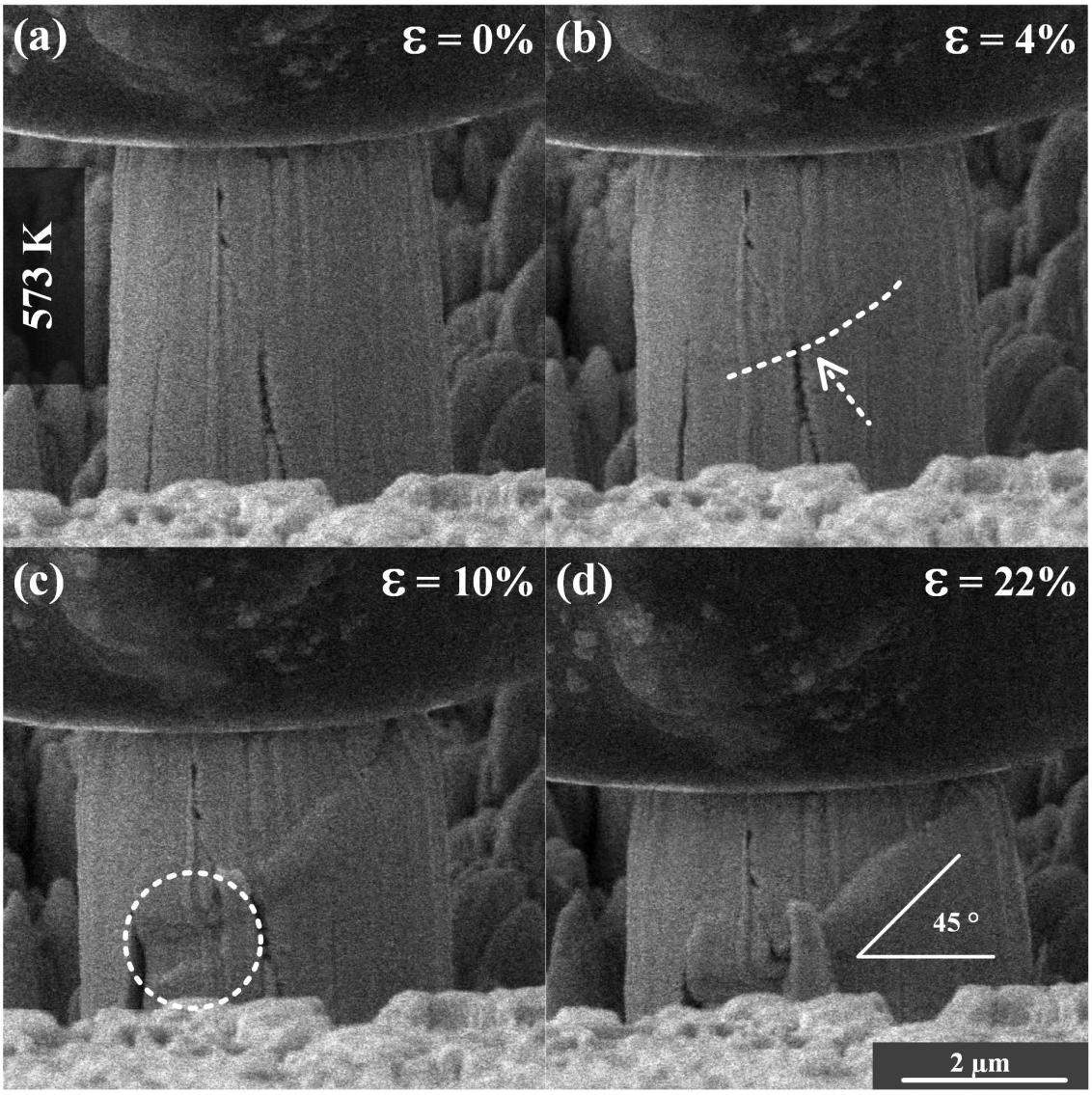

Figure 3.11: Sequential *in situ* SEM snapshots of the a micropillar which is deformed at 573K at different engineering strain levels : (a) 0%, (b) 4%, (c) 10%, and (d) 22%.

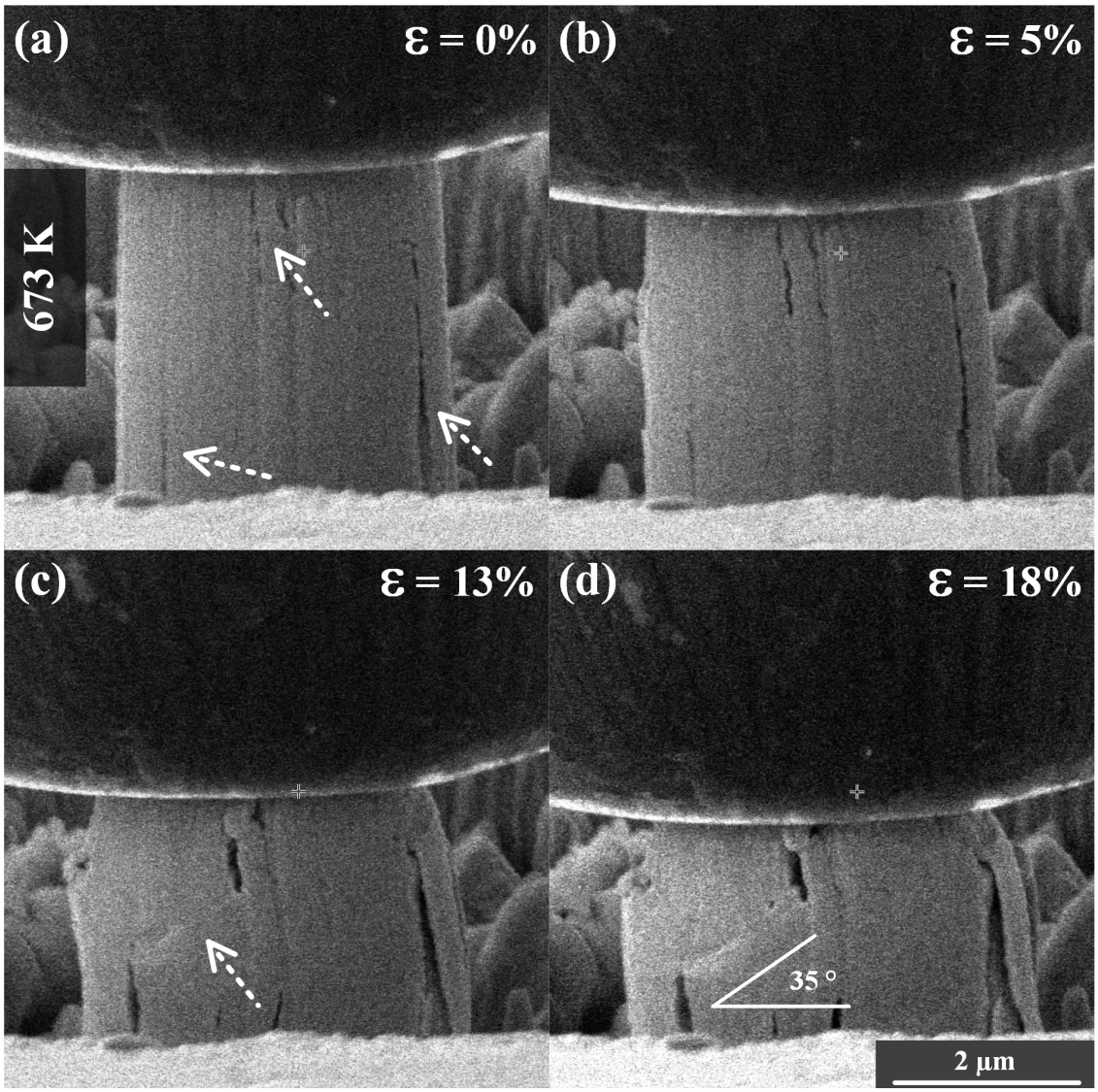

Figure 3.12: Sequential *in situ* SEM snapshots of the a micropillar which is deformed at 673K at different engineering strain levels : (a) 0%, (b) 5%, (c) 13%, and (d) 18%.

At higher temperatures (i.e., T >423 K), the microspecimens demonstrate a significant improvement in defect tolerance due to enhanced plasticity, and thus, maintains excellent structural integrity up to at least 20% strain. At 573 K, the apparent pre-existing voids on the surface do not lead to local fracture or delamination upon loading (see for example Figure 3.11). Instead, a shear band initiates at one of the GB defects and develops in the adjoining surface grains, as indicated by the dashed line in Figure 3.12 at 4% strain. The shear band steadily grows with further deformation, which leads to blunting of the tip of the GB defect but with no catastrophic failure. The observed shear band is approximately 45° with respect to the pillar axis, which coincides with the maximum shear stress direction. At 673 K, the sample deforms even more uniformly as shown in Figure 3.12. In this case, the microspecimen is observed to deform in a barrel-like shape, with shear bands initiating at pre-existing GB defects. Further SEM investigations (see for example Figure 3.13) show that plasticity initiates at the tip of the pre-existing voids/pores. It should be noted that the observed uniform wavy slip is distinct from the localized sharp slip in face-centered-cubic (FCC) microcrystals, and is typically observed in BCC bulk crystal [116] and W microcrystals below T_c [4, 19]. Furthermore, the pre-existing defects at GBs are observed to open progressively along the horizontal direction to accommodate the barrelled deformation, however, their tips are mostly blunted due to the enhanced plasticity at elevated temperatures, which also lead to the formation of shear bands. Accordingly, none of the surface GB defects are able to propagate vertically along the

GBs, which suppresses any catastrophic failure up to at least 20% strain.

3.2.2 Micro-mechanical Model for Predicting the Flow Strength of BCC Microcrystals

To predict the compressive strength of micropillars as well as the the individual curds of the micro-architectured coatings, a dislocation-density based model is proposed here, which accounts for the effect of crystal or grain size, D, dislocation density, ρ, strain rate, $\dot{\varepsilon}$, and temperature T. In this model, the flow strength, $\sigma_f(T, \dot{\varepsilon}, D, \rho)$ is decomposed into two components:

$$\sigma_f(T, \dot{\varepsilon}, D, \rho) = M\tau_f(T, \dot{\varepsilon}, D, \rho) = M(\tau_0(T, \dot{\varepsilon}) + \tau_{athermal}(D, \rho)) \tag{3.2.1}$$

where M is the Taylor factor for polycrystals or the inverse of Schmid factor of single crystals, τ_f is the resolved flow strength which is comprised of lattice friction,τ_0, and athermal contribution $\tau_{athermal}$. For $\tau_{athermal}(D, \rho)$, which arises from the long-range elastic interactions of dislocations, the parameter is represented using the generalized size-dependent Taylor-strengthening law [83], viz.

$$\tau_{athermal} = \mu(\frac{\beta}{D\sqrt{\rho}}) + \alpha\mu b\sqrt{\rho} \tag{3.2.2}$$

where $\beta = 1.76 \times 10^{-3}$ and $\alpha = 0.57$ are dimensionless constants which were determined in [83] using experimental data and 3D discrete dislocation dynamics (DDD) simulations, b is the magnitude of the Burgers vector, and $\mu(T)$ is the shear modulus,

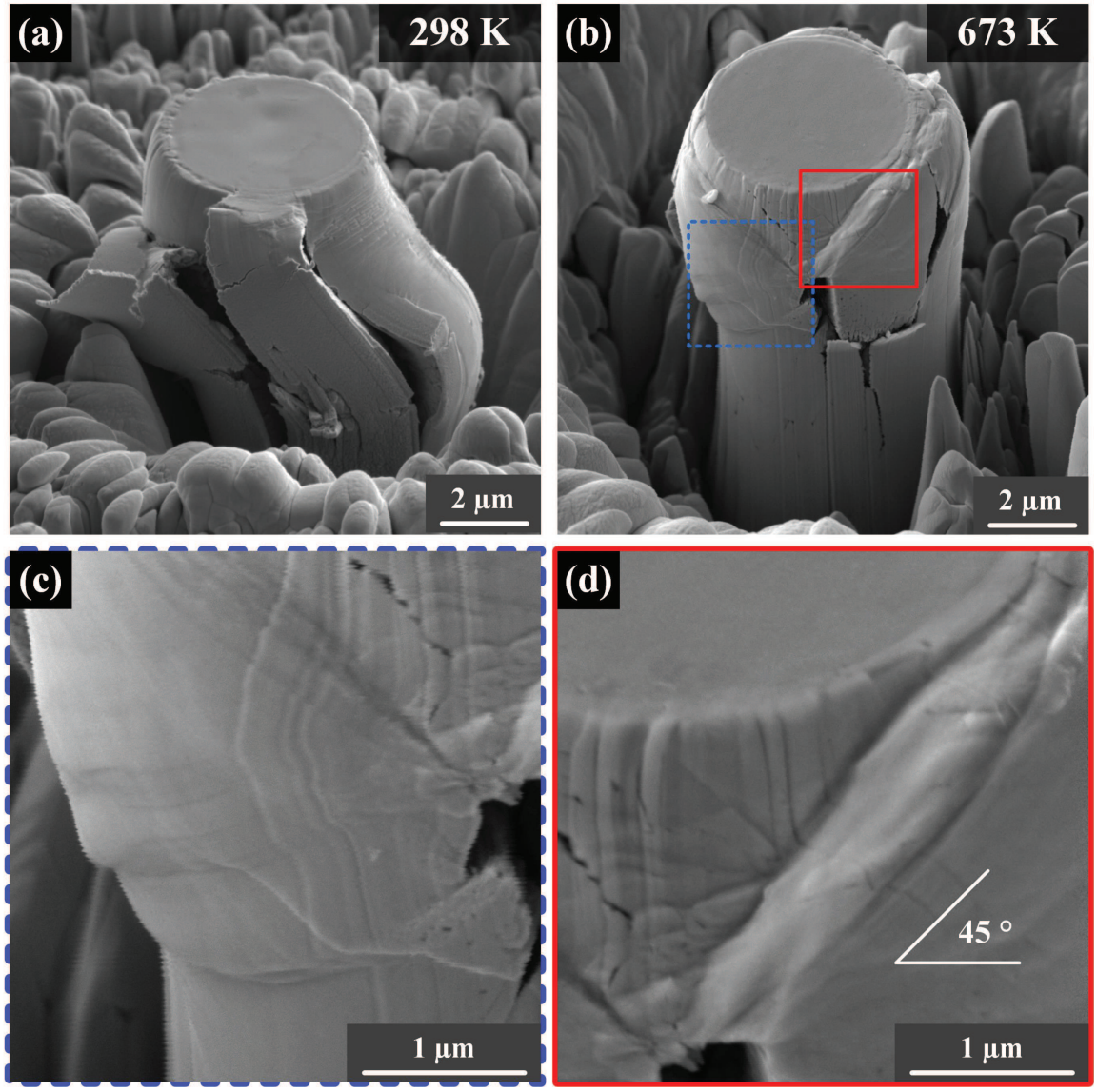

Figure 3.13: SEM micrographs of 5 µm micro-architectured tungsten micro-pillars after testing at: (a) room temperature; and (b) 673 K. Zoom-ins of the two boxes in (b) are shown in (c) (d). (c) shows wavy slip traces which are observed in BCC microcrystals, comparing with (a), it indicates surplus amount of plasticity at 673 K. The localized shear band in (d) is 45° with respect to loading axis which coincide with max shear stress direction.

which is weakly dependent on temperature. In this equation, the first term represents the strength of the weakest dislocation source, and the strength contribution from dislocation forest hardening is accounted by the second term [83].

In single crystal microspecimens where dislocations can escape from the free surface, it was previously shown that the initial dislocation density, ρ_0, can be used in Equation 3.2.2. However, for polycrystalline microspecimens the effect of GBs impeding dislocation slip must be accounted for. It was shown that in UFG bulk polycrystals, dislocation density as a function of strain level and grain could be represented as [117, 118]:

$$\rho = \rho_0 + \frac{A\varepsilon}{bD} \tag{3.2.3}$$

where A is a constant. Considering the sample is CVD-grown then heat treated, the dislocation density is assumed to be on the order of $\rho_0 = 10^{12}$ m^{-2}. For bulk polycrystalline FCC materials, A was measured to be ~3.58 [119], however, for polycrystalline microcrystals it can be expected that the dislocation density will increase with increasing strain at a lower rate (i.e., smaller A is expected). Nevertheless, there are no estimates in literature on the appropriate values for A that can be directly used in current study. For polycrystals having a grain size on the order of 1 µm and an initial dislocation density $\rho_0 \leq 10^{12}$ m^{-2}, the term $A\varepsilon/bD$ in Equation 3.2.3 becomes dominant. Utilizing this and combining with Equations 3.2.1 and 3.2.2, it can be shown that

$$\sigma_f = M\Big[\tau_0 + \mu\Big(\frac{\beta}{\sqrt{A\varepsilon/b}} + \alpha b\sqrt{A\varepsilon/b}\Big)D^{-0.5}\Big] \tag{3.2.4}$$

Temperature-dependent term, τ_0, is measured from bulk single crystal experiments by Brunner [120] are used, and the discrete data points are fitted it into a polynomial form as follows:

$$\tau_0(T, \dot{\varepsilon} \sim 10^{-3}) = \begin{cases} 4.54 \times 10^{-4}T^2 - 1.223T + 708.07 & 0 < \text{T} < 626 \text{ K} \\ 5.42 \times 10^{-3}T^2 - 8.28T + 3.18 \times 10^3 & 626 \text{ K} < \text{T} \end{cases} \tag{3.2.5}$$

where temperature, T, is inKelvin, and the stress is in MPa. In addition, the dependence of shear modulus on temperature takes the form [121]

$$\mu(T) = -2.054 \times 10^{-5}T^2 - 9.1979 \times 10^{-2}T + 1629 \tag{3.2.6}$$

with T and $\mu(T)$ in unit of K and GPa, respectively, and the Burgers vector, b, is assumed to be independent of T with a value of 0.274 nm.

The resolved flow strength, τ_f, at 2.5 % strain from previously published W single crystal micro-compression experiments of micropillars having $D = 1$ and 5 µm are shown in Figure 3.14. It is commonly reported that FIB'ed microspecimens generally have a dislocation density on the order of 10^{11} to 10^{13} m^{-2} [122–124] which depends on various factors, including the processing procedure of the parent crystal, annealing conditions, etc. [125]. Glebovsky and Semenov [126] indicated the W single crystals grown using the electron-beam floating zone method have a dislocation density no less than 2×10^{10} m^{-2}. Williamson and Smallman [125] reported well annealed metals as having dislocation densities ranging from 2×10^{11} m^{-2} for aluminium to 3×10^{12}

m^{-2} for tungsten. While initial dislocation density in the single crystal experiment was not reported [4], considering that the parent single crystals are usually grow from liquid or solid state, a low level dislocation density on the order of $\sim 10^{11}$ m^{-2} could be expected. Furthermore, the heat treatment on the micropillars (inside the SEM right before testing) could potentially remove FIB-induced dislocations near the surface, and thus a dislocation density of 2×10^{11} m^{-2} would be a good approximation. Nevertheless, predictions from Equation 3.2.2 for the single crystal case with an initial dislocation density, ρ_0, of 2×10^{11} m^{-2} and 2×10^{12} m^{-2} are both shown in Figure 3.14.

The predictions with an initial dislocation density $\rho_0 = 2 \times 10^{11}$ m^{-2} shows an excellent agreement with the experimental results for both crystal sizes at all tested temperatures. The predictions with $\rho_0 = 2 \times 10^{11}$ m^{-2} gives reasonable estimation for D = 5 µm, however, significantly underestimates the resolved flow stress for the case of D = 5 µm. This observation is rationalized by Equation 3.2.2 by considering that for crystals which that are small enough and have a low dislocation density (i.e., $D \times \sqrt{\rho}$ is small) the first term dominates the CRSS, however, when crystals are large enough and have a moderate dislocation density, the CRSS is then dictated by the second term. For the 5 µm case, the response is dominated by forest hardening for both dislocation density; however, for 1 µm case, an order of magnitude increase in dislocation density leads to the transition from dislocation-source controlled to forest-dominated hardening.

The predictions from Equations 3.2.4 and are shown in Figure 3.15 for the poly-

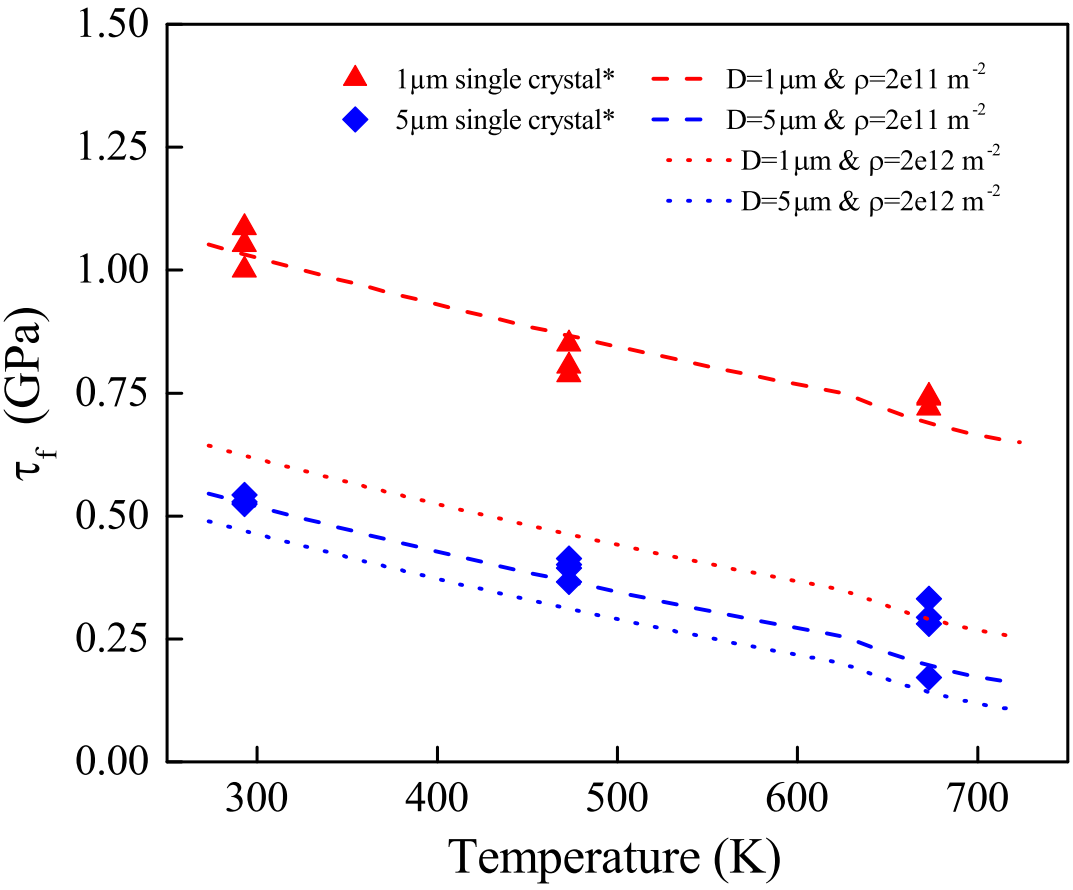

Figure 3.14: The resolved flow strength, τ_f, as measured from 1 µm and 5 µm single crystal W microcrystals [4], as well as those predicted from Equation 3.2.1 for two initial dislocation densities.

crystalline microspecimens in this study. Electron backscattering diffraction (EBSD) analysis of the current coating indicates that Taylor factor for this coating is $M \sim 2.25$. It is shown that the prediction with $A = 3.58$ give a dislocation density $\rho = 3.27 \times 10^{14}$ which over estimates the experimental results. On the other hand, by setting $A = 1.432$, a dislocation density $\rho = 1.3 \times 10^{14}$ is yielded, and it is clear that Equations 3.2.4 are in excellent agreement with the experimental results. This lower value of A indicates that the dislocation density evolves with a lower rate than in bulk polycrystals.

3.3 Micro-tensile Test at Room Temperature

The micro-compression technique has been widely used to study the micro and nano mechanics of materials. Beyond the scientific breakthrough it brought, its success is largely attributed to the simplicity of specimen fabrication and experimentation. However, there are some limitations of such experiments. One drawback is that the stress state during the deformation is never maintained to be uniaxial, which is partially attributed to the limited aspect ratio of micropillars and the specimen boundary conditions. From the material perspective, compression experiments are not suitable for quantifying ductility or maximum elongation as typically metals can sustain large amount of compressive strains before failure, including many brittle materials. In addition, some materials exhibit tension compression asymmetry. This motivates the development of small scale micro-tensile testing.

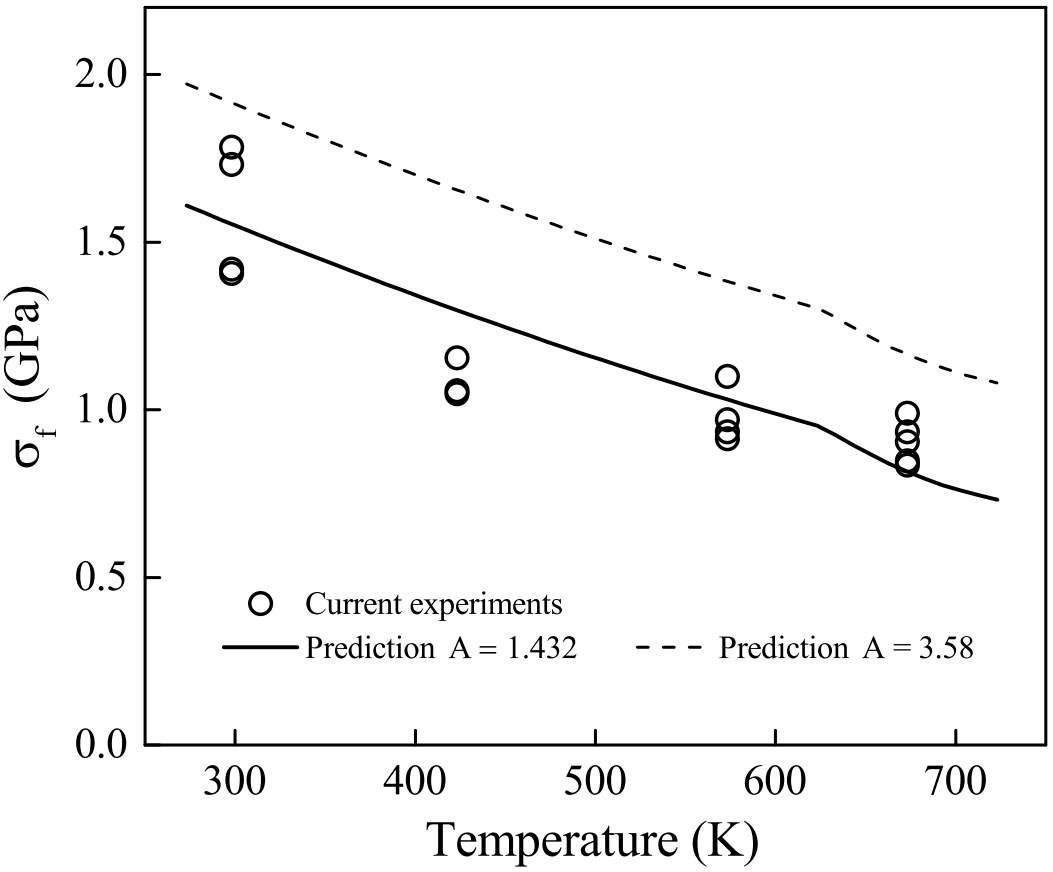

Figure 3.15: The flow stress at 2.5% strain from the current experiments as a function of temperature as well as the predictions from Equation 3.2.4 for A = 1.432 and 3.58.

CHAPTER 3. MICRO-MECHANICAL CHARACTERIZATION: FROM AMBIENT TO ELEVATED TEMPERATURE

In this section, the micro-tensile apparatus described in Chapter 2 is used to study the mechanical response of a micro-specimen milled from the micro-architectured W-coating. The motivation of this work is twofold: first, to examine the small-scale tensile methodology developed in this thesis work; and second, to quantify the tensile strength and failure mode of microcrystals milled from the micro-architectured W coatings.

The micro-tensile experiment is conducted using a load control method to maintain the sample is strained at a engineering strain rate on the order of 10^{-3}. The tensile specimen has a gauge length of 42 µm, width of 10.3 µm, and thickness of 5.8 µm, and is fabricated along the grow direction of the coating (i.e., through thickness). The sample and gripper fabrication is detailed in Chapter 2.

The engineering strees-strain along with the SEM snapshots at different strain levels are shown in Figure 3.16. The specimen failed at a maximum tensile stress of ∼1050 MPa. During the deformation, it exhibited little hardening and is followed by a large strain burst as manifested in the stress-strain curve. It is worthwhile to mention that the data collection frequency is 500 Hz and there is no data points recorded beyond 11 % engineering strain up to above 25% engineering strain which indicates that the failure was catastrophic. A linear fit on elastic regime give a Young's modulus of $\sim$ 30 GPa, which is only a small fracture of theoretical value (400 GPa). This is mainly due to the compliance form the SiC and W gripper and sample base, which suggests further characterization of system compliance may be required.

Nevertheless, the maximum tensile stress of $\sim$ 1050 MPa should be unaffected. To eliminate the toe region (i.e. before (2)), which is related to the sample head securing inside the gripper, foot compensation is performed based on ASTM standard and is shown as dashed line. By comparing the SEM micrographs at different strains (i.e., (1), (2), and (3) in Figure 3.16(b)), the it is difficult to find any discernible signs of plastic deformation or crack nucleation, which confirms our hypothesis based on the stress-strain curve that the failure is abrupt and brittle.

To further characterize the failure, fracture surface morphology is examined using secondary electron (SE) SEM and FIB ion channeling contrast images before deformation as shown in Figure 3.17. It is observed that the crack occurred at the second layer of the coating. Comparing the sample before and after deformation (i.e., Figure 3.17(a) and (c)), we observed that the fracture path coincides with the regions (arrowed in (a)) that have a high density of pre-existing voids. For those large pre-existing defects, they are precisely located on the crack path (see the blue circled region in Figure 3.17(a) and (c)), which suggests the failure process is sensitive to these defects. In addition, the fracture surface/path profile is highlighted with a dashed line in Figure 3.17(c) and superimposed onto the FIB ion channeling contrast image before deformation (see Figure 3.17(d)), through this comparison, it is clear that cracks initiation and propagation may not necessarily occur exclusively at the grain boundaries. Zoom-ins of rectangular regions in Figure 3.17(c) are shown in Figures 3.17(e) and (f), which also indicate co-existing of inter- and transgranular type of

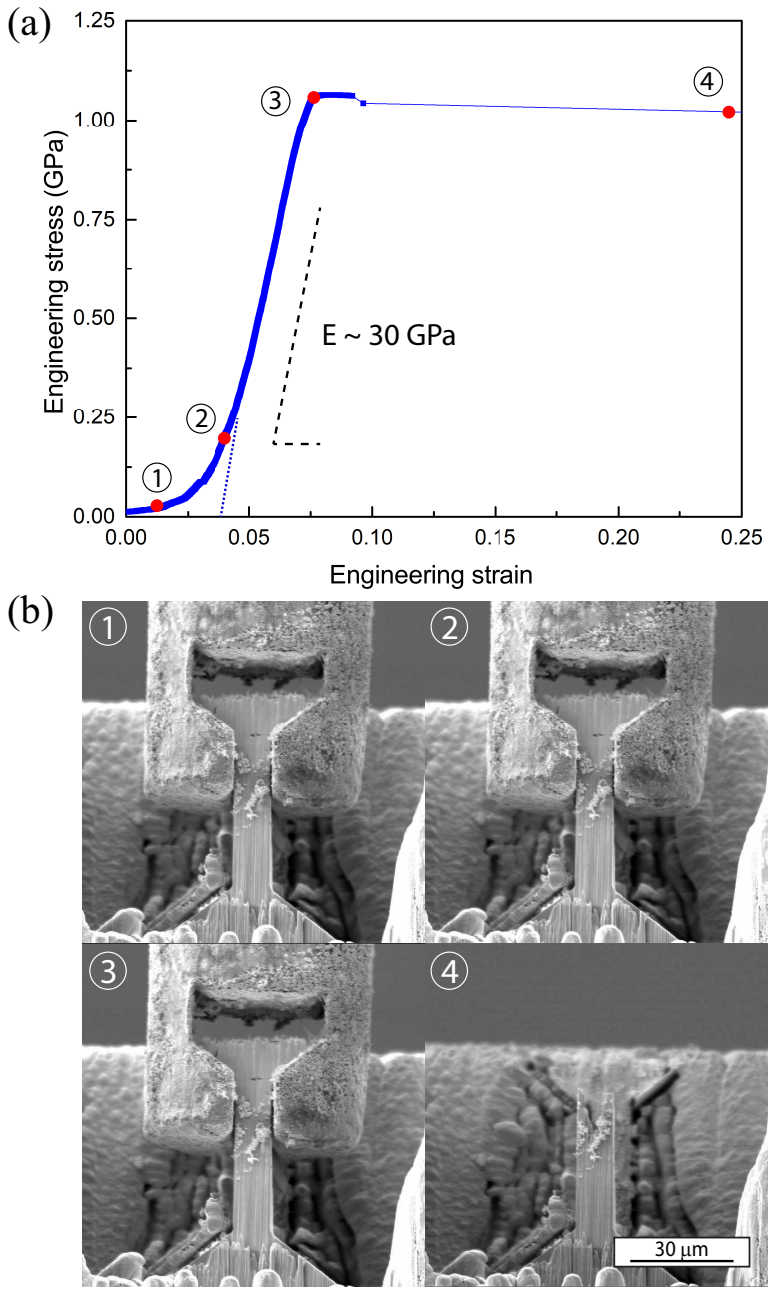

Figure 3.16: (a) The engineering stress-strain curve from *in situ* microtension experiments for a tensile specimen having a width of 10.3 µm, a thickness of 5.8 µm and a gauge length of 42 µm, the dash line intercepts with the x-axis indicates foot correction. (b) Sequential *in situ* SEM snapshots of the deformation morphology at different strains. The circled numbers in (a) and (b) give the strain level at which the corresponding SEM micrograph was taken.

fracture process during the failure. The cleavage surface in Figure 3.17(e) has sharp edges, which is a sign of transgraunular failure, whereas Figure 3.17(f) shows smooth surface and elongated dimples that are parallel to the growing direction, which indicates voids were formed at the surface during CVD process and led to fracture at the grain boundaries. The above conclusion is also supported by SEM micrographs taken from the sample top and are shown in Figure 3.18. Thus, based on above analysis, it is suggested that fracture may initiate at pre-existing voids and propagate along the brittle grain boundary and then deviate into grains, which results in both inter- and transgranular type of fracture under tensile loading.

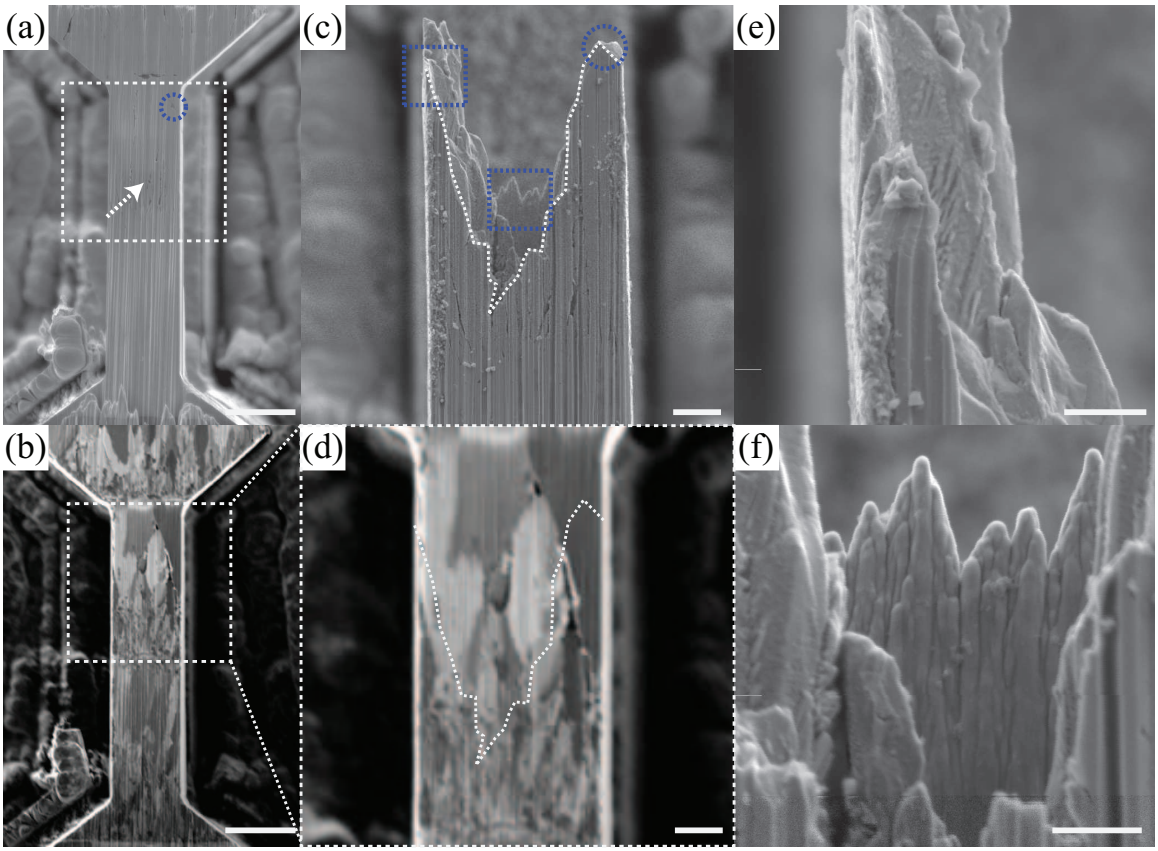

Figure 3.17: SEM secondary electron and FIB channelings contrast micrographs of specimen before and after failure from sample side: (a) SEM and (b) ion channeling contrast imaging of the specimen, and the failure region is highlighted with a dashed line rectangle with zoom-ins that are shown in (c) and (d); fracture profile in (c) is recorded using dashed line and superimposed on the ion channeling contrast image (d) for fracture analysis; (e) and (f) are close views of the highlighted region (blue rectangle) in (c). Circled region in (a) and (c) are the same region before and after deformation. It is shown that fracture occurs at the location that coincides with a region that has a high density of pre-existing cracks region indicated with an arrow in (a). The scale bars are 10 µm for (a)-(b), 2.5 µm for (c)-(d), and 1 µm for (e) and (f).

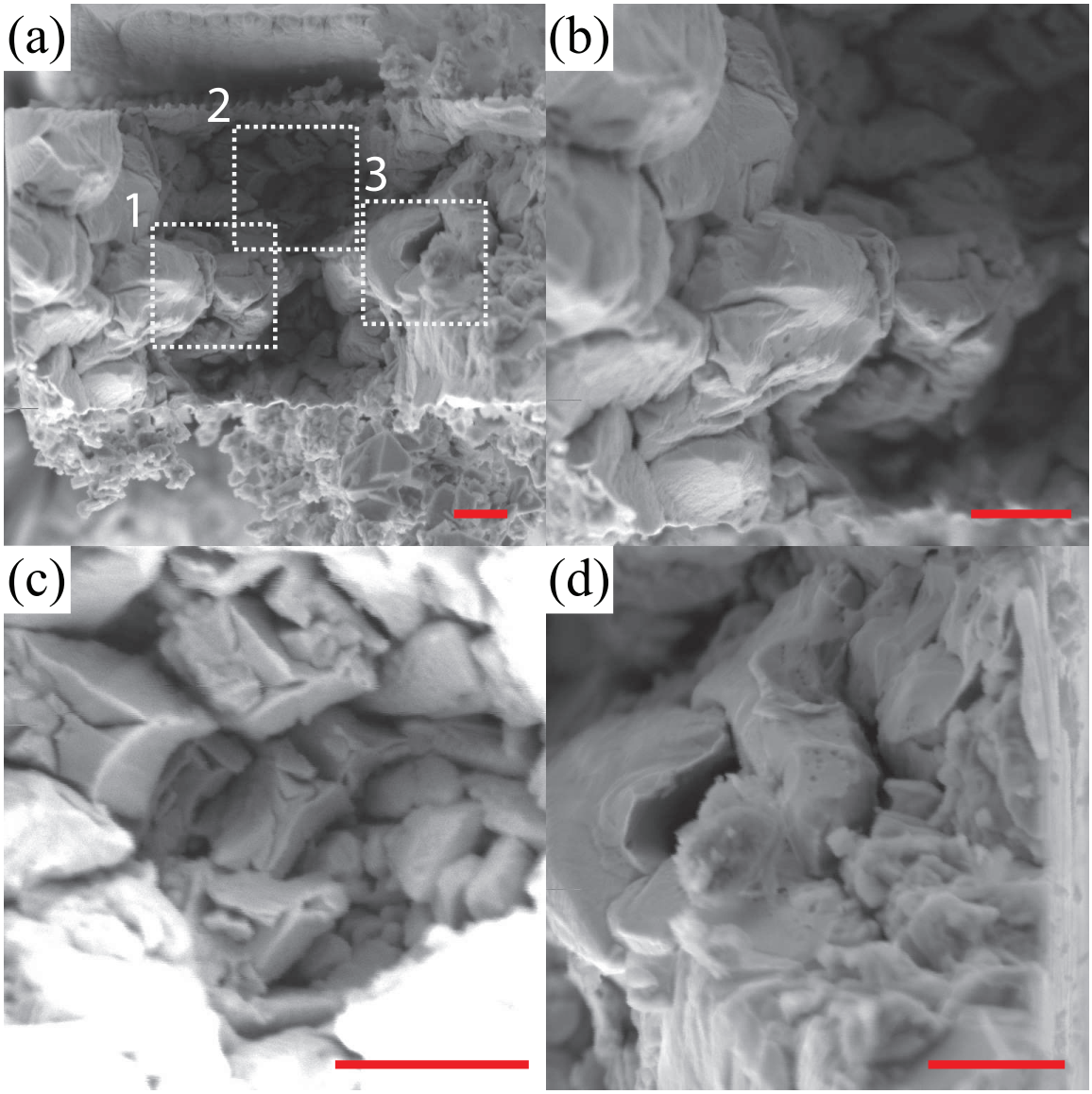

Figure 3.18: Fracture surfaces of the tensile specimen observed from the sample top: local regions 1-3 in (a) are shown with higher magnification in (c-d) respectively. All figures share the same scale bar of 1 µm.

3.4 Micro-cantilever Deflection Experiments at Room Temperature

Micro-cantilever deflection experiments are widely utilized to measure elastic properties and fracture toughness in both bulk samples and thin films. Weihs et al. [127] first proposed and utilized this techniques to determine the elastic moduli and yield strength of thin-film materials. Armstrong et al. [128] fabricated triangular cross-sectioned micro-cantilevers using FIB on bulk polycrystalline copper sample and quantified the anisotropy of the elastic modulus. This idea was then further developed to measure fracture toughness of the coating and has been shown it is more flexible and versatile compares to bulk scale experiments. Di Maio and Roberts [54] introduced the idea of fabricating pre-cracked cantilever microbeam using FIB and fracture them using a nanoindenter to determine the fracture toughness. This experimental technique has then been used to measure the fracture toughness of silicon based passivation film [55], NiAl single crystalline along different orientations [129], tungsten [130] and many other materials.

In this section, we utilize this methodology on unnotched beams fabricated from the micro-architectured W coatings to determine the grain boundary fracture stress. All experiments were carried out inside an SEM with a Berkovich tip to apply a point load on the free ends of the micro-beams, as shown in figure 3.19 (a). For the purpose

of monitoring the crack initiation and propagation, the side wall of the fixed-end side of cantilever is clean using FIB as shown in Figure 3.19 (b).

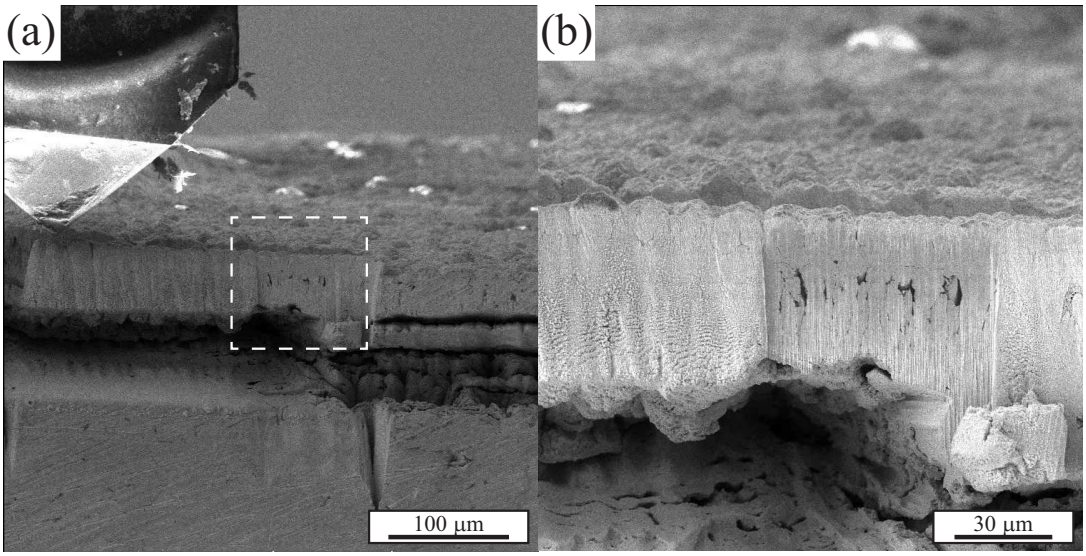

Figure 3.19: SEM micrographs of the micro-cantilever deflection experiments: (a) Experimental setup, where a Berkovich tip applies point load at the free end of microbeam. (b) Zoom-in of the dash-lined region in (a) to show the fixed end of cantilever, which was cleaned using FIB before experiment to reveal the pre-existing defects.

The in-plane stress during the deflection is estimated using Euler beam theory. For a point load with magnitude F is applied on the free end of the beam (schematically shown in Figure 3.20), the governing equation and associated boundary condition are

$$EI\frac{\mathrm{d}^4 w}{\mathrm{d}x^4} = F\delta(x-L) \tag{3.4.1}$$

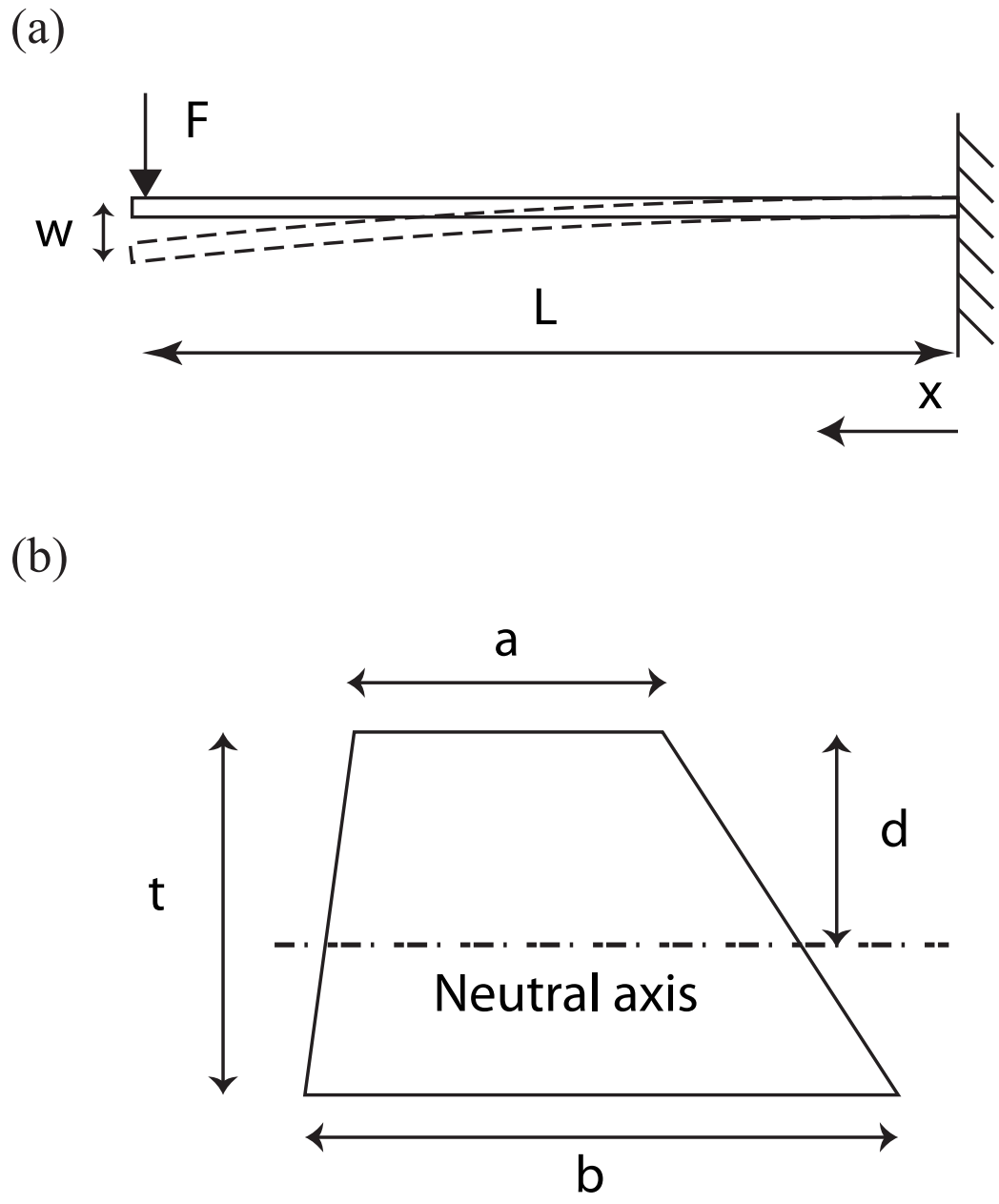

Figure 3.20: Schematic of (a) the experimental setup and (b) cross-sectional plane of microbeams. As the beam has a trapezoidal cross section, the neutral axis does not coincide with the center line, and its distance to top surface is denoted as d.

with

$$w|_{x=0} = 0, \quad \left.\frac{\mathrm{d}w}{\mathrm{d}x}\right|_{x=0} = 0, \quad \left.\frac{\mathrm{d}^2w}{\mathrm{d}x^2}\right|_{x=L} = 0 \tag{3.4.2}$$

where w is deflection, E is Young's modulus, I is the second moment of area of the cross-sectional plane, which can be calculated follows

$$I = \frac{t^3(a^2 + 4ab + b^2)}{36(a+b)} \tag{3.4.3}$$

with the neutral axis location from top surface

$$d = \frac{t(a+2b)}{3(a+b)} \tag{3.4.4}$$

where a, b are the top and bottom edge length, and t is the height as indicated in Figure 3.20 (b). The tensile stress experienced by the beam above the neutral axis is

$$\sigma = \frac{Mz}{I} \tag{3.4.5}$$

where z is the distance from the neutral axis to the point of interest, and M is the bending moment. Using the above equation, the maximum tensile stress that occurs at the top surface can be calculated by setting $z = d$.

Three free standing micro-architectured W coating micro-beams were tested at a constant loading rate, and a representative displacement versus load curve is shown in Figure 3.21. The calculated maximum tensile stress along with geometric measurements for tested micro-beams are summarized in Table 3.1. The maximum load achieved in the experiment , which is termed as fracture load in Table 3.1, is used to calculate the maximum tensile stress. This will be used to identify the grain boundary cohesive strength in cohesive zone model (CZM) in Chapter 4. The displacement

Table 3.1: Summary of maximum tensile stress (at the top surface of the point at which fracture initiates along the micro-cantilever length) calculated using Equation 3.4.5 along with the cross-sectional dimensions and experimentally measured fracture load of each tested micro-beam. The cross-sectional dimension parameters are defined in Figure 3.20(b).

Beam #	a (µm)	b (µm)	t (µm)	d (µm)	Fracture load (mN)	Max tensile stress (MPa)
B1	44	76	54	29.4	17.67	139.2
B2	44	60	35	18.4	7.96	161.2
B3	44	74	50	27.1	32.35	296.1

burst in Figure 3.21 indicates the failure is catastrophic and brittle. It should be mentioned that here although the experiment is load-controlled, a linear drop on load is observed when the displacement burst occurs. This reduction is associated with the subtraction of the force on the spring of the indenter from the total/raw force. Finally, specimens were examined using SEM and shown in Figure 3.22. Figure3.22(b) and (c) show that the fracture coincide with the regions having cracks, and the path is superimposed onto the SEM micrograph that is taken before deformation as shown in Figure 3.22(a).

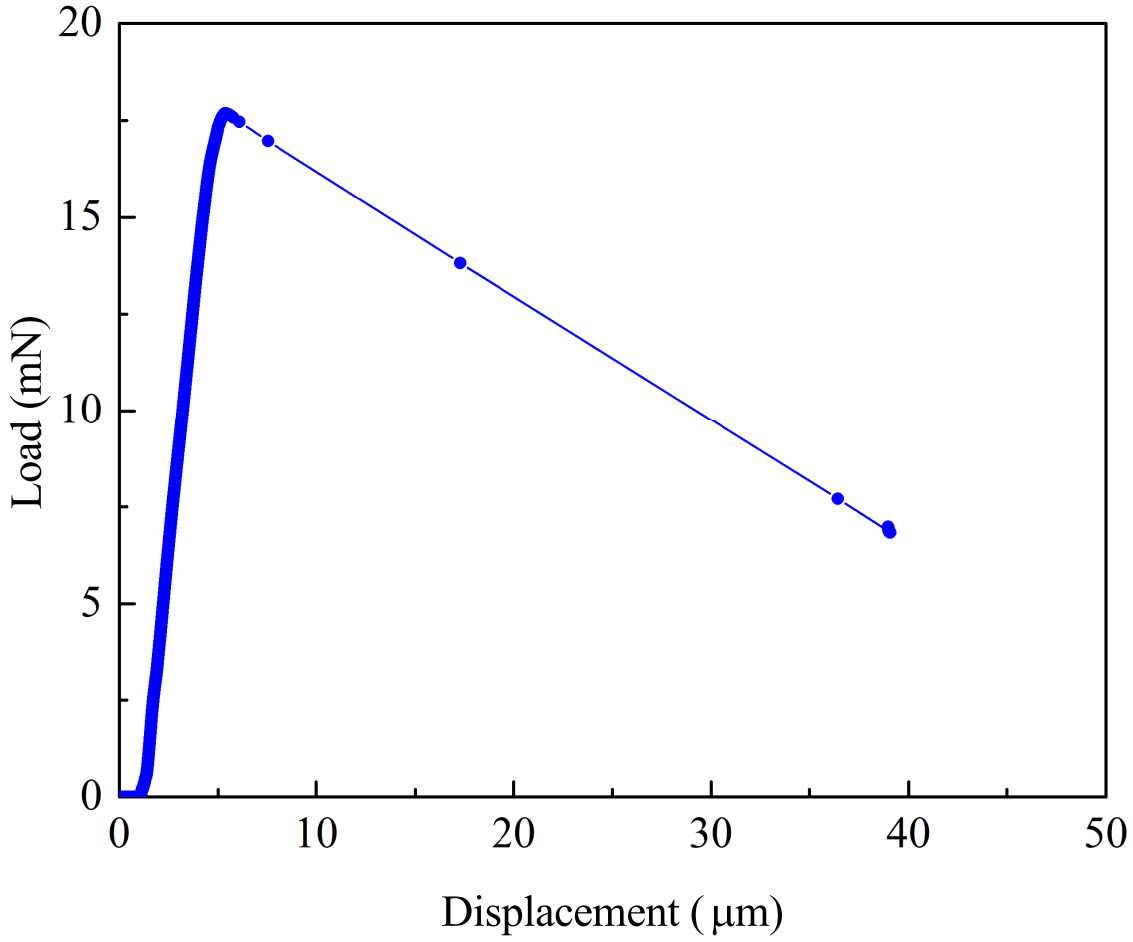

Figure 3.21: A representative displacement-load curve obtained through micro-cantilever beam deflection experiment. The experiment is load-controlled, and the load drop during the displacement burst is caused by the subtraction of force on the spring (of the indenter column) from the total force.

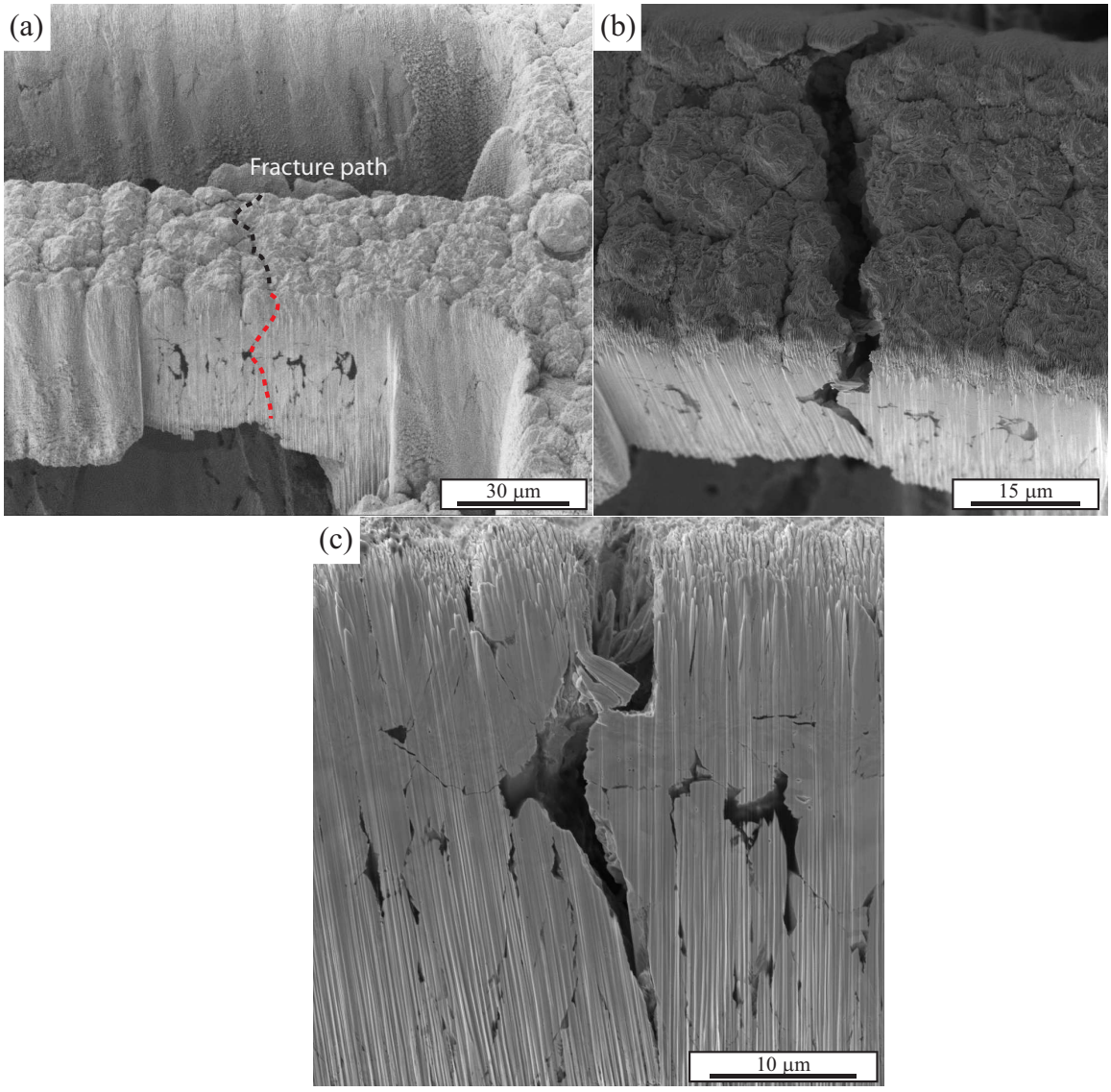

Figure 3.22: SEM micrographs of a micro-beam specimen before and after deflection. (a) Predeformed micro-beam superimposed with dashed line to indicate the crack path. SEM micrographs taken on the fractured micro-specimen to reveal the crack path from (b) top and (c) side of the micro-beam.

3.5 Summary of Micro-mechanical Experiments

In summary, *ex situ* and *in situ* SEM micro-compression/tension and micro-cantilever deflection experiments were performed to study the thermo-mechanical response and failure of microspecimens milled the micro-architectured tungsten coating. The results and analysis show:

1. The coating exhibits very high strength and brittle failure at room temperature. Our micro-tension experiments reported a maximum tensile strength ∼1.2 GPa without showing any hint of plasticity before catastrophic failure. Post-mortem examination indicates cracks preferentially nucleate near the pre-existing voids and propagation along grain boundaries and deviate into grains. In micro-compression experiments, the coating exhibits a week size-dependent strength that is above 1.5 GPa with moderate scattering. Consider intergranular fracture is predominant, grain boundary cohesive strength is probed through micro-cantilever deflection experiments. It is shown the strength is ranging from 140 MPa to 300 MPa based on the micro-specimens tested.

2. A transition in the deformation mode is identified above a characteristic temperature between 576 K and 673 K in the micro-compression experiments. At low temperatures, catastrophic failure characterized by intergranular fracture

and buckling of individual columnar grains are prevalent. This originates from the intrinsic void along the grain boundaries and the difficulties in activating plastic slip.

3. At elevated temperatures, the enhanced mobility of dislocations give rise to an enlarged plastic zone at the pre-existing GB defects. This cause the effect of the geometric defects to diminish, and thus, the material exhibits continuous plastic flow response and more homogeneous deformation.

4. While the strength of the coating will inevitably decrease with increasing temperature, the UFG microstructural design still offers a good strength at elevated temperatures. In addition, the onset of plasticity at elevated temperatures offers improved defect tolerance capabilities that suppress structural instabilities observed at low temperatures.

5. Finally, a physics-based model was proposed to predict the effect of temperature, and intrinsic/extrinsic size on the strength of this coating system, and can further be applied to other BCC materials. The model was shown to be in agreement with current experiments as well as previously published W single crystal studies.

The above highlights that the micro-architectured microstructure offers a great combination of excellent mechanical strength, and structural integrity at elevated temperatures, which is ideal for extreme environment applications.

Chapter 4

Crystal Plasticity Finite Element Modeling of the Thermo-mechanical Response of Micro-architectured Tungsten Coating

Image-based modeling and simulations are conducted to investigate the thermo-mechanical response of the polycrystalline micro-architectured W coatings and to elucidate its microstructure-property relationships. This computational framework comprises of microstructural characterization, synthetic microstructure generation, meshing and crystal plasticity based finite element (CPFEM) simulations. This chapter is organized as follows. First, the finite-deformation, rate- and temperature-dependent

crystal plasticity formulation based on the kink-pair mechanism , is summarized. The procedure for the generation and meshing of the quasi-3D statistically equivalent representative microstructure is then presented. To allow nonlinear fracture nucleation and propagation processes at the grain boundary, a traction-separation type of interface constitutive law is incorporated into the finite element framework through the embedded cohesive zone model. Using this framework, systematic investigations were carried out on the deformation and failure in micro-compression experiments at various temperatures (i.e. 293 K-673 K).

4.1 Finite-deformation Crystal Plasticity Theory

The fundamentals of single crystal plasticity were established during the early 20th century, sparked by the development of the well-known *Schmid's law*. Around same time, in an effort to predict the anisotropic deformation of polycrystalline metals, Taylor [131] and Sachs [132] proposed their own models with an isostrain or isostress assumption. Later, a more sophisticated self-consistent framework was developed by Kroner and further extended by Budiansky and Wu [133], Hill [134, 135], and Molinari et al. [136] in which both equilibrium and compatibility condition across the grain boundaries were maintained. Although they are computationally efficient, all these theories were built on certain amount of simplified assumptions without explicitly

considering the complex geometry and interactions within a polycrystalline material. During the last couple of decades, the crystal plasticity finite element method (CPFEM) was extensively developed and has became a powerful and versatile tool in examining microstructure-property relationships of crystalline materials, including, fracture, fatigue, etc.. This section reviews the theory of crystal plasticity within a finite-strain framework.

4.1.1 Kinematics of Finite Plastic Deformation

From a physical perspective, materials consist a large but finite number of atoms arranged in either a highly ordered (i.e. crystalline solids), or randomly oriented (i.e., amorphous solids) manner. However, from a macroscopic perspective, where the scale or the dimension of the materials is much larger than its atomic structures, the material can be idealized as a continuum body.

Now consider a continuum body $\mathcal{B}$ occupying a region of space Ω_0 embedded in a three-dimensional space and evolving with the time. The reference configuration is defined as the regions occupied by the continuum body $\mathcal{B}$ at a fixed reference time t_0; while the configuration at time $t_0 + \Delta t$ is to referred as the current configuration. As shown in Figure 4.1, the position of any material point P belongs to $\mathcal{B}$ in the reference and current configurations are given by their position vector $\mathbf{X}$ and $\mathbf{x}$. By introducing the displacement vectors $\mathbf{u}$, the particle motion can be described as:

$$\mathbf{x} = \mathbf{X} + \mathbf{u} \tag{4.1.1}$$

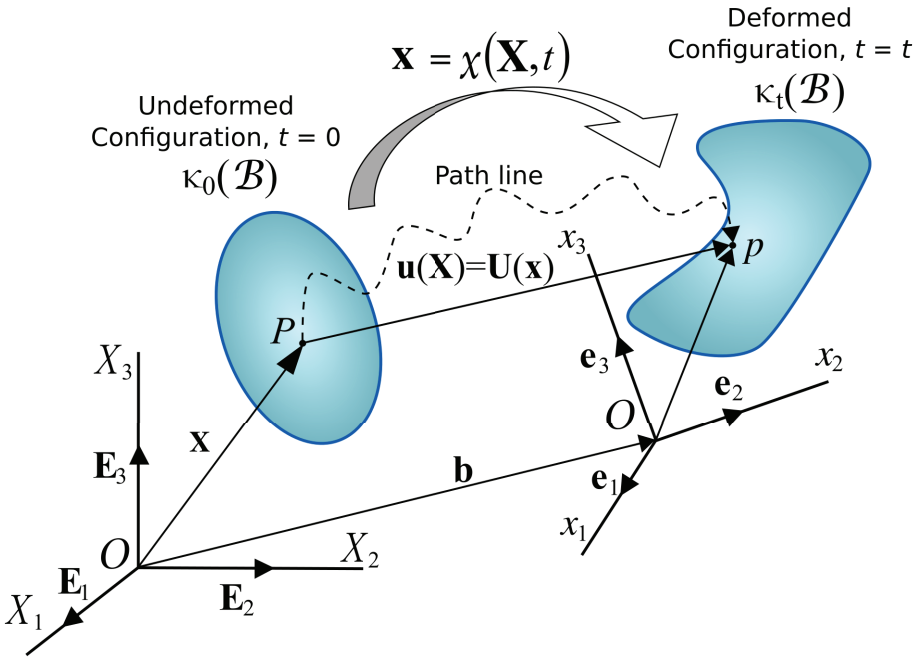

Figure 4.1: Schematic of the configuration space and motion of a continuum body. Image is adopted from Wikipedia *https://en.wikipedia.org/wiki/Conti nuum_ mechanics*

The mapping from the reference configuration to the current configuration at time t is thus written as:

$$\mathbf{x}(t) = \chi(\mathbf{X}, t) \tag{4.1.2}$$

To establish the deformation of a line element $d\mathbf{X}$ emanating from position $\mathbf{X}$ in the reference configuration to $d\mathbf{x}$ in the current configuration, the deformation gradient tensor, $\mathbf{F}$, is defined as:

$$d\mathbf{x} = \mathbf{F} \cdot d\mathbf{X} \tag{4.1.3}$$

where

$$\mathbf{F} = \frac{\partial \chi(\mathbf{X}, t)}{\partial \mathbf{X}} = \frac{\partial \mathbf{x}}{\partial \mathbf{X}} \tag{4.1.4}$$

Using Equation 4.1.1, the deformation gradient can be expressed in terms of displacement field:

$$\mathbf{F} = \mathbf{I} + \nabla_{\mathbf{x}}\mathbf{u} \tag{4.1.5}$$

where $\mathbf{I}$ is the second order identity tensor.

For crystalline matter under finite deformation, the total deformation gradient is multiplicatively decomposed into elastic and plastic parts [137]:

$$\mathbf{F} = \mathbf{F}^e\mathbf{F}^p \tag{4.1.6}$$

where the elastic component $\mathbf{F}^e$ characterizes the elastic stretching and rotation of lattice, and $\mathbf{F}^p$accounts for the isochoric plastic deformation, (i.e., det $\mathbf{F}^p = 1$). In this decomposition, a fictitious intermediate state is introduced between the reference and current configurations in which each material point is stress-free as shown in Figure 4.2. It should be noted that the intermediate configuration is not uniquely defined since a rigid body rotation could be imposed without disturbing the unstressed state. To enforce uniqueness, the elastic deformation gradient tensor $\mathbf{F}^e$ must be symmetric.

As the crystal deforms, the lattice stretches and rotates. The slip direction vector $\mathbf{m}_0^\alpha$ and slip plane normal vector of slip system α in the current configuration are given by

$$\mathbf{m}^\alpha = \mathbf{F}^e \cdot \mathbf{m}_0^\alpha \quad \text{and} \quad \mathbf{n}^\alpha = \mathbf{n}_0^\alpha \cdot \mathbf{F}^{e-1} \tag{4.1.7}$$

where $\mathbf{m}_0^\alpha$ and $\mathbf{n}_0^\alpha$ are unit vectors defined in the reference configuration. While the vectors $\mathbf{m}^\alpha$ and $\mathbf{n}^\alpha$ in the deformed configuration are not necessarily unit vectors, they must remain orthogonal.

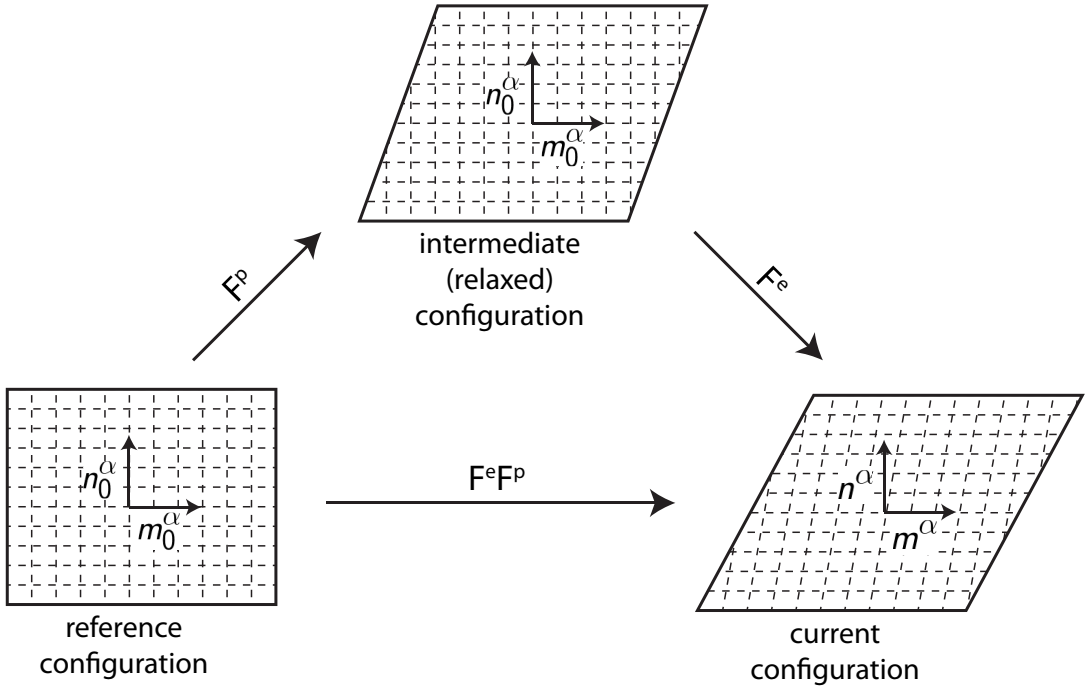

Figure 4.2: Multiplicative decomposition of the total deformation gradient **F** into elastic and plastic parts.

4.1.2 Single Crystal Constitutive model and Flow Rule

The constitutive relationship given in the intermediate configuration is in terms of the second Piola-Kirchoff stress tensor, **S**, and Lagrange-Green strain tensor, $\mathbf{E}^e$, according to

$$\mathbf{S} = \mathbb{C} : \mathbf{E}^e \tag{4.1.8}$$

with

$$\mathbf{E}^e = \frac{1}{2}\Big\{\mathbf{F}^{eT}\mathbf{F}^e - \mathbf{I}\Big\} \tag{4.1.9}$$

where $\mathbb{C}$ is the the fourth order anisotropic elasticity tensor. The Cauchy stress tensor σ defined in the current configuration is related to the second Piola-Kirchoff stress tensor by

$$\sigma = \frac{1}{\det\ \mathbf{F}^e}\mathbf{F}^e\mathbf{S}\mathbf{F}^{eT} \tag{4.1.10}$$

For dislocation-mediated plasticity, the flow rule, which defines the plastic deformation evolution, is given in terms of the plastic velocity gradient $\mathbf{L}^p$ as [138]:

$$\mathbf{L}^p = \dot{\mathbf{F}}^p\mathbf{F}^{p-1} = \sum_{\alpha=1}^{n_{slip}} \dot{\gamma}^\alpha \mathbf{S}_0^\alpha \tag{4.1.11}$$

where $\dot{\gamma}^\alpha$ denotes plastic slip rate on slip system α. $\mathbf{S}_0^\alpha$ is called the *Schmid tenosr* of slip system α given the dyadic product of slip system direction and normal, such that

$$\mathbf{S}_0^\alpha = \mathbf{m}_0^\alpha \otimes \mathbf{n}_0^\alpha \tag{4.1.12}$$

Slip rate, $\dot{\gamma}^\alpha$, is commonly formulated as a function of the resolved shear stress, and following the work by Hutchinson [139], Pan and Rice [140] and Peirce et al. [141] a power law form expression is used here:

$$\dot{\gamma}^\alpha = \dot{\gamma}_0^\alpha \left|\frac{\tau^\alpha}{s^\alpha}\right|^{\frac{1}{m}} sign(\tau^\alpha) \tag{4.1.13}$$

where $\dot{\gamma}_0$, m are material properties (i.e., reference slip rate and strain rate sensitivity) and are determined from experiments. This formulation was originally developed for

face-centered cubic (FCC) materials, and also has been shown to work in its original form or variational form for body-centered cubic (BCC) materials by incorporating the contribution of short range thermally-activated obstacles [142]. Finally, the resolved shear stress on slip system α is derived as:

$$\tau^{\alpha} = (\mathbf{F}^{eT}\mathbf{F}^{e}\mathbf{S}) : \mathbf{S}_0^{\alpha} \tag{4.1.14}$$

4.1.3 Slip System Resistance Evolution

In dislocation mediated plasticity, the dislocation density is the most important internal parameters for describing the state of plastic deformation. Here a dislocation density-based slip resistance evolution model is presented, which has been previously used to successfully predict the mechanical response of a wide range of FCC and BCC materials including Cu, W, etc.. [1, 143].

The overall shear resistance on slip system α is the summation of the thermal and athermal components (including grain boundary and Taylor strengthening mechanisms in this work):

$$s^{\alpha}(T, \dot{\gamma}) = \tau^{*}(T, \dot{\gamma}) + \tau_{GB}(T) + \tau_{dis}(T) \tag{4.1.15}$$

where τ^{*} is the stress component associated with thermally-activated process, more specifically, the Peierls/lattice resistance, while τ_{GB} together with τ_{dis} represents the atherml contribution. It should be noted that τ_{GB} and τ_{dis} originate from athermal processes but they are weakly temperature-dependent and should be considered if

simulations are conducted at a wide range of temperatures.

Grain boundaries in polycrystalline materials serves as barriers to block intergranualar dislocation transfer down to a grain sizes of ∼10 nm [144]. The classical Hall-Petch relationship [145, 146] is used here to account for such an effect

$$\tau_{GB}(T) = k_{HP}(T)\frac{1}{\sqrt{D}} \tag{4.1.16}$$

where D is the grain size, and k_{HP} is Hall-Petch strengthening coefficient, which is commonly fitted from experimental measurements of the flow strength with different average grain sizes.

In addition to the pile up of dislocations at grain boundaries, the long range interaction inside grains, namely the dislocation forest hardening is accounted for according to Taylar equation, such that

$$\tau^{\alpha}_{dis}(T) = b\mu(T)\sqrt{h_{dis}(T)\rho^{\alpha}(T)} \tag{4.1.17}$$

where, b is the magnitude of the Burgers vector, μ is the shear modulus, and ρ^{α}_{dis} is the dislocation density on slip system α. The dislocation density evolution on slip system α is characterized by the phenomenological model proposed by Mecking and Kocks [147]:

$$\dot{\rho}^{\alpha} = \left(\kappa_1\sqrt{\rho^{\alpha}(T)} - \kappa_2(\dot{\varepsilon}, T)\rho^{\alpha}(T)\right)\cdot|\dot{\gamma}^{\alpha}| \tag{4.1.18}$$

where κ_1 and κ_2 are materials parameters represent dislocation generation and annihilation processes, respectively. Their relation is adopted from Beyerlein and Tome's

work [148] as

$$\frac{k_2^\alpha(\dot{\varepsilon},T)}{k_1} = \frac{\chi b}{g^\alpha}\left(1 - \frac{k_B T}{D^\alpha b^3} ln \frac{\dot{\varepsilon}}{\dot{\varepsilon}_0}\right) \tag{4.1.19}$$

where χ, g^α, and D^α are interaction parameter (between 0.1 and 1.0), normalized activation energy, and proportionality factor, respectively. The reference strain rate, $\dot{\varepsilon}_0$ is taken as 10^{7} s^{-1}.

4.1.4 Lattice friction model based on kink-pair mechanism

In FCC materials, dislocations are commonly observed to dissociate into partials and forms stacking faults. The planar core structure leads to frictionless gliding of dislocations even in some high stacking fault energy material (e.g., Al), so the intrinsic lattice friction term can be in crystal plasticity formulation. However, in BCC materials, the core of screw dislocation have a non-planar structure which is characterized by the isotropic/anisotropic spreading on three {110} planes [149, 150]. Dislocation motion is thus characterized by the formation and propagation of kink-pairs, as shown in Figure 4.3. In this process, the kinks have high mobility that can propagate effortlessly and the dislocation gliding is controlled by the thermally activated motion of the screw dislocations. Therefore, an accurate formulation of lattice friction resistance at various temperatures and strain rates is required.

Within Seeger's [151, 152] kink-pair model, the macroscopic plastic strain rate $\dot{\gamma}_p$

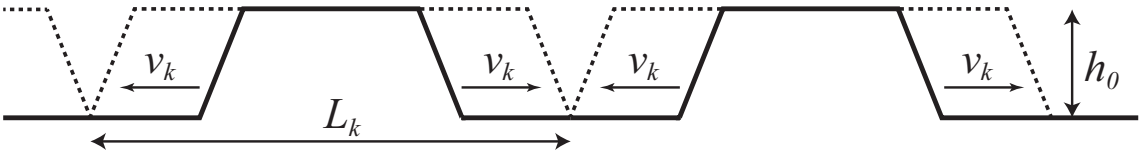

Figure 4.3: Kink-pair formation and expansion. The horizontal line segment represents the screw dislocations, and the kinks having height of h_0 propagate at a velocity v_k. The mean free path length of kink-pairs is L_k. It should be noted that the mobility of two kinks is generally high, and the propagation is relatively easy.

is related to the internal dislocation behavior through Orowan's equation:

$$\dot{\gamma}_p = b\rho_m v(\tau,\ T) \tag{4.1.20}$$

where b is the magnitude of Burgers vector, ρ_m is mobile dislocation density of <111> screw dislocations. The dislocation velocity $v(\tau, T)$ is given by

$$v = h_0 \bar{L}_k \Gamma(\tau,\ T) \tag{4.1.21}$$

where h_0 is the spacing of two adjacent Peierls valleys, and $\bar{L}_k$ is the mean distance of a pair of kinks when they become trapped as shown in Figure. 4.3. Γ is the nucleation rate of kink-pairs per unit time per unit length of dislocation line and is expressed as

$$\Gamma = \Gamma_0(\tau, T)\ \exp(-\frac{H^*_{kp}}{kT}(\tau)) \tag{4.1.22}$$

where H^*_{kp} is the activation enthalpy of thedouble kink. The exact form of Γ_0 and detailed discussion about it can be found in [153, 154]. Combining the above equations,

we reach the Arrhenius type of expression

$$\dot{\gamma} = \gamma_0 \exp(-\frac{H^*_{kp}(\tau)}{kT}) \tag{4.1.23}$$

where $\gamma_0 = b\rho_m h_0 \bar{L}_k \Gamma_0$.

Based on the separation distance of two kinks, the activation enthalpy is described in two regimes with different assumptions and can be divided by a critical separation distance, x_c, as shown in Figure 4.4. In the high temperature regime, a bulge is first formed on the straight dislocation, and followed by the formation of two kinks when the leading part reaches the neighboring valley. As the separation x gets larger, the kink-pair interaction is governed by the long-range elastic interactions. The activation enthalpy of two fully formed and well separated kinks can be then described by the elastic-interaction (EI) approximation [155]:

$$H_{kp} = 2H_k - \frac{\psi_0 h_0^2}{2x} - \tau b h_0 x \tag{4.1.24}$$

where H_k is the enthalpy of a kink, ψ_0 is the pre-logarithmic factor of the dislocation line tension $\psi_d = \psi_0 \ln(R/r_0)$, where R and r_0 are the outer and inner cut-off radii of the stress field contributions to the dislocation line tension. More specifically, the second term accounts for the elastic interaction energy and third term describes the work done by external stresses. The above equation of H_{kp} is a function of the separation distance, x. By minimizing the activation energy, H_{kp} at the critical configuration is obtained as [151]

$$H^*_{kp} = 2H_k - 2\alpha\sqrt{\tau}, \text{ with } \alpha = \sqrt{h_0^3 b \psi_0 / 2} \tag{4.1.25}$$

when the critical separation is

$$x_c = \sqrt{\frac{h_0 \psi_0}{2b\tau}} \tag{4.1.26}$$

Plugging Equation 4.1.25 into Equation 4.1.23 yields

$$\tau = \tau_0^{EI} \left(1 - \frac{T}{T_c(\dot{\gamma})}\right)^2 \tag{4.1.27}$$

where $T_c = \frac{2H_k}{k\ln(\dot{\gamma}_0/\dot{\gamma})}$ and $\tau_0^{EI} = \frac{2H_k^2}{\psi_0 b h_0^3}$.

At the low temperature regime, where the separation of kink-pairs is less than the critical value x_c and linear elasticity theory starts to give a poor estimation, Peierls potential is then introduced to describe such interactions. In the line-tension (LT) regime, the governing equation of a dislocation line under external stress is [156]

$$\psi_d \frac{d^2y}{dx^2} - \frac{dU(y)}{dy} + \tau b = 0 \tag{4.1.28}$$

where $\psi_d = \psi_0 \ln(R/r_0)$ accounts for the line tension, and $U(y)$ is the Peierls potential defined as a function of displacement from the position of minimum energy. The kink pair activation enthalpy is thus the energy difference of kink-pair configurations and a straight dislocation under the same stress, which can be written as

$$H_{kp}^* = 2\sqrt{2\psi_d} \int_{y=y_0}^{y=y_{max}} \left[U(y) - U(y_0) - (y - y_0)b\tau\right]^{1/2} \, dy \tag{4.1.29}$$

where y_0 is the equilibrium spacing of a straight dislocation under applied stress τ (i.e., $dU(y)/dy|_{y=y_0} = b\tau$), and upper limit of the integration, y_{max}, is determined from $U(y_{max}) - \tau b y_{max} = U(y_0) - \tau b y_0$. Accordingly, the solution is depend on the shape of the Peierls potential.

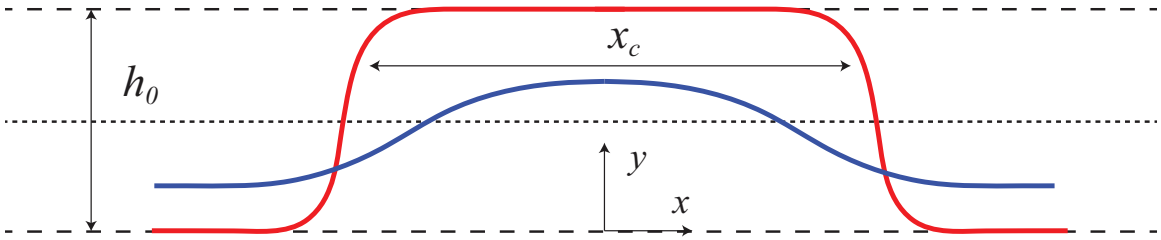

Figure 4.4: Kink-pair configurations at high (red line) and low (blue line) temperature regimes. Dashed line and dotted line indicate energy minima and maximum of Peierls energy, respectively.

Several potentials can be found in the literature, including Eshelby potential [157], sinusoidal potentials [158, 159], and antiparabolic potentials [154, 160]. More details for each potential can be found in [142, 156]. Here, the antiparabolic potential is used, and the activation enthalpy can be written as [154]

$$H_{kp}^{*} = 2H_k \left(1 - \frac{\tau^*}{\tau_0}\right)^2 \tag{4.1.30}$$

Plugging above equation into Equation 4.1.23, the lattice friction, τ^*, can be written as

$$\tau^* = \tau_0 \left(1 - \left(\frac{T}{T_c(\dot{\gamma})}\right)^{\frac{1}{2}}\right) \tag{4.1.31}$$

Along with Equation 4.1.27, the analytical expression for τ^* at $0 < T < T_c(\dot{\gamma})$ is

$$\boxed{\tau^* = \begin{cases} \tau_0 \left(1 - \left(\frac{T}{T_c(\dot{\gamma})}\right)^{\frac{1}{2}}\right) & 0 < T < \tilde{T}(\dot{\gamma}) \\ \tau_0^{EI} \left(1 - \frac{T}{T_c(\dot{\gamma})}\right)^2 & \tilde{T}(\dot{\gamma}) < T < T_c(\dot{\gamma}) \end{cases}} \tag{4.1.32}$$

where

$$T_c(\dot{\gamma}) = \frac{2H_k}{k_B \ln(\dot{\gamma}_0/\dot{\gamma})} \tag{4.1.33}$$

It should be mentioned that $T_c(\dot{\gamma})$, which is referred to as the critical or athermal temperature in literature, is defined on the atomic scale that signifies the temperature beyond which the lattice friction becomes zero. It is different than the brittle-to-ductile transition temperature (BDTT), which is commonly determined from macroscale experiments and is sensitive to the microstructure and testing methods [111, 161]. Moreover, T_c is rate-dependent and a higher strain rate leads to a higher T_c as schematically shown in Figure 4.5. In contrast, the dividing temperature $\tilde{T}(\dot{\gamma})$ is simply defined as a numerical parameter instead as opposed to have any physical significance because the temperature-dependent configuration of kink-pair is a continuous process. Also, it is important to realize that the pre-factor coefficients (i.e., τ_0) in LT regime expression represents the minimum stress minimum stress required for a dislocation to overcome a Peierls valley without the aid of thermal activation.

The next step is to determine the material parameters in Equations 4.1.32 and 4.1.33 by fitting with data from bulk single crystal experiments at various temperatures and strain rates. There are 4 out of 5 total parameters are independent, including τ_0, τ_0^{EI}, and any two combinations from H_k, $\dot{\gamma_0}$ and $T_c(\dot{\gamma})$. The EI and LT models shares all the other parameters except the pre-factor stress, so, theoretically, $2H_k$ and $\dot{\gamma_0}$ can be determined from either temperature regime. For example, τ_0^{EI}

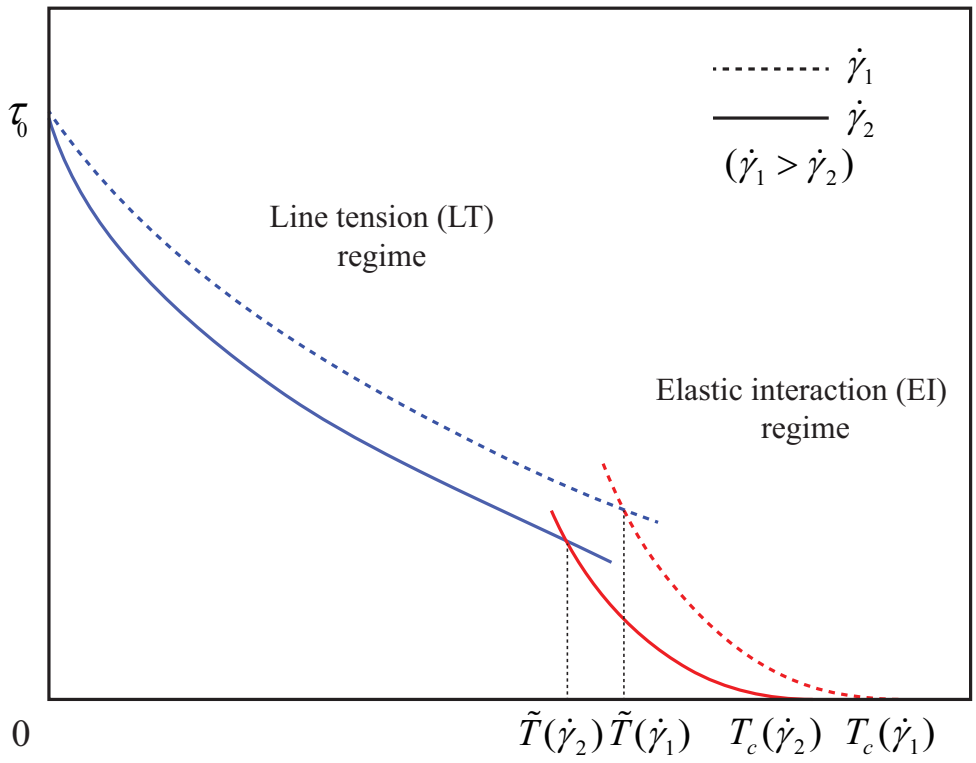

Figure 4.5: Illustration of kink-pair theory prediction of τ^* from 0 K to $T_c(\dot{\gamma})$ at different strain rates. Dashed and solid lines indicate high and low strain rates, respectively.

and $T_c(\dot{\gamma})$ can be obtained through a linear fit between experimentally measured $\sqrt{\tau^*}$ and testing temperature, T, at each strain rate. $2H_k$ and γ_0 and then obtained by linear fitting of $1/T_c(\dot{\gamma})$ and $\ln\dot{\gamma}$ with the data in EI regime. Lastly, τ_0 is determined through experimental data in LT regime. More details of this process applied on tungsten will be discussed in Section 4.4.1.

4.2 Numerical Implementation of Crystal Plasticity Constitutive Model

User defined constitutive relationships can be implemented into Abaqus through the UMAT or VUMAT subroutine. For performing static/quasi-static simulations using the Abaqus/standard solver, an accurate and efficient implicit time integration scheme is required in the UMAT subroutine.

Backward Euler discretization on $\dot{\mathbf{F}}^p$ at time t in Equation 4.1.11 yields

$$\mathbf{L}_t^p = \left(\frac{\mathbf{F}_t^p - \mathbf{F}_{t-\Delta t}^p}{\Delta t}\right) \mathbf{F}^{p-1}_t \tag{4.2.1}$$

By introducing Equation 4.1.11 into above equation gives

$$\mathbf{F}_t^{p-1} = \mathbf{F}_{t-\Delta t}^{p-1} \left(\mathbf{I} - \sum_{\alpha=1}^{n_{slip}} \Delta t \ \dot{\gamma}^\alpha \mathbf{S}_0^\alpha\right) \tag{4.2.2}$$

Applying the above equation along with the elasto-plastic decomposition (i.e., Equation 4.1.6) to the constitutive relation (i.e., Equation 4.1.8) and neglecting the high

order $O(\Delta t^2)$ terms yields

$$\mathbf{S}_t = \mathbf{S}^{tr} - \sum_{\alpha=1}^{n_{slip}} \Delta\gamma^{\alpha}(\mathbf{S}_t, s_t^{\alpha})\mathbf{B}^{\alpha} \tag{4.2.3}$$

where

$$\mathbf{S}^{tr} = \mathbb{C} : \frac{1}{2}\left(\mathbf{A} - I\right) \tag{4.2.4}$$

$$\mathbf{B}^{\alpha} = \mathbb{C} : \frac{1}{2}\left(\mathbf{A}\mathbf{S}_0^{\alpha} + \mathbf{S}_0^{\alpha T}\mathbf{A}\right) \tag{4.2.5}$$

and

$$\mathbf{A} = \mathbf{F}_{t-\Delta t}^{p-T}\mathbf{F}_t^T\mathbf{F}_t\mathbf{F}_{t-\Delta t}^{p-1} \tag{4.2.6}$$

Finally, the new slip resistance is updated using Equation 4.1.15 as

$$s_t^{\alpha} = \tau^* + \tau_{GB} + b\mu\sqrt{h_{his}\rho_t^{\alpha}(\Delta\gamma(\mathbf{S}_t, s_t^{\alpha}))} \tag{4.2.7}$$

and the dislocation density is updated through Equation 4.1.18 as

$$\rho_t^{\alpha} = \rho_{t-\Delta t}^{\alpha} + |\Delta\gamma| \cdot \left(k_1\sqrt{\rho_{t-\Delta t}^{\alpha}} + k_2\rho_{t-\Delta t}^{\alpha}\right) \tag{4.2.8}$$

Now Equations 4.2.3 and 4.2.7 form a set of nonlinear, simultaneous equations of $\mathbf{S_t}$ and s_t^{α} that can be solved through a two-level iteration [162]. In the first level, s_t^{α} are fixed, and $\mathbf{S}_t$ is searched through Newton-Raphson iteration. With the converged $\mathbf{S}_t$, the second level of iteration becomes a simple update of new slip resistances s_t^{α} based on the new dislocation density as updated with Equation 4.2.8. This two level iterative process is repeated until both $\mathbf{S_t}$ and s_t^{α} have converged.

Within the first (inner) level of iteration at time t, a residual $\mathbf{R}$ is defined at step i when using Newton-Raphson method, such that

$$\mathbf{R}_t^i = \mathbf{S}_t^i - \mathbf{S}^{tr} + \sum_{\alpha=1}^{n_{slip}} \Delta\gamma^\alpha(\mathbf{S}_t^i, {s_j}^\alpha) \tag{4.2.9}$$

Then, an updated estimate of $\mathbf{S}_t$ from step i to step i+1 is calculated through

$$\mathbf{S}_t^{i+1} = \mathbf{S}_t^i - \left[\frac{\partial \mathbf{R}^i}{\partial \mathbf{S}_t^i}\right]^{-1} \mathbf{R}_t^i \tag{4.2.10}$$

with

$$\left[\frac{\partial \mathbf{R}_t^i}{\partial \mathbf{S}_t^i}\right]^{-1} = \mathbb{I} + \sum_{\alpha=1}^{n_{slip}} \mathbf{B}^\alpha \otimes \frac{\partial}{\partial \mathbf{S}_t^i}\left[\Delta\gamma^\alpha(\mathbf{S}_t^i, {s_j}^\alpha)\right] \tag{4.2.11}$$

subscript j in s_j^α in Equations 4.2.9 and 4.2.11 refers to jth iteration of second level (outer) iteration at the current time step.

In addition to the above time integration scheme, the Abaqus/Standard solver requires computation of the Jacobian matrix to solve for nodal displacements in non-linear FEM simulations. Although a poor approximation of the Jacobian matrix will not lead an incorrect solution, an accurate evaluation of the Jacobian matrix is important for achieving a better convergence rate. This could be obtained through a numerical perturbation procedure [162]; for computational efficiency, an analytical formulation derived by Balasubramanian [163] is adopted in the current Abaqus UMAT subroutine. For better demonstration, the detailed computational procedure

for the above implicit-time integration scheme is summarized in Algorithm 1.

Algorithm 1: time integration algorithm for Abaqus UMAT subroutine

Input: $\mathbf{F}_t$, $\mathbf{F}_{t-\Delta t}$, $\mathbf{SDV}_{t-\Delta t}$ ($\rho^{\alpha}_{t-\Delta t}$, $\mathbf{S}_{t-\Delta t}$), Δt

Output: σ_t, $\mathbf{SDV}_t$ (ρ^{α}_t, $\mathbf{S}_t$), $\frac{\partial \Delta \sigma}{\partial \Delta \varepsilon}$

Initialization(slip system, read SDVs);

Compute $\mathbf{A}$, $\mathbf{B}^{\alpha}$, $\mathbf{S}^{tr}$ based on equations 4.2.4, 4.2.5, 4.2.6;

while $\Delta s_{max} > \Delta s_{tol}$ **do**

  while redisual $\mathbf{R}^i_t > \mathbf{R}_{tol}$ **do**

    calculate $\Delta\gamma^{\alpha}(\mathbf{S}^i_t, {s_j}^{\alpha})$ using equation 4.1.13;

    calculate $\mathbf{R}^i_t$ using equation 4.2.9;

    calculate $\left[\frac{\partial \mathbf{R}^i}{\partial \mathbf{S}^i}\right]^{-1}$ using equation 4.2.11;

    update stress $\mathbf{S}^{i+1}_t$ using equation 4.2.10;

    update shear slip $\Delta\gamma^{\alpha}(\mathbf{S}^{i+1}_t, {s_j}^{\alpha})$;

    evalutaion new residual $\mathbf{R}^{i+1}_t$;

    increase iteraction counter, such that i = i+1;

  compute new dislocation density ρ^{α}_t using equation 4.2.8;

  compute new slip resistance s^{α}_{j+1} using equation 4.2.7;

  compute $\Delta s_{max} = \left| max(s^{\alpha}_{j+1} - s^{\alpha}_j)_{\alpha} \right|$;

Update $\mathbf{SDV}_t$ (i.e. ρ^{α}_t, $\mathbf{S}_t$);

Calculate Cauchy stress tensor σ;

Compute Jacobian matrix (i.e. $\frac{\partial \Delta \sigma}{\partial \Delta \varepsilon}$);

4.3 Cohesive Zone Model

4.3.1 A Brief Introduction

The concept of cohesive zone was first conceived by Barenblatt [164] and Dugdale [165] in their work on analyzing the failure process near the crack tip. In this formulation, a fracture process zone is incorporated ahead of the idealized infinite sharp crack, where singularity showed up based on linear fracture mechanics. Within the zone, the interface is described by a traction-separation relation. This is a "top-down" approach for modeling crack initiation and propagation using a continuum description, which generally requires experimental calibration at the small scale [166]. For its natural compatibility with the framework of continuum mechanics, the idea is quickly spawned and was introduced into a computational framework by Hillerborg et al. [167]. Since then, it has been used to investigate fractures on a wide range of materials (e.g., metals [168], polymers [169], ceramics [170], composites [171] etc..) under different loading conditions [170, 172, 173].

One of the key the aspects in utilizing the cohesive zone formulation to model material fracture lies on the development of the traction-separation constitutive relationship that is able to accurate describe the failure process [174]. Major progress on this aspect is briefly summarized here. In the early work of Dugdale [165], in order to solve the plastic zone ahead of steel sheets containing slits, he assumed the stress

within the cohesive zone is constant and is equal to the yield stress of the material. In his analysis, the cohesive zone extent is an output whereas later computational work based on FEM requires the extent of cohesive surfaces to be specified as an input before simulation. Needleman proposed a cubic polynomial [175] and an exponential [176] function based CZMs, which is defined by two parameters, cohesive strength and work of separation, to study the matrix-particle decohesion. Later, Tvergaard and Hutchinson [177] proposed a trapezoidal shape multi-linear CZM to study the crack growth during peeling of the adhesive metal joints. Geubelle and Baylor [178] developed a bilinear triangular-shaped traction-separation relationship to study delamination in composites subjects to low-velocity impact. In these studies, cohesive elements were inserted before simulation which is referred to as an intrinsic cohesive formulation in the literature. Meanwhile, these CZMs have an initial elastic regime before reaching the cohesive strength. This results in an extra system compliance and leads to size dependent elastic wave speed in dynamic simulation. To address such issues, Camacho and Ortiz [170] developed so-called extrinsic cohesive formulation in which cohesive elements are dynamically inserted when some criterion is satisfied and the initial elastic region is removed. Regarding the recent progress, the PPR model [179] proposed by Park, Paulino, and Roester which has been widely used for mixed-mode fractures is also worth mentioning [180, 181].

These above mentioned constitutive relationships as well as those that exist in the literatures can be classified as either potential-based or nonpotential-based mod-

els. In potential-based models, for example, the PPR model, the traction-separation relation is derived by taking the first derivative of the energy potential, which automatically guarantees the consistency of constitutive relationships for arbitrary mixed-mode conditions. On the other hand, the nonpotential-based models do not possess such a property, but they are relatively easy to develop because a symmetric system is not required.

4.3.2 Cohesive Zone Formulations in Abaqus

Most implementations of CZM into the FEM framework rely on the cohesive element, which is inserted at element boundaries either before or during the simulation. This approach is easy to implement because there is no fundamental difference between cohesive element compares solid elements but with a different constitutive response. Abaqus [182] offers an alternative approach to implement CZMs based on surface contact formulation, which is commonly termed as cohesive surface/contact approach. In other words, the traction-separation model becomes an interaction/contact property, not a material property. Compared to element-based formulation, it has the following advantages [182]: (1) tracking relative geometric relation using the built-in contact-based algorithm avoids penetration or other unphysical geometric relationship; (2) allows specification of post-failure cohesive behavior if the failed surfaces come into re-contact; (3) can be used to model "sticky" contact (i.e., free surfaces can bond after coming into contact); (4) allows the utilization of traction-separation

relationships in conjunction with other contact formulations (e.g., friction) to model more complex phenomena at interface; (5) improved numerical convergence has also been reported [183].

Abaqus has implemented various traction-separation models in its library which assume initially linear elastic behavior followed by damage initiation and evolution [182]. Multiple criteria for damage initiation are available and they are: MAXS (maximum stress criterion), MAXE/U, (maximum strain/separation criterion), QUADS (quadratic stress criterion), and QUADE/U (quadratic strain/separation criterion). Regarding the damage evolution, it can be defined through either the effective displacement or energy dissipation. If the damage evolution is based on energy dissipation, the dependence of the fracture energy on the mode mix can be defined through a power law, or Benzeggagh-Kenane form [184] or mode-independent. For the shape of the damage evolution function, linear, exponential, as well as tabular are supported.

4.4 Evaluation of the Constitutive Model

4.4.1 Estimation of Tungsten Lattice Friction from Kink-pair Theory

Fitting material parameters in the kink-pair theory requires accurate experimental measurement of CRSS at various temperatures and strain rates. To avoid variance due

to the random initial dislocation microstructures, the Ackerman-Mughrabi technique is commonly adopted [185], where samples are cyclically pre-deformed to produce a very stable dislocation cell structure before testing. This method has been used for measuring CRSS of a wide range of BCC metals, including tantalum [186], niobium [187], and molybdenum [188]. Unfortunately, CRSS data on W measured with such method is not available, so the CRSS reported by Brunner and Glebovsky [5, 189] using the lower yield point will be used for the fitting.

In Brunner and Glebovsky's experiments [5, 189], high-purity W single crystals were grown using high-vacuum electron-beam floating zone melting technique [190, 191] with a dislocation density approximated to be 5.5×10^9 m^{-2} [192]. The bulk crystal bar with a diameter of 10 mm was spark-machined and finally polished into a dog-bone shape with guage diameter and length of 0.9 mm and 14 mm, respectively. The longitudinal/tensile direction was measured to have a crystallographic orientation of [1 4 9] which corresponds to a Schmid factor (SF) of 0.5 for <110>{111} slip systems. Two types (namely, type-A and type-B) of tensile testing were carried out at a constant uniaxial strain rate $\dot{\gamma}_{rss} = 1.7 \times 10^{-3}$ s^{-1}. In type-A tests, specimens were isothermally deformed to fracture, however, the parabolic-shaped hardening response in the stress-strain curve presents a challenge in quantifying the CRSS, so type-B tests were then introduced. Samples are successively deformed in small strain intervals at several (decreasing) temperatures after being first deformed at T > 600 K. Negligible hardening was observed and the stress at the plateau and lower yield points from

type-B tests were used. During both types measurement methods, stress relaxation experiment (SRE) were also performed by arresting the cross-head and recording the decay of applied load with time which allows for calculation of thermal activations parameters that will be used in the fitting process.

To exclude the contribution of the athermal stress component, τ^* is obtained by subtracting the CRSS at the highest testing temperature (i.e., 11.65 MPa at 785 K), where τ_0^{EI} and $T_c(\dot{\gamma})$ are calculated based on the linear fit between $\sqrt{\tau^*}$ and T using the results above 600 K. This gives $T_c = 797.5K$ which is 0.215 T_m (i.e., melting temperature) and agrees well with T_c found for other BCC materials [185, 186, 188]. Similarly, τ_0 is then fitted by using lower temperature data with the assumption that the formation enthalpy of isolated kink-pair $2H_k$ is maintained across all temperature regimes [120, 142]. Therefore, all the parameters at strain rate $\dot{\varepsilon} = 1.7 \times 10^{-3}$ are determined, and the fitted curves are plotted along with experimental data in Figure 4.6. To predict τ^* at different strain rates, a reference strain rate $\dot{\gamma_0}$ in Equation 4.1.33 needs to be determined that can be obtained from a linear fit between $1/T_c(\dot{\gamma_0})$ and $\ln(\dot{\gamma})$. However, as the experiments were only carried out at one strain rate, $\ln(\dot{\gamma_0}/\dot{\gamma}) = 30.7$ was calculated from SRE data is used here (for further details refer to [120]). Figure 4.6 depicts the results from experiments and the kink-pair theory with fitted parameters that are summarized in Table 4.1.

Table 4.1: Experimentally fitted parameters used in EI and LT models for W

τ_0 (MPa)	τ_0^{EI} (MPa)	$2H_k$ (eV)	$\dot{\gamma}_0$
1036	2057	2.06	3.66×10^{10}

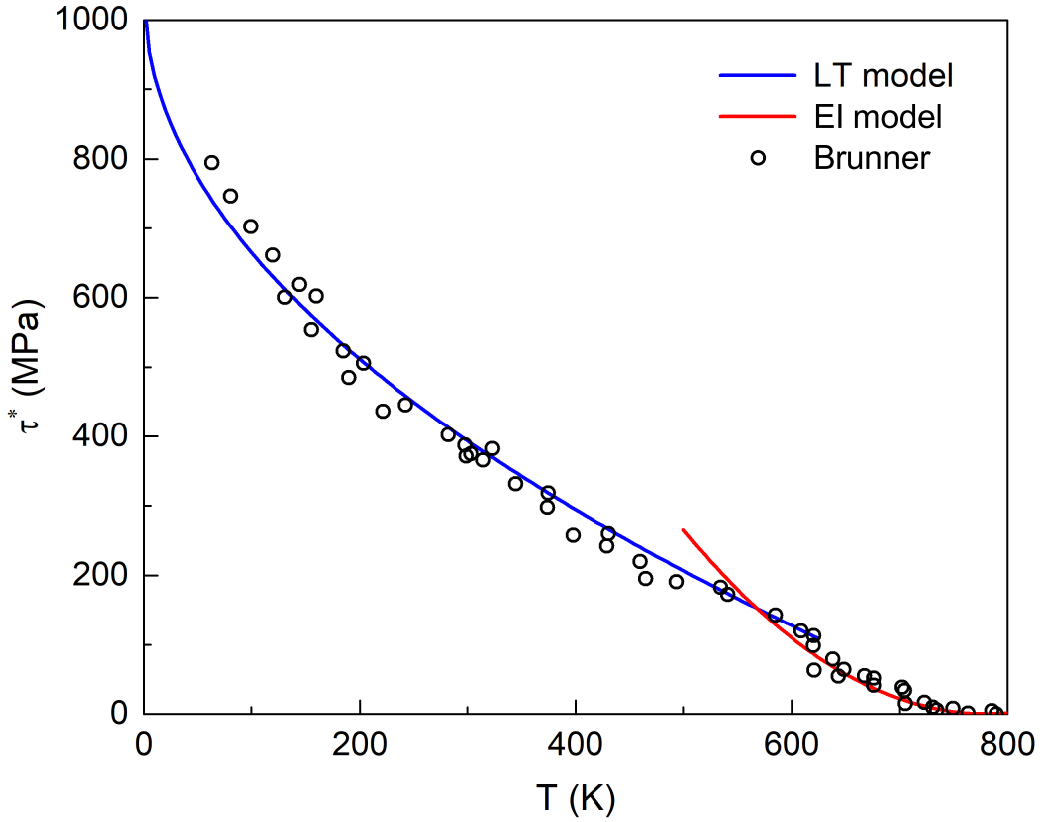

Figure 4.6: Plot of measured [5] and fitted τ^* using EI and LT models. The athermal contribution in the experimental data is excluded by subtracting the resolved shear stress at the highest testing temperature.

4.4.2 Estimation of Material Parameters for Tungsten

Elastic moduli

BCC materials possess cubic symmetry which require 3 independent elastic constants (i.e., $C11$, $C12$, and $C44$) to establish the relationship between stress and strain as

$$\begin{pmatrix} \sigma_{11} \\ \sigma_{22} \\ \sigma_{33} \\ \sigma_{23} \\ \sigma_{13} \\ \sigma_{12} \end{pmatrix} = \begin{pmatrix} C_{11} & C_{12} & C_{12} & 0 & 0 & 0 \\ & C_{11} & C_{12} & 0 & 0 & 0 \\ & & C_{11} & 0 & 0 & 0 \\ & \vdots & & C_{44} & 0 & 0 \\ & sym & \cdots & 0 & C_{44} & 0 \\ & & & 0 & 0 & C_{44} \end{pmatrix} = \begin{pmatrix} \varepsilon_{11} \\ \varepsilon_{22} \\ \varepsilon_{33} \\ \varepsilon_{23} \\ \varepsilon_{13} \\ \varepsilon_{12} \end{pmatrix} \tag{4.4.1}$$

Lowrie and Gonas [121] utilized ultrasonic wave velocity measurements to quantify elastic properties from room temperature to 2100 K and the fitted quadratic form is adopted here:

$$C_{11} = (536.04 - 4.2980 \times 10^{-2}T - 5.4670 \times 10^{-6}T^2) \text{ GPa} \tag{4.4.2}$$

$$C_{12} = (205.14 - 1.6281 \times 10^{-2}T - 3.2490 \times 10^{-6}T^2) \text{ GPa} \tag{4.4.3}$$

$$C_{44} = (163.50 - 9.1979 \times 10^{-2}T - 2.0540 \times 10^{-6}T^2) \text{ GPa} \tag{4.4.4}$$

Slip systems

Identifying correct slip systems in tungsten (as well as other BCC metals) has

always been challenging due to the high probability of cross-slip of screw dislocations [193]. It's commonly accepted that all slips happens along the closed packed <111> direction; however, dislocations can glide on the {112} and {123} planes, which have smaller interplanar spacing than {110} planes. Thus, there are in total 48 candidate slip systems, including 12 {110}<111>, 12 {112}<111>, and 24 {123}<111>.

There are a few macro-scale tension tests on single crystal tungsten that can be found in literature [194–196], however, all of them reported difficulties in identifying active slip systems. In these experiments, an extensive amount of fine and short slip lines were observed on the sample surface which could either originate from {110} or {112} planes due to the cross-slip of screw dislocations. Kim et al. [197] carried out micro-scale tension and compression on submicron sized BCC metals (i.e., W, Mo, Ta, Nb) and followed by SEM analysis. They claimed slip traces on sample surface were too wavy, and only niobium showed clear slip bands along {110} planes. Micro-compression experiments on 5 μm W micropillars [4] showed similar wavy deformation mode. Nevertheless, it is generally agreed that slip happens on {110} and {112} planes. As such, 12 {110}<111> and 12 {112}<111> slip systems (listed in Table 4.2) are considered in the CPFEM simulations.

Flow and hardening parameters

Most of the flow and hardening parameters used in this work are adopted from visco-plastic self-consistent (VPSC) modeling of W work by Terentyev et al. [1], where parameters were calibrated with experiments carried out above 600 K. Considering

Table 4.2: Slip systems for CPFEM simulation

α	$[\mathbf{n}_0^\alpha]_{\{110\}}$	α	$[\mathbf{n}_0^\alpha]_{\{112\}}$	$\mathbf{m}_0^\alpha$
1	(110)	13	(211)	$<\bar{1}11>$
2	(110)	15	(121)	$<1\bar{1}1>$
3	(101)	14	(112)	$<11\bar{1}>$
4	$(10\bar{1})$	16	$(\bar{2}11)$	$<111>$
5	(101)	21	$(12\bar{1})$	$<\bar{1}11>$
6	(011)	17	$(\bar{1}12)$	$<1\bar{1}1>$
7	(011)	18	$(\bar{1}21)$	$<11\bar{1}>$
8	$(01\bar{1})$	20	$(11\bar{2})$	$<111>$
9	$(01\bar{1})$	23	$(1\bar{1}2)$	$<\bar{1}11>$
7	$(01\bar{1})$	19	$(21\bar{1})$	$<1\bar{1}1>$
10	(011)	22	$(2\bar{1}1)$	$<11\bar{1}>$
12	$(10\bar{1})$	24	$(1\bar{2}1)$	$<111>$

that the current work focuses on a lower temperature regime (i.e., 293 K-673 K), slight adjustments were made on those temperature-dependent parameters. For succinctness, only the changes are discussed in this section.

In their work, the Hall-Petch coefficient k_{HP} was experimentally measured at various temperatures and is shown in Table 4.3. It shows a linear dependence between T and k_{HP} such that $k_{HP} = a - T \cdot b$, where $a = 0.72\,\mathrm{MPa} \cdot \sqrt{\mathrm{m}}$ and $b = 3.42 \times 10^{-4}\,\mathrm{MPa} \cdot \sqrt{\mathrm{m}} \cdot \mathrm{K}^{-1}$. They attributed the negative proportional relationship to the thermally-activated absorption and transition of dislocations at the grain boundaries since these activities are enhanced at higher temperatures. Using this relation and extrapolating to lower temperatures gives $0.49\,\mathrm{MPa} \cdot \sqrt{\mathrm{m}}$(673K), $0.52\,\mathrm{MPa} \cdot \sqrt{\mathrm{m}}$(573 K), $0.58\,\mathrm{MPa} \cdot \sqrt{\mathrm{m}}$(423 K), and $0.62\,\mathrm{MPa} \cdot \sqrt{\mathrm{m}}$ (293 K). This extrapolation may lead to an overestimation of the Hall-Petch effect at the lower temperature regime, thus, considering the temperature range in this work, k_{HP} is set to be $0.5\,\mathrm{MPa} \cdot \sqrt{\mathrm{m}}$, which is also supported by the experimental measurements on UFG tungsten [198, 199].

Regarding the dislocation interaction parameter h_{dis} in the Taylor hardening relation (i.e., Equation 4.1.17), extrapolation based on the experimental calibration at 600 K- 800 K in [1] is used. Using the relationship $h_{dis} = c - T \cdot d$ with c =0.38 and d = $4 \times 10^{-4}\,\mathrm{K}^{-1}$, the values of h_{dis} at different temperatures used in the current study is listed in Table 4.4. It should be mentioned that τ_{dis} is proportional to the square root of h_{dis} and Taylor hardening only contributes a small portion to flow stress, the

bias introduced by extrapolation will be limited. All other parameters are directly adopted from [1] and are listed in Table 4.5

Table 4.3: Temperature-dependent Hall-Petch strengthening coefficient k_{HP} measured from experiments [1].

Temperature (K)	773	873	1273
k_{HP} (MPa $\cdot \sqrt{\text{m}}$)	0.45	0.42	0.28

Table 4.4: Temperature-dependent dislocation interaction coefficient h_{dis} used in current study.

Temperature (K)	293	423	573	673
h_{dis}	0.26	0.21	0.15	0.11

4.4.3 Evaluation the Crystal Plasticity Model for a Single Grain

Before directly applying the above proposed CP model and parameters into the imaged-based simulation, a few simple simulation cases are carried out on single crystal for validation and demonstration purposes. In these cases, uniaxial tension is performed on a single C3D8 element up to 15% engineering strain at a constant engineering strain rate of 10^{-3} s^{-1} and then plotted as true stress versus true strain

Table 4.5: Flow and hardening paramters adopted from [1] and used in the simulations.

Parameter	Definition	Value	Unit	Used in equation
$\dot{\gamma}_0^\alpha$	reference shear rate	10^{-3}	s^{-1}	4.1.13
m	strain rate sensitivity coefficient	0.02	-	4.1.13
k_{HP}	Hall-Petch coefficient	0.50	MPa$\cdot\sqrt{m}$	4.1.16
b	magtitude of Burger's vector	0.274	nm	4.1.17
κ_1	Kocks-Mecking parameter	4.8×10^8	m^{-1}	4.1.17
g^α	normalized activation energy	2.8×10^3	-	4.1.17
D^α	proportionality constant	10^4	MPa	4.1.18
$\dot{\varepsilon}_0$	reference strain rate	10^7	s^{-1}	4.1.19

using Equations 2.5.4 and 2.5.5.

To begin with, true stress-strain curves at four temperatures in which our *in situ* experiments were carried out is shown in Figure 4.7. The simulation is performed on a [001]-oriented single crystal with a initial dislocation density of 10^{12} m^{-2}. At this temperature regime, the response shows strong temperature dependence and in great accordance with the predications from kink-pair theory and experimental measurements. Based on Schmid's law, 4 out of 12 {112}[111] type of slip systems possesses the maximum Schmid factor (i.e., 0.471) and are activated in this case.

To demonstrate the effect of loading direction, true stress-strain curves of crystals with three different crystallographic orientations (i.e., [$\bar{1}$11], [112], [$\bar{1}$49] with Schmid

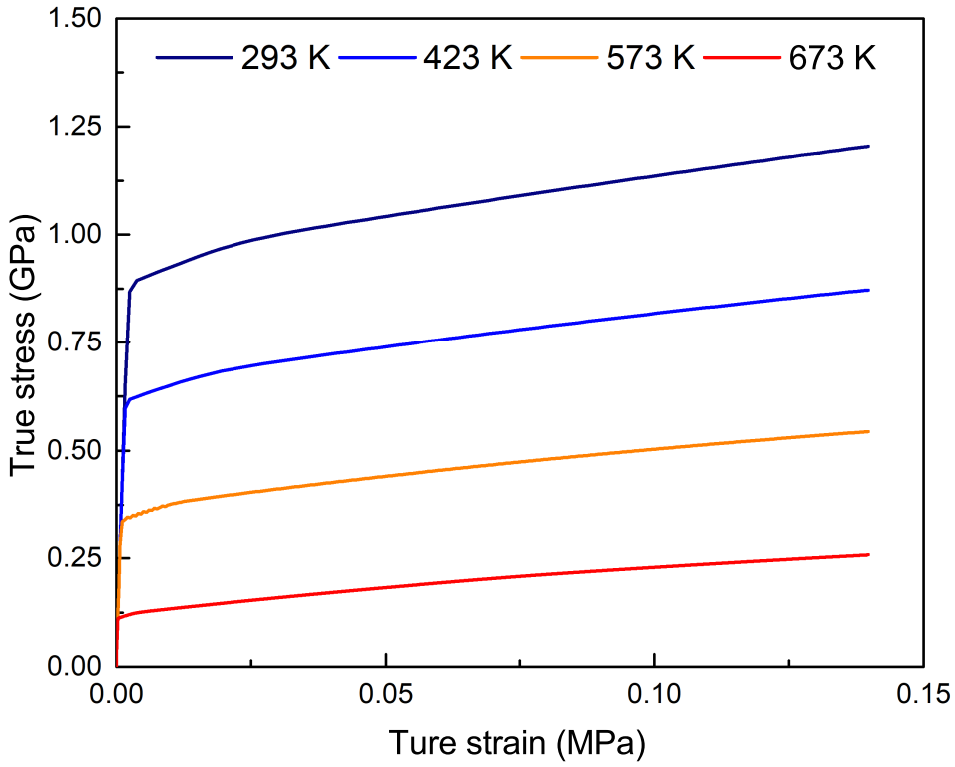

Figure 4.7: The true stress-strain responses of a [001]-oriented single crystal W at different temperatures with a constant strain rate of $1 \times 10^{-3}\,\mathrm{s}^{-1}$.

factor of 0.272, 0.408, 0.500) with aspect loading axis are presented in Figure 4.8. For clearness, only the lowest temperatures (i.e., 293 K) results are shown.

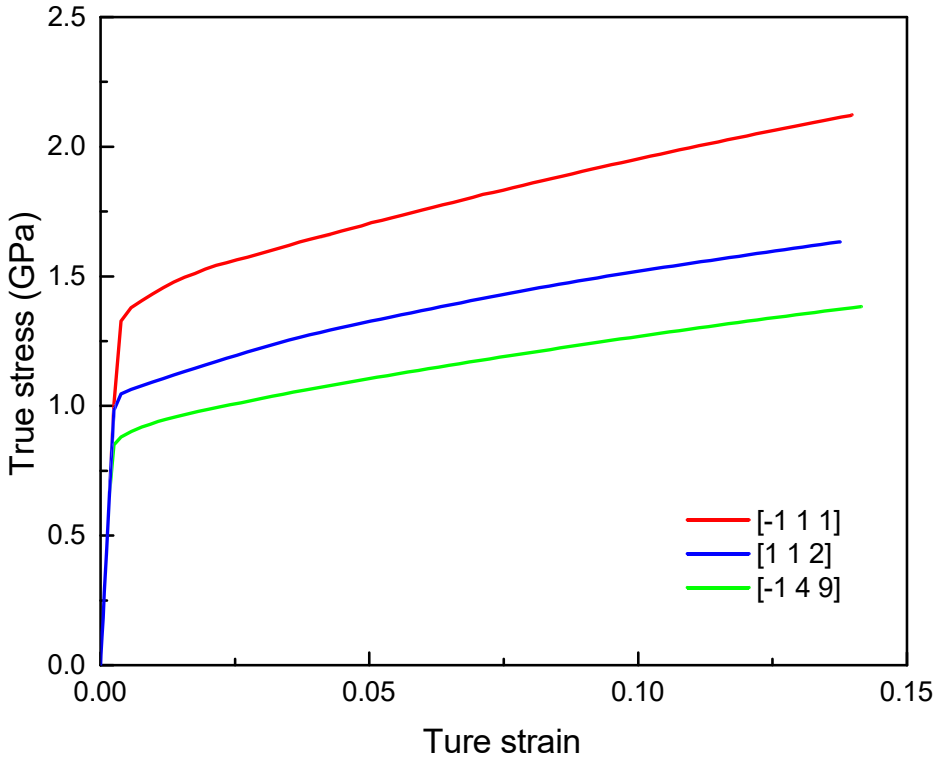

Figure 4.8: True stress-strain responses of [-1 1 1],[1 1 2] and [-1 4 9] oriented single crystal W specimens at 293 K. The Schmid factors for these crystals are 0.272, 0.408, and 0.500, respectively.

The dislocation density evolution for a $[\bar{1}49]$-oriented crystal is loaded at 293 K and 673 K in uniaxial-tension at a engineering strain rate 10^{-3} of and dislocation evolution of the four slip systems with different SF between 0 and 0.5 are shown in Figure 4.9. At 293 K, only slip systems with SF larger than 0.26 are activated, and the slip system that possesses the highest SF was activated at a very small strain and finally reached

a dislocation density on the order of 10^{14} m^{-2}. For the $(211)[\bar{1}11]$ slip system that has a SF of 0.37, it was activated at about 3% of true strain before which plasticity was exclusively activated on the $[\bar{1}01][111]$ slip system. For slip systems with a SF less than 0.26, the dislocation density remains as constant during the deformation indicating these system was not contributors to plastic deformation. At 673 K, in contrast to 293 K, the $(\bar{1}21)[11\bar{1}]$ slip systems were activated at $\sim 3\%$ strain. However, the $(\bar{1}01)[111]$ slip system exhibited a lower final dislocation density compares to 293K, and this is attributed to the lower dislocation interaction parameter (i.e., h_{dis}), which decreases with increasing temperature. However, it is observed that more slip systems were activated, which reflects the enhanced plasticity at elevated temperatures.

To finish the discussion on the constitutive response, the effect of initial dislocation density is investigated and shown in Figure 4.10. At 293 K, one order of magnitude difference initial dislocation density leads to less than a 20 MPa variation in both yield strength and flow strength; at 673 K, this difference is further reduced due to the smaller h_{dis}. The observed small variation, on one hand, is attributed to the small contribution of Taylor hardening to the total slip resistance throughout the deformation; on the other hand, for the lower initial dislocation density case, dislocations multiplies quickly during the initial loading. As shown in Figure 4.10(b), for the $\rho_0 = 10^{11}$ case, dislocation density on primaty slip system (i.e., $(\bar{1}01)[111]$) ramps up quickly and catches up to 10^{12} m^{-2} within 0.005 true strain.

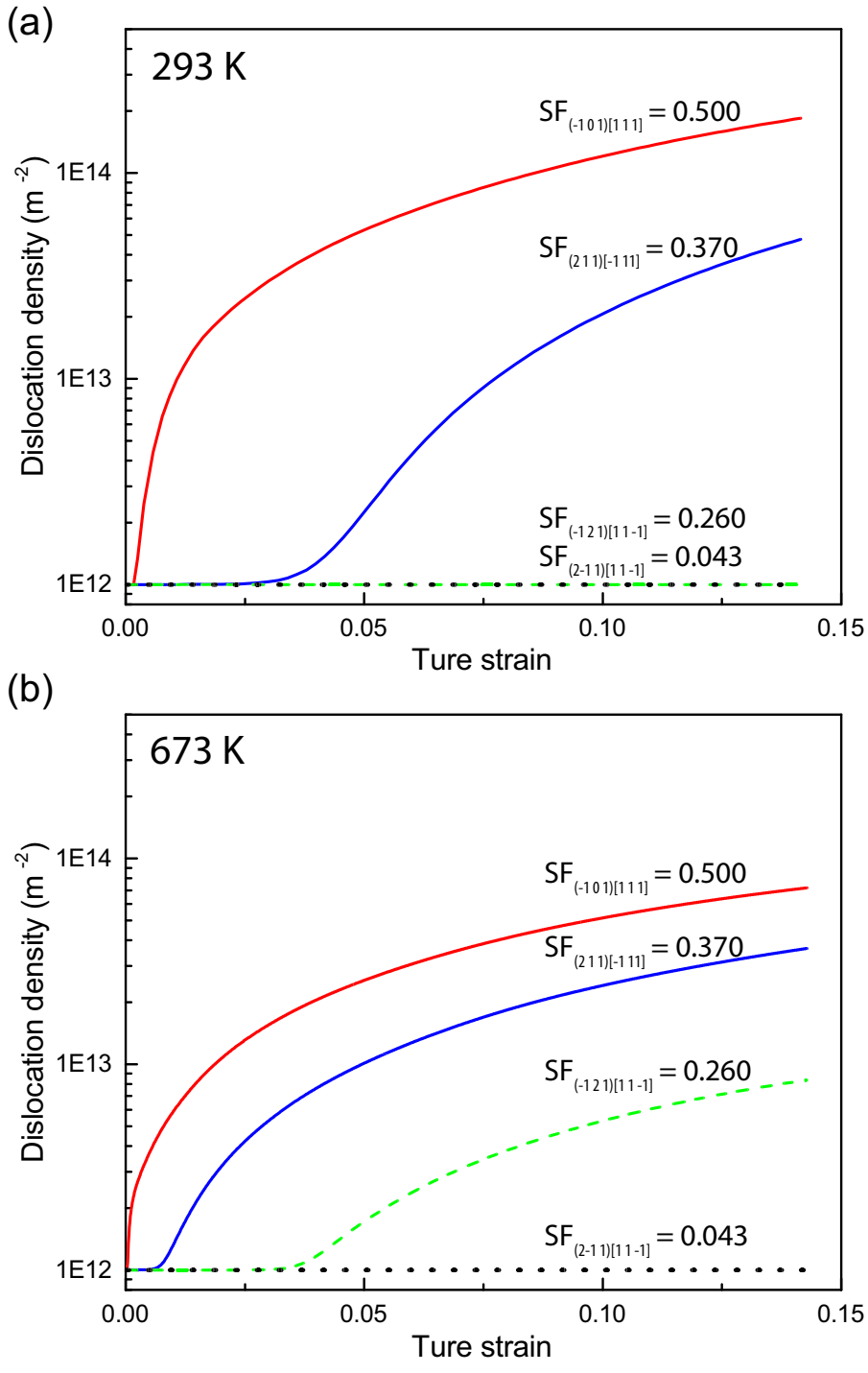

Figure 4.9: Dislocation evolution of a $[\bar{1}49]$ orientated single crystal tungsten under uniaxial tension at 293 K (a) and 673 K (b).

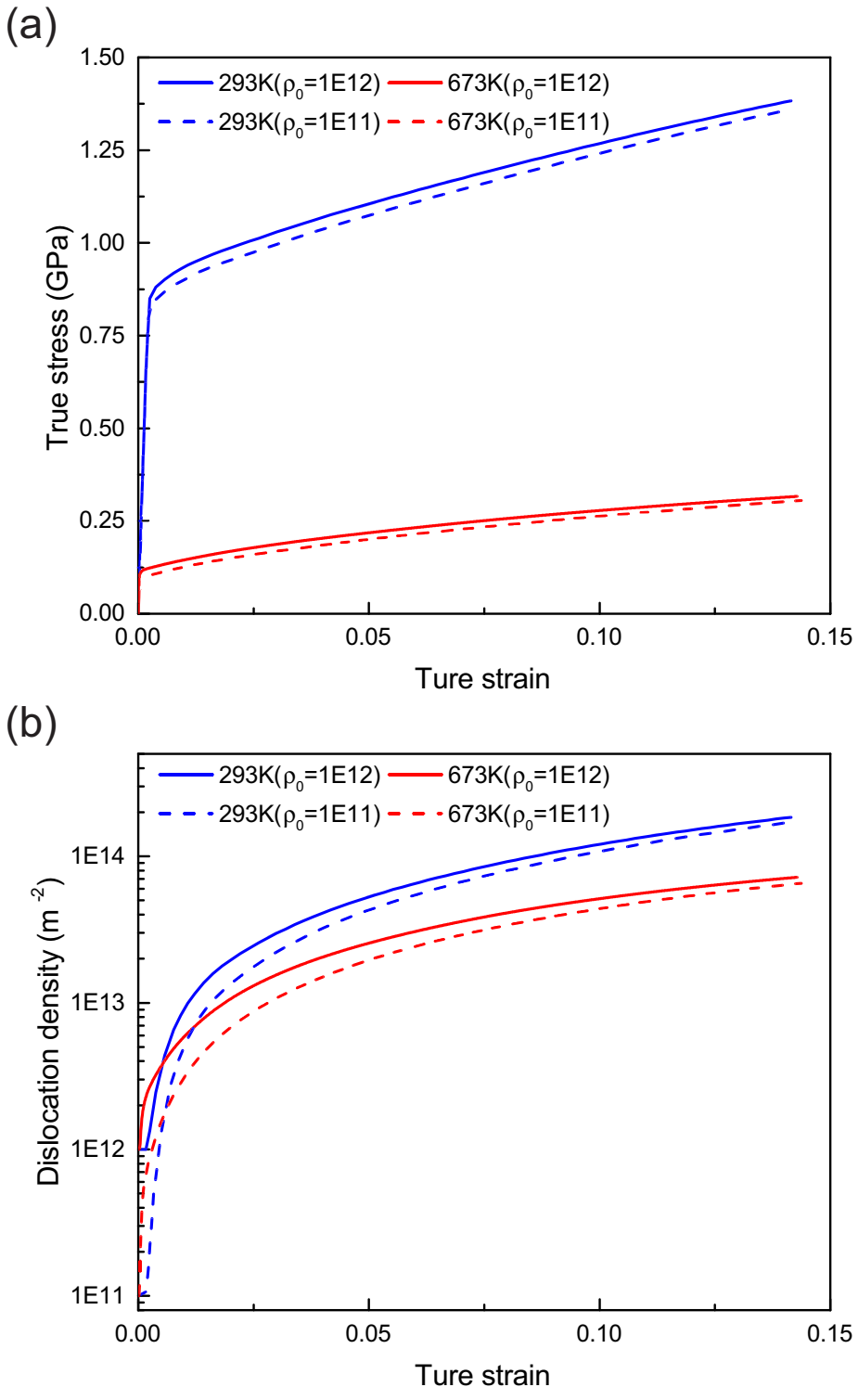

Figure 4.10: The true stress-strain responses (a) and dislocation density evolution (b) of a [001]-oriented single crystal tungsten at different temperatures with a constant strain rate of $1 \times 10^{-3}\,\mathrm{s}^{-1}$.

4.4.4 Estimation of Cohesive Zone Parameters for Grain Boundary

Utilizing the cohesive zone formulations generally requires calibrating the parameters inside the model with dedicated experiments. Mohammed and Liechti [200] utilized four-point bending tests to characterize the brittle adhesive interface of epoxy-aluminum. Yang et al. [201] carried out peeling tests on adhesively-bonded metal joints and calibrated the parameters inside a trapezoidal shape CZM in order to study mixed-mode fracture of plastically deformed adhesive joints. Li et al. [180] used cruciform and micro-droplet tests to calibrate and validate the parameters in PPR and bilinear CZMs in S-glass fiber reinforced epoxy-matrix composites to study its damage evolution. This approach generally gives promising results but the experimentation involves significant efforts.

However, experimental quantification is accessible when the interfaces and materials can be processed into a well-defined geometry. Alternatively, atomistic simulations have also been used to parametrize the traction-separation relationships of the interfaces of various materials, for example, graphene–polymer [202], aluminum-silicon carbide [203], and slica-glycidoxypropyltrimethoxy silane (GPS)[204]. For metals, Yamakov et al. [205] used MD to extract cohesive zone representations of intergranular fracture in FCC aluminum; Zhou et al. [206] and Lloyd et al. [207] also attempted this atomistic-to-continuum approach. It offers great flexibility in fitting CZM pa-

rameters under mix-mode conditions, however, it has not been proven that a strategy that relies on atomistic simulations exclusively is able to predict fractures in bulk metallic samples. This could be partially attributed to the spatial and temporal resolution of atomistic simulations, which it is not able to fully capture the non-local multi-scale failure mechanisms in metals.

Experimental characterization of grain boundary traction-separation relationships generally gives better estimations; however, may be limited to specific kinds of microstructures. Wei and Anand [208] developed an ad-hoc CZM for GB of nanocrystalline nickel and calibrated the model using uniaxial tension experiments. However, this approach is only limited to the nanocrystalline materials in which only grain boundary mechanisms - sliding and separation - are activated and each grain only deformed elastically. More recently, Kupka et al. [209] utilized micro-mechanical experiments and CPFEM simulations to parametrize the material and grain boundary properties in an aluminum lithium alloy. In their work, micro-compression tests were used to fit material parameters in a crystal plasticity model; micro-cantilevers with a pre-notch at the GB was used to create stress concentrations and to trigger intergranular fracture. At the end, the grain traction-separation law was identified by back fitting micro-bending simulations with different CZM parameters to experiments.

In this work, a similar back fitting approach is used and the set of parameters that yields the best resemblance with the micro-compression experiments are adopted. A bilinear traction-separation law with a maximum nominal stress (MAXS) criterion is

used as shown in Figure 4.11.

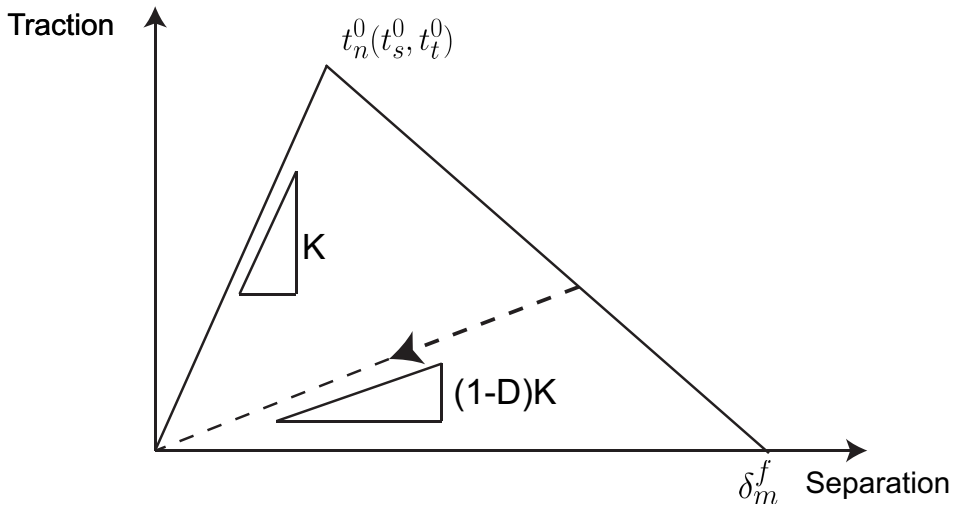

Figure 4.11: Schematic of the bilinear cohesive zone model used in the current work. The damage is initiated at a critical traction value (i.e., t_n^0, t_n^0 or t_n^0), and failure happens at critical separation δ_m^f.

For the initial elastic regime, the traction relates to separation of the cohesive surface and is expressed in uncouple form as

$$\mathbf{t} = \begin{Bmatrix} t_n \\ t_s \\ t_t \end{Bmatrix} = \begin{bmatrix} K_{nn} & 0 & 0 \\ 0 & K_{ss} & 0 \\ 0 & 0 & K_{tt} \end{bmatrix} \begin{Bmatrix} \delta_n \\ \delta_s \\ \delta_t \end{Bmatrix} = \mathbf{K}\boldsymbol{\delta} \tag{4.4.5}$$

where t_n, t_s, and t_t are the normal, and two perpendicular planar tangential components of the traction vector $\mathbf{t}$ of the cohesive surface, δ_n, δ_s, and δ_t the are corresponding components of the separation vector $\boldsymbol{\delta}$. K_{nn}, K_{ss}, and K_{tt} are taken to be

10^6 μN/μm^3; a larger stiffness value leads to the singularities in global stiffness matrix which undermines the convergence rate, while a smaller value introduce excessive compliance into the system. The maximum nominal stress (MAXS) criteria is used such that

$$\max\left\{\frac{\langle t_n\rangle}{t_n^0}, \frac{t_s}{t_s^0}, \frac{t_t}{t_t^0}\right\} = 1 \tag{4.4.6}$$

where t_n^0, t_s^0, and t_t^0 are the cohesive strengths along normal and two perpendicular in-plane direction. The Macaulay bracket, $\langle\rangle$, guarantees that compressive deformation does not lead to the initiation of damage. A normal cohesive strength of $t_n^0 = 200$ MPa is chosen based on micro-bending experiment on beams that fractured at ~ 200 MPa, and two tangential cohesive strengths are assumed to be equal to the normal cohesive strength. The effective displacement δ_m is defined as [210]:

$$\delta_m = \sqrt{\langle\delta_n\rangle^2 + \delta_s^2 + \delta_t^2} \tag{4.4.7}$$

where δ_n, δ_s, δ_t are the separations in the normal and two perpendicular tangential directions, respectively. Again, the Macaulay bracket ensures compressive stress will not contribute to failure of the interface. As the effective displacement reaches a critical value of δ_m^f, the cohesive interface fails. This critical value is set to 5 nm for 293 -573 K, which is equivalent to an energy release rate of $0.5\,\mathrm{J/m^2}$ based on the calculation of the area under the bilinear traction-separation curve. This relatively low energy release rate is rationalized by the pre-existing defects along the grain boundaries. At 673 K, $\delta_m^f = 20$ nm is adopted to account for the brittle-to-ductile transition, which is commonly observed at 573-673 K [111]. This quadrupling of the

critical separation distance or energy release rate is supported by the experimental measurements of CVD-grown tungsten bulk specimen [211]. Finally, a scalar damage variable, D, is defined to provide a measure of damage, such that

$$D(\delta) = \left\langle \frac{\delta_m^f(\delta_{max} - \delta_m^0)}{\delta_{max}(\delta_m^f - \delta_m^0)} \right\rangle \tag{4.4.8}$$

where δ_m^0 is the effective displacement when the damage first initiates, and δ_{max} is the maximum effective displacement that had been reached in the loading history.

4.5 Representative Microstructure and Mesh Generation for Simulation

4.5.1 Quasi-3D Microstructure Generation Using Dream.3D

In this study, 3D microstructures is generated by extruding 2D slices into 3D. There are two main reasons to adopt this treatment. On one hand, both cross-sectional EBSD maps and ion channelling contrast micrographs suggest the grains have straight and vertical boundaries. On the other hand, our post-failure and our *in situ* observations indicates all fractured boundaries are straight. It should be mentioned here there have recently been a few attempts to use statistics derived

from 2D EBSD maps (from top surface and cross-sectional surface) to reconstruct 3D microstructures [212].

Grain size and crystallographic orientation statistics were first extracted from the 2D EBSD IPF on the top surface as discussed in Chapter 2. Then, the Dream.3D software [213] was used for 3D microstructure generation with parameters shown in Figure 4.12. "Mu" and "Sigma" are parameters (μ, σ) defined as parameters for logarithmic normal distribution. A bin size of 0.2 µm was chosen with minimum and maximum cut-off values (i.e., 1 and 2, respectively) in order to exclude very large and small features. The truncation, which is defined with respect to cut-off values, is $e^{\mu - min/max \times \sigma}$, and in this case grains that have an equivalent sphere diameter (ESD) less than 0.498 µm and larger than 4.13 µm will be excluded in the synthetic microstrucure.

Dream.3D stores microstrucutral information on a discretized data grid. Here, a voxel size of 0.1 × 0.025 × 0.025 µm^3 is used to construct a synthetic microstructure having dimensions of 5× 25 × 30 µm^3. This setup offers high in-plane (y-z plane) resolution and enables a good depiction of grain morphology, while keeping the file compact. The final synthetic microstructure is shown in Figure 4.13. Afterward, 2D slices are extraced from the 3D microstructure parallel to y-z plane. At the end, 2D microstructures with an area of 5 × 5 µm^2 are sampled from the 2D slices, the procedure is shown in Figure 4.13.

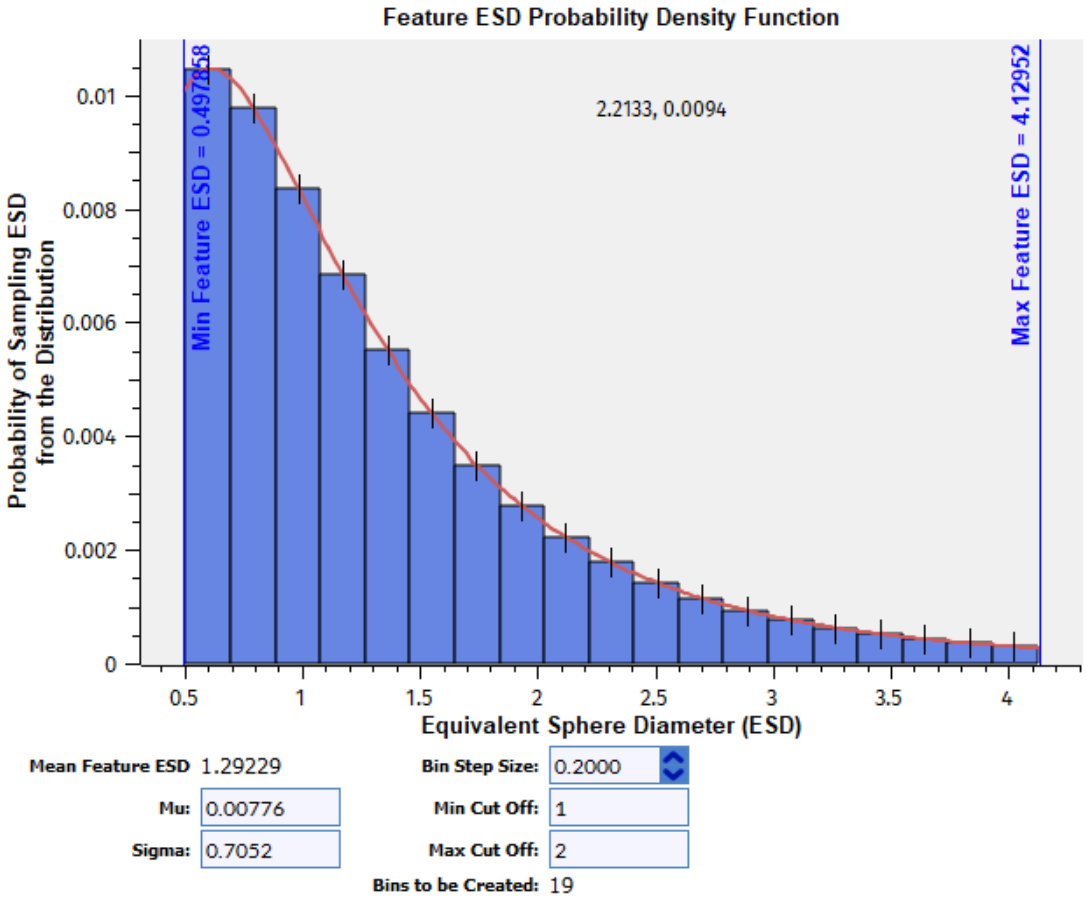

Figure 4.12: Screenshot of Dream.3D GUI to show the input statistics for virtual microstucture synthesis. A bin size of 0.2 µm was used which created 19 bins. Grains with an ESD less than less than 0.498 µm and larger than 4.13 µm are excluded.

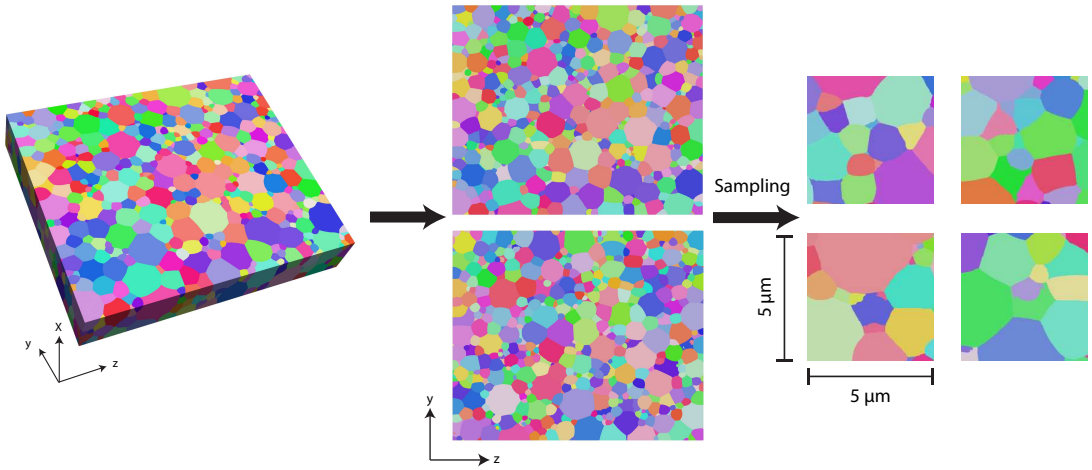

Figure 4.13: Images of synthetic microstructures created using Dream.3D. The initial 3D microstructure shown on the left side has dimensions of 5× 25 × 30 µm^3. Afterward, slices of 2D microstructure were extracted from the 3D microstrucutre. Finally, 5 × 5 µm^2 microstructures are randomly sampled from 2D microstructures.

4.5.2 Mesh Generation and Identification of Grain Boundary

The square 2D microstructures were then postprocessed into circles having diameters of 4.5 µm and converted into the format required by ImageToModel software [214] using a Matlab script. After they were imported, erosion, dilation, and small object filters were applied in order to remove small objects (i.e., small grains and artifacts)in the voxel dataset. Finally, 2D slices were extruded to the desired height followed by a smoothing procedure to guarantee smooth grain boundary morphologies before the mesh generation.

The mesh was generated using SimModeler software developed at Simmetrix Inc. [214]. The geometries were meshed using tetrahedron elements having an edge length no more than 0.2 µm, and mesh refinement was applied based on the criterion of a maximum skewness (i.e., 0.85) to reach a desirable mesh quality. Using these parameters give a total element number of ∼200,000 for each pillar with dimensions of $D = 4.5\,\mu m$, $H = 12\,\mu m$. An example of the meshed geometry is shown in Figure 4.14.

It is reported that linear tetrahedral elements exhibit stiffer response due to volumetric locking, which causes overestimated the local stress that is particularly inappropriate to be used for buckling investigations. It should be mentioned here that Cheng et al. [95] proposed several locking-free tetrahedron-mesh-based formulations that are computationally efficient. Unfortunately, these advanced techniques/ formulations have not been incorporated into Abaqus, so quadratic tetrahedral elements (i.e., C3D10 or TET10) were used in the current study to remedy the volumetric-locking at the cost of a higher computational power.

Finally, grain boundaries were identified on the meshed geometry using a Matlab script developed for this thesis work. The script is able to insert additional nodes at the shared surfaces of two elements in case they belongs to different grains. Moreover, it constructs cohesive surfaces definitions automatically and writes them into the simulation input file.

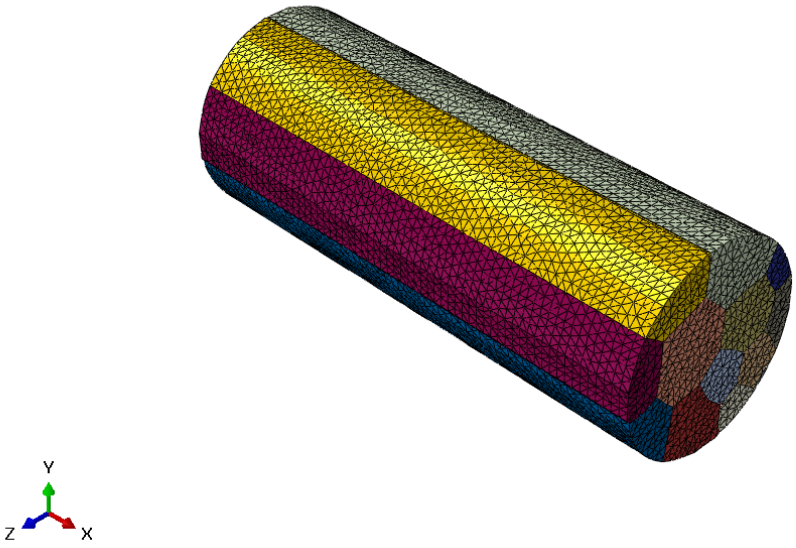

Figure 4.14: Image of a meshed pillar with a dimension of $D = 4.5\,\mu m$, $H = 12\,\mu m$, and a mesh size of 0.2 µm with adaptive refinement to ensure good mesh quality.

4.5.3 Simulation Geometry and Setup

Three pillars (i.e., P1, P2 and P3) with different microstructures were selected for the simulations to investigate the effect of local microstructures where P1 has columnar grains with similar sizes, while P2 has a single grain that is much larger in size than the others, as shown in Figure 4.15. Regarding the texture, 3 different sets of crystallographic orientations were randomly generated for each of the microstructures. It should be mentioned here, the cut-off effect on the exterior grains is also considered when appllying the Hall-Petch effect, and when in-plane grain size is less than 0.65 µm (i.e., half of the average in-plane grain size), an in-plane grain size of

0.65 µm is assumed to avoid the stress singularity raised due to the extra small grains. Assuming each columnar grain is an ellipsoid, the equivalent spherical grain diameter is computed as

$$d_{ESD} = \sqrt[3]{12}\ \sqrt{\frac{4A}{\pi}} \tag{4.5.1}$$

where A is the in-plane area of each grain measured from the 2D microstructure.

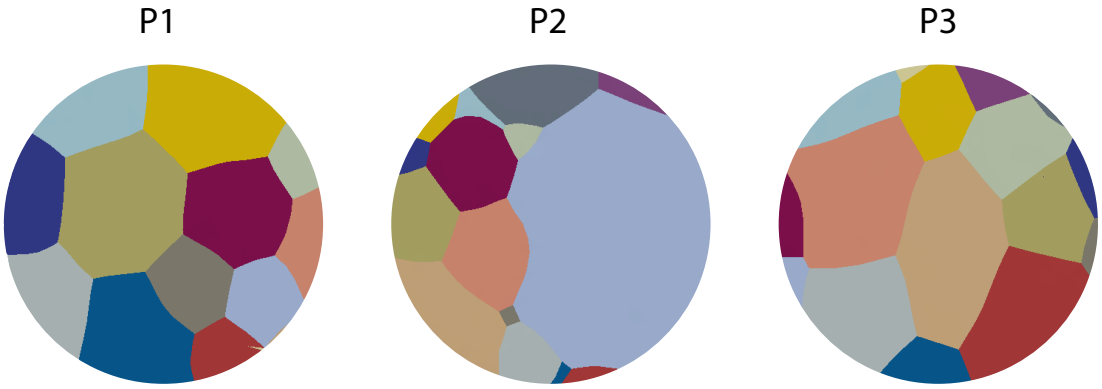

Figure 4.15: Top view of the microstructures of the pillars used in the simulations that have z diameter of 4.5 µm in the simulation. Three different sets of crystallographic orientations are randomly generated for each of the pillar.

To mimic the experimental setup, a diamond flat punch was also included in the simulation and the bottom of the pillar is fixed (i.e., X=Y=Z=0) as shown in Figure 4.16. The punch has a surface area of 9 × 9 µm^2 and a thickness of 1 µm. The diamond punch is treated as an isotropic elastic material having an elastic modulus E = 1200 GPa and a Poisson's ratio ν = 0.2 [215]. The bottom surface of the punch and the top surface of the pillar is aligned with their centers coincided at the

beginning of the simulation. Moreoever, the contact in-between is defined as "Surface-to-surface" formulation (which gives significant better accuracy than "Surface-to-node" formulation) and is tracked using "Small-sliding" algorithm in Abaqus. The Coulomb model with a coefficient of 0.03 was used to account the friction between the punch and the pillar [216]. Simulations with higher coefficients (i.e., 0.1, 0.2, 0.3) do not result in noticeable changes in stress-strain response. In addition, take advantage of the surface-based cohesive behavior definition, a "hard" contact with zero friction are used for modeling the interaction of the grains after GB failure.

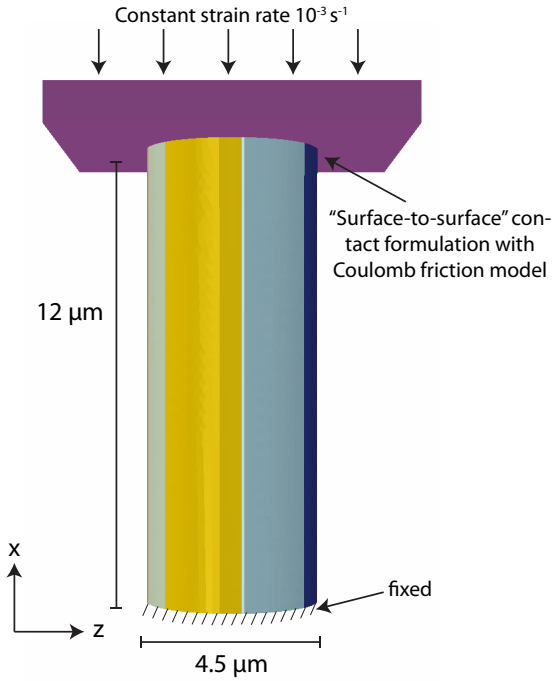

Figure 4.16: Schematic of the simulation geometry. The pillar size is $D = 4.5\,\mu m$, $H = 12\,\mu m$ with a fixed bottom end and a diamond punch in contact with the top surface.

Quasi-static simulations are usually carried out through the "General, Static"

procedure in Abaqus where the mass matrix or inertia effect is not included. However, it is commonly observed that "General, Static" simulations terminated due to non-convergence when the simulation is strongly nonlinear (e.g., contact) or local instabilities emerge (e.g., buckling). Stabilization schemes based on introducing extra viscosity may not remedy the issue and may distort the solution. To address these issues, the "Dynamic, Implicit" procedure with "Quasi-static" application type was used in the current work. It should be noted here that the Abaqus "Dynamic, Implicit" procedure has three application types with different level of energy dissipation, and they are "Transient fidelity", "Moderate dissipation", and "Quasi-static". The "Quasi-static" type gives larger energy dissipation than the other two, and the inertia effects are introduced to regularize the unstable behavior (e.g., buckling). From the numerical perspective, the fundamental difference is that "Quasi-static" enforces a backward Euler time integration scheme while the other two using Hilber-Hughes-Taylor time integration. As this procedure uses the Abaqus/Standard solver, the UMAT used in "General, Static" procedure can be directly adopted without any modifications except the density of each materials need to be specified in order to form a mass matrix. In our simulations, densities of 19.3 g/cm^3 and 3.51 g/cm^3 were applied to W and diamond, respectively.

All simulations were performed using at a constant engineering strain rate of 10^{-3} s^{-1} by applying a constant displacement rate on top of the punch, where the lateral displacements were set to zero. The engineering stress is calculated by dividing the

reaction force of the punch to the top surface area of the pillar before deformation. All simulations and visualizations were conducted commercial FEM software Abaqus 2016 [217].

4.6 Simulation Results and Discussions

Utilizing the above developed framework, a series of CPFEM simulations were performed to study the effects of temperature, texture, microstructure, etc. on the mechanical response of the micropillars. The numerical results and discussion are presented in this section. It should be noted that no special calibration is performed specifically for the W coating before simulation, and parameters are adopted from polycrystalline tungsten studies that exist in literatures, which may not be a perfect description of the CVD grown tungsten. So the goal of the current work is not to pursue a one-to-one matching of our experiments, but instead, to better understanding the roles of multiple underlying mechanisms to help in the process of contributes to future design of such coatings.

4.6.1 The Effect of Temperature

Our experiments indicate, among multiple factors, temperature plays the dominant role in the defromation mode in the micro-architectured W. It was rationalized that that increase of temperature lowers the lattice friction and provides extra amount

of plasticity, and thus results, in an improved defect tolerance compatibility at a cost of strength. Here, numerical results provides a quantitative analysis of this process so it can be better understood.

The engineering stress-strain curves from simulations and experiments are shown in Figure 4.17. The simulation results are from microstructure P1, and only part of the experimental results are shown for clearness (one at each temperature). It is shown that the simulations give a good prediction on the yield strength at different temperatures: at 293 K, both the simulation and experiments shows a yield strength around 1.6 GPa; at 673 K, both give around 750 MPa yield strength. Among all testing temperatures, only the 423 K simulation gives a higher predication around 200 MPa, which could be partially attributed to the overestimation of lattice friction (see Figure 4.6) that the fitted curve yields a slightly higher prediction than the experimental measurement at 400 - 500 K. At 423 K, the predicted lattice friction is about ∼35 MPa higher than that of experimental measurement, which is converted to ∼78 MPa flow stress (by using a Taylor factor of 2.25).

For the initial linear regime of simulation, the slope gives a Young's modulus of ∼380 GPa, which perfectly matches the theoretical value of polycrystalline W and is consistent with our input material parameters. This is attributed to the ideal scenario where there is perfect alignment between the punch and pillar top surface and an absence of any defects/void in the simulation volume. These idealized conditions would not be possible in experiments for a few reason. For one thing, microstructural

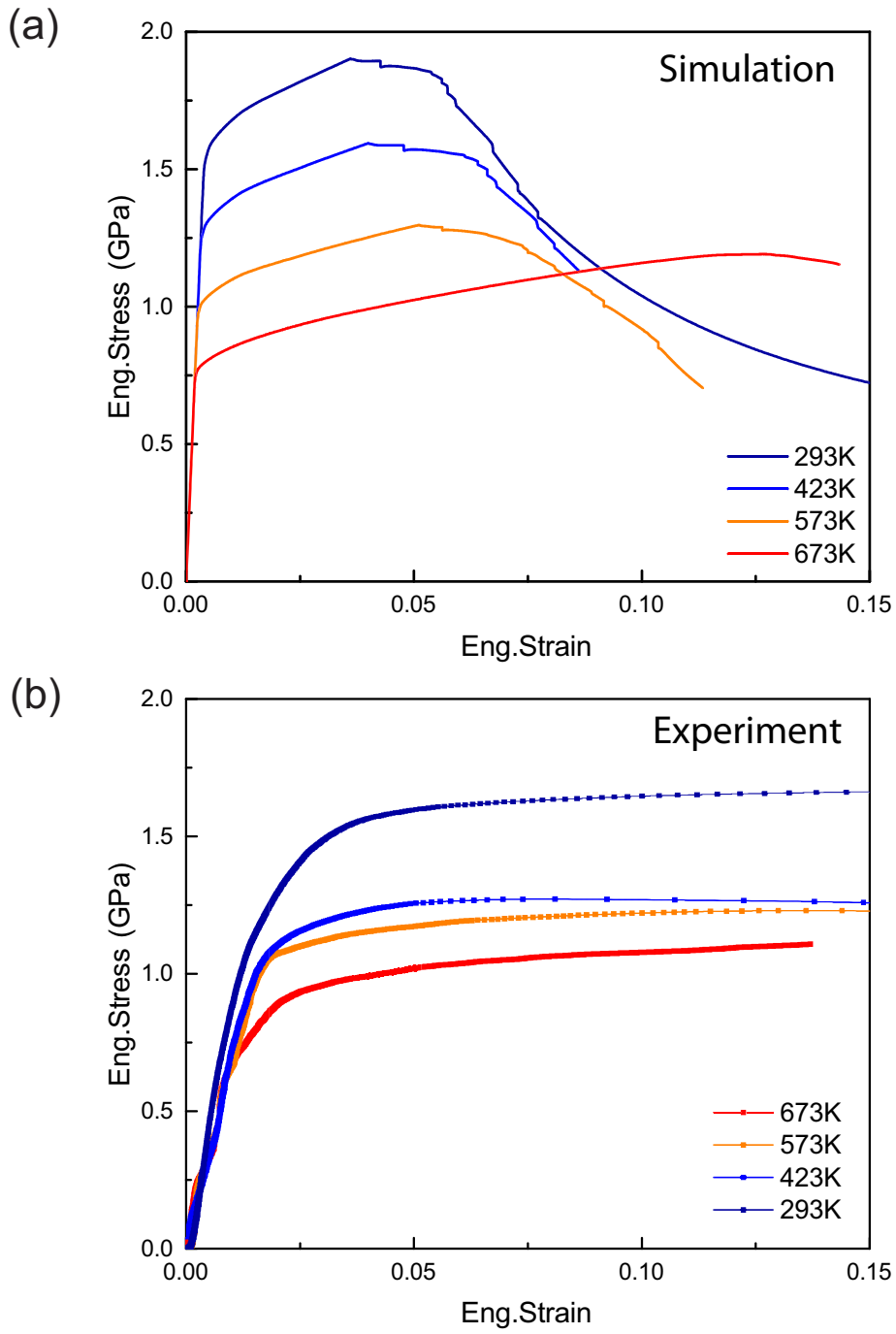

Figure 4.17: Engineering stress-strain responses of micro-compression experiments from both (a) simulations and (b) experiments conducted at 293-673 K. Numerical results are from synthetic microstructure P1 with texture T1; for experimental results, only one at each temperature is shown.

characterization in Chapter 2 indicates that the material has a large amount voids and thus the modulus is expected to be lower than condensed counterpart. Moreover, these voids as well as other defects beneath the pillar can increase the base compliance of the pillar which could not be fully corrected by Sneddon's formula in Equation 2.5.9. Lastly, the alignment and contact between the pillar top surface and punch are less likely to be perfect in the real world due to slight tilt angles and surface roughness [218]. All of these effects could be studies in our simulation, the first two effects could be incorporated into simulation by incorporating a porous based material, and the last one can be considered by small rotations of the punch angle.

Regarding the post-yielding behavior, the hardening rate of the simulation is generally higher than seen in the experiments, and this is partially attributed to the extra compliance and voids in the real material. It should be mentioned there that the displacement-controlled method was used for simulation which allow the stress relaxation whereas the load-controlled method was used for experiments in which failure will manifest as strain-bursts. It is shown that the first load drop is observed at 3.5% of engineering strain for 293 K and gradually increases to 5% at 573 K due to the enhanced plasticity at higher a temperature. Beyond this point, a plateau shows up before the observation of significant stress drops at 5.5% to 8.5% strain depend on temperature. This is in qualitative agreement with the experimental observation that the strain burst or plateau occurs somewhere between 5% to 10% strain at 293 - 573 K. At 673 K, the simulations successfully capture the experimentally observed

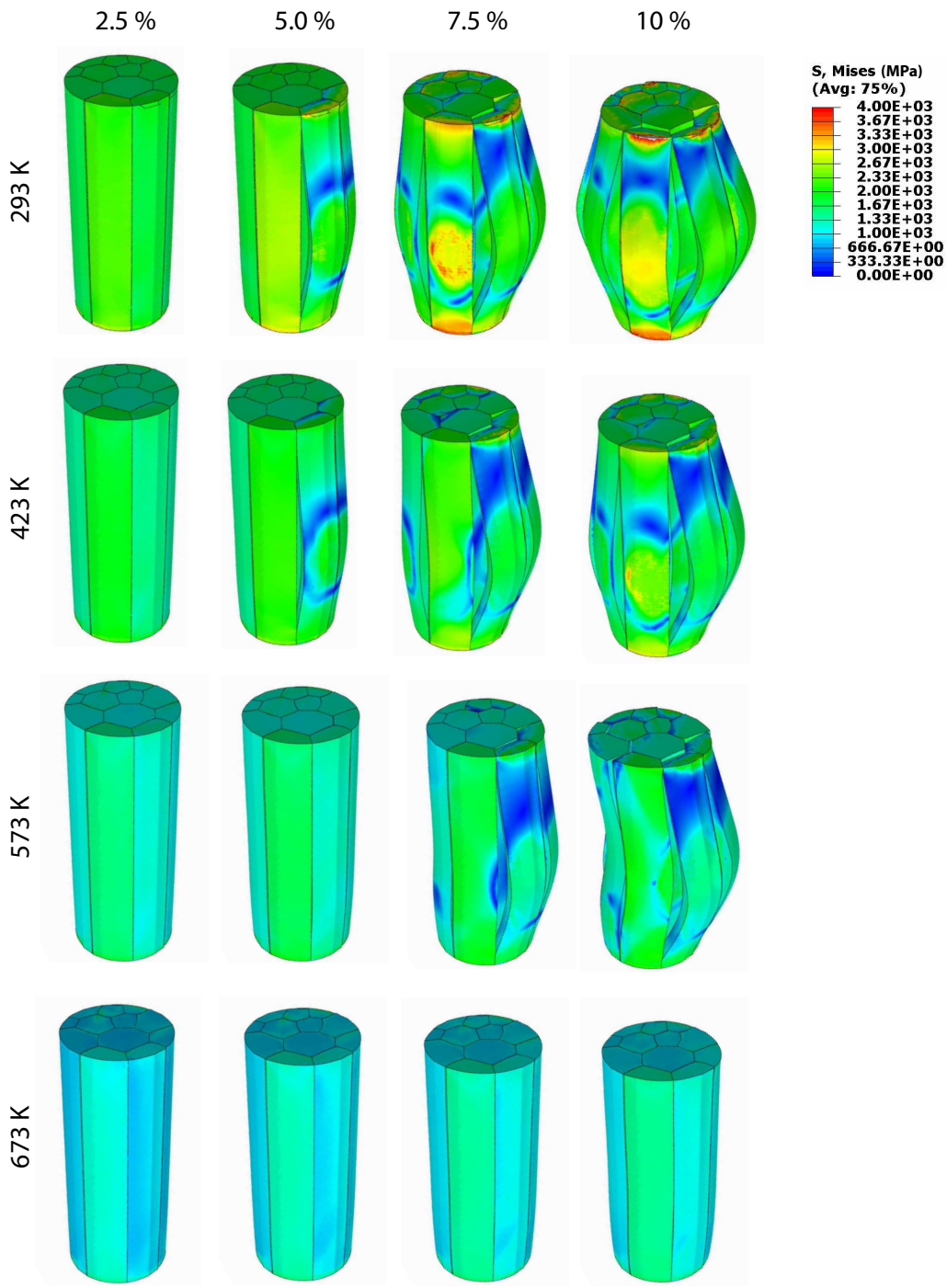

Figure 4.18: Deformation morphologies of pillar P1 with texture T1 at different temperatures and strain levels. The punch at the top of the pillar is excluded for better visualization. The stress concentration for 293 K at 7.5% and 10% comes from the contact of sharp pillar edge contacting the punch.

continuous hardening behavior which continues to a very high level of strain without softening but at a lower rate. The *in situ* snapshots (c.f., Figure 3.12) show the formation of a localized shear zone, which could reduced the overall hardening rate reflected in the engineering stress-stain response. The pre-existing voids, which are not explicitly incorporated in the simulation geometry will also lead to localized deformation and reduce the overall hardening. It should be noted that as the hardening parameters were adopted from a dense polycrystalline W which exhibits stronger hardening rate than the W coating with voids at GB.

Regarding crack nucleation and propagation, the simulations offer full-field tracking capabilities that is more informative than surface observations in the experiments, and ratio of fractured GB with the evolution of engineering strain is shown in Figure 4.19(b). In addition, deformation morphologies at different strain levels are shown in Figure 4.18. It is shown that the onset of fracture occurs after yield at 1% of strain and then propagates rapidly. Under such small strains, the pillar deforms uniformly without barreling and the stress state remains unixial. However, the crystallographic orientation and grain size variation leads to different stress levels in the iso-strained columnar grains. This suggests that the grain boundary failure is initiated and promoted due to the anisotropic deformation of grains across the grain boundary. To verify the hypothesis, a micro-compression simulation on the [001]-textured sample (i.e., all grains has [001] orientation) on the same microstructure was carried out. Upon doing so, no GB fracture is observed within 5 % strain. If the Hall-Petch effect

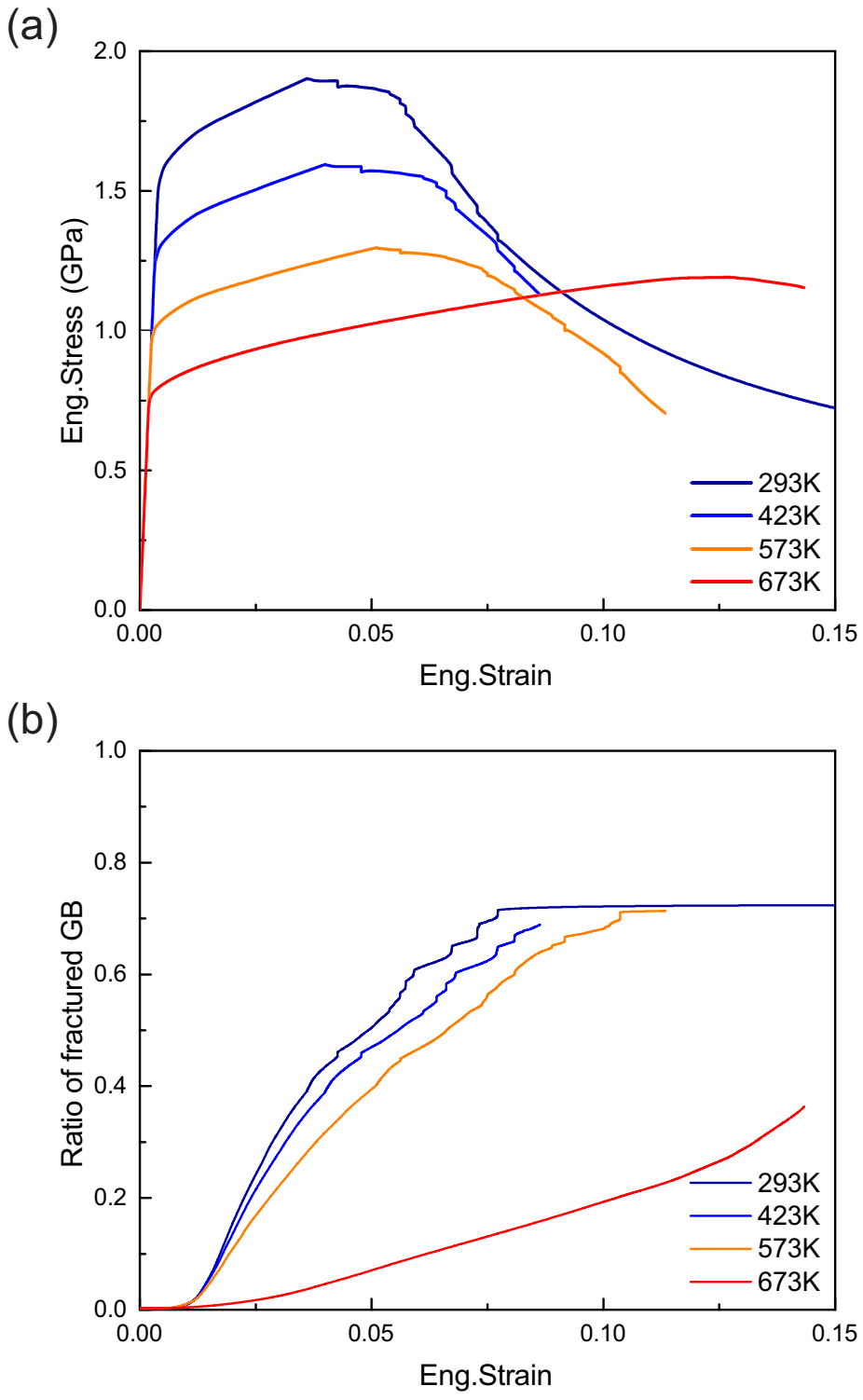

Figure 4.19: (a) Engineering stress-strain responses and (a) ratio of fractured GB with respect to total GB area during loading.

is applied in an average sense (a.k.a, assume all grains have the same in-plane grain size), the onset of fracture happens at a even larger strain (more than 10 %). As shown in Figure 4.19(b), with strain reaches At 5% strain, 50%, 46%, and 39% is failed for 293 K, 423 K, 573 K simulations, and the pillars already exhibited barrel shape (see Figure 4.18)which indicates the crack propagation is promoted by normal stress/separation instead of shear stress. For the 673 K, the more ductile grain boundary along with increase in plasticity in each grain significantly slows down the fracture propagation as shown in Figure 4.19(b). The pillar is able to sustain up to $\sim$ 13 % of engineering strain without exhibiting a load drop.

This observation is also supported by the deformation morphology as shown in Figure 4.18. At 2.5 % strain, the pillar undergoes uniform deformation at all temperatures. This is clear from the uniform stress contours in each grain and the observed slight stress variation in different grains is due to the crystallographic orientation, but no local GB decohesion is observed on the surfaces. At 5% strain, it is observed that two grains at the circumference have already bowed out due to the high aspect ratio and free lateral motion, which is an effect only seen at 293 K and 423 K. In contrast, for higher temperatures, the pillar is still maintains their structural integrity upon deformation. With an increase in strain level, at 7.5% strain, noticeable intergranular crack are observed at 573 K ; meanwhile, for the lower temperature case, more and more columnar grains start to buckle and fracture along grain boundaries. At 10% strain, intergranular fracture is predominant at 293 K-573 K cases, while no notice-

able cracks are observed for 673 K which is similar to our *in situ* experiments (see Figure 3.12). It should be pointed out that the temperature difference also leads to a different final deformation morphology of the pillar as shown for 293 K and 573 K at 10% strain. Nevertheless, since the strain level is moderate, no fractured grains are able to overcome the friction with punch, and thus the buckling mode is limited to the first mode with periodicity of 12 µm.

4.6.2 The Effect of Texture

As previously indicated, the texture or crystallographic orientation of each columnar grain will affect both the strength and fracture of the coating. To characterize this, a systematic study is carried out in this section. Three different sets (namely, T1, T2, and T3) of crystallographic orientations are randomly generated and assigned to microstructure P1 for simulations, and the resulting stress-strain responses at 293 K and 673 K are shown in Figure 4.20. The flow stresses at 1% and 2.5% of engineering stress are listed in Table 4.6. Among threes randomly generated textures, there is a 131 MPa variation in flow stress (at 1% strain) observed at 293 K, which decreases to 86 MPa for 673 K which also partially explains the reduced scattering at elevated temperatures seen in our experiments.

Regarding the effect on crack nucleation and propagation, it is shown that texture T2 and T3 yield higher flow stresses and thus lead to earlier crack nucleation and propagation as shown in Figurer 4.20(b). It should be noted that texture T2 gives

Table 4.6: Effect of crystallographic texture on the flow stress (at 1% and 2.5% engineering strain) at 293 K and 673 K.

T (K)	Texture-1 (MPa)	Texture-2 (MPa)	Texture-3 (MPa)	Mean (MPa)	Variation (MPa)
293	1678	1722	1809	1736	131
	1818	1874	1976	1889	158
673	852	887	938	892	86
	933	971	1028	977	95

the highest flow stress, however, which also helps to promote fracture. At 673 K, the flow stress start to decrease at ∼8 % strain. Close examination of the model shows that two neighboring grains have a magnified difference in stress state that originates from crystallographic orientation variation, and leads to earlier crack nucleation. In addition, these two grains are located at the circumference without side constraints which results in easier buckling and crack propagation. This suggests, for the small volumes tested that have only ∼ 10 grains, the texture effect can not be ignored and its randomly in small volumes will contribute to scatter in experimental measurements.

4.6.3 The Effect of Microstructure

For the buckling problem, it is suggested the slenderness ratio is an indicator of the susceptibility of a column to buckling. In the previous section, the simulations

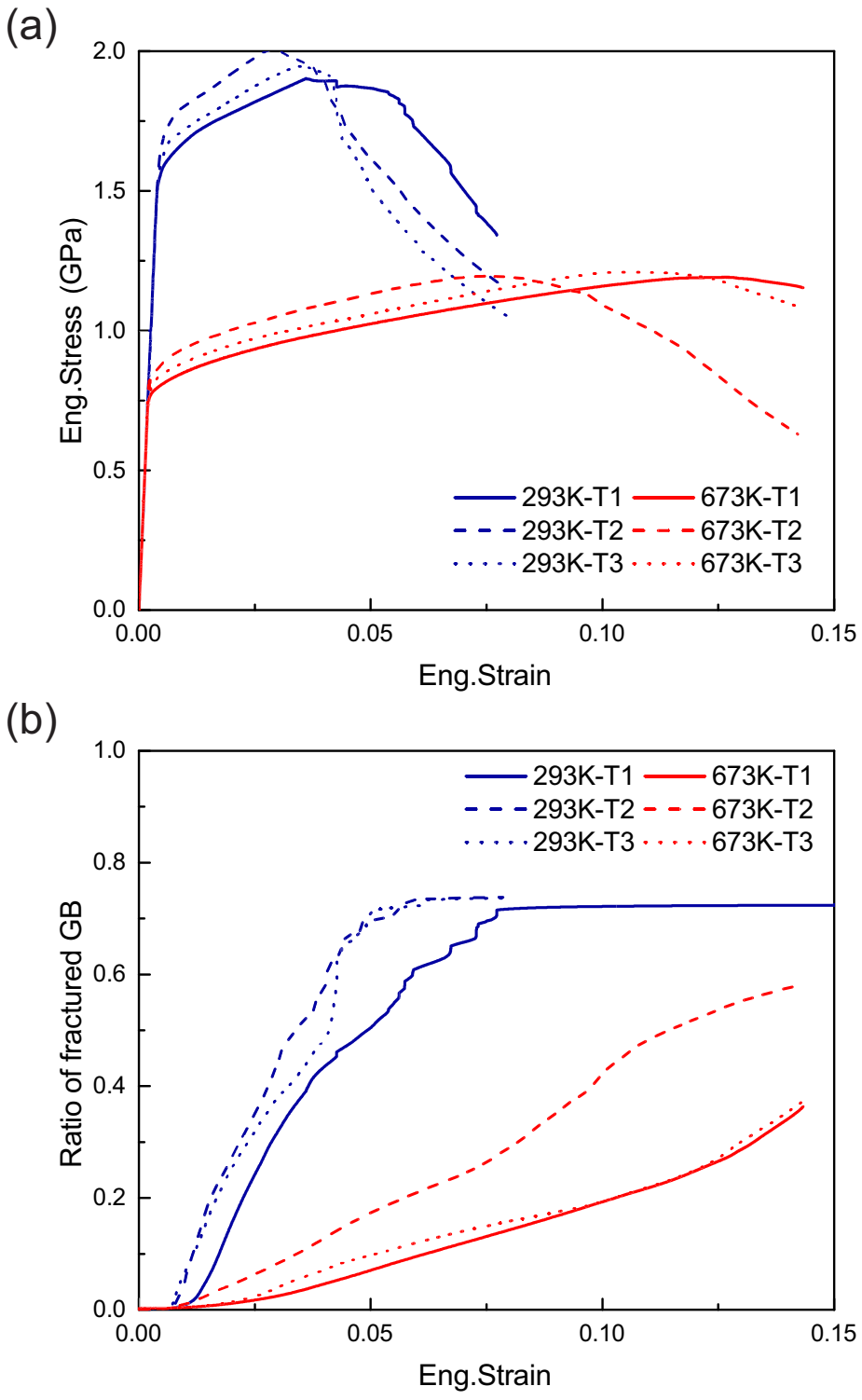

Figure 4.20: Engineering stress-strain responses of microcompression simulations with microstructure P1 and three different crystallographic textures.

were carried out on a microstructure having similar in-plane grain sizes. However, for the coating being studied here, the in-plane grain size follows the a logarithmic normal distribution which implies the slenderness of each columnar grain could vary dramatically. Considering that the micropillar we tested are comprised of only a few grains with a large surface to volume ratio, the effect grain size scatter deserves more detailed study. Moreover, along with variation of the in-plane grain size, the strength of each grain will also change accordingly following a the Hall-Petch relationship. Thus, it is critical to investigate the effect of microstructure on the deformation of such a coating.

For this purpose, simulations on microstrcture P2, which is comprised of a large grain a few small grains were carried out. The stress-strain curves and deformation morphology at different strain levels are shown in Figures 4.21 and 4.22, respectively. The stress-strain curves from microstructure P1 and texture T1 are also included for comparison. It is shown that the flow stress (at 1% strain) is 130 MPa lower at 293 K and 104 MPa at 673 K which is attributed to the Hall-Petch effect. Based on the rule of mixture, grain with larger size will contribute to a larger fraction of the flow stress and the increased grain size will reduce the CRSS, thus doubling its effects. It should be noted here the difference in flow stress does not exclude the effect of crystallographic orientation difference as they are randomly assigned. However, this difference is a conservative value as it is the lowest one in the Table 4.6. If the highest one in Table 4.6 is used, the difference will reach 231 MPa.

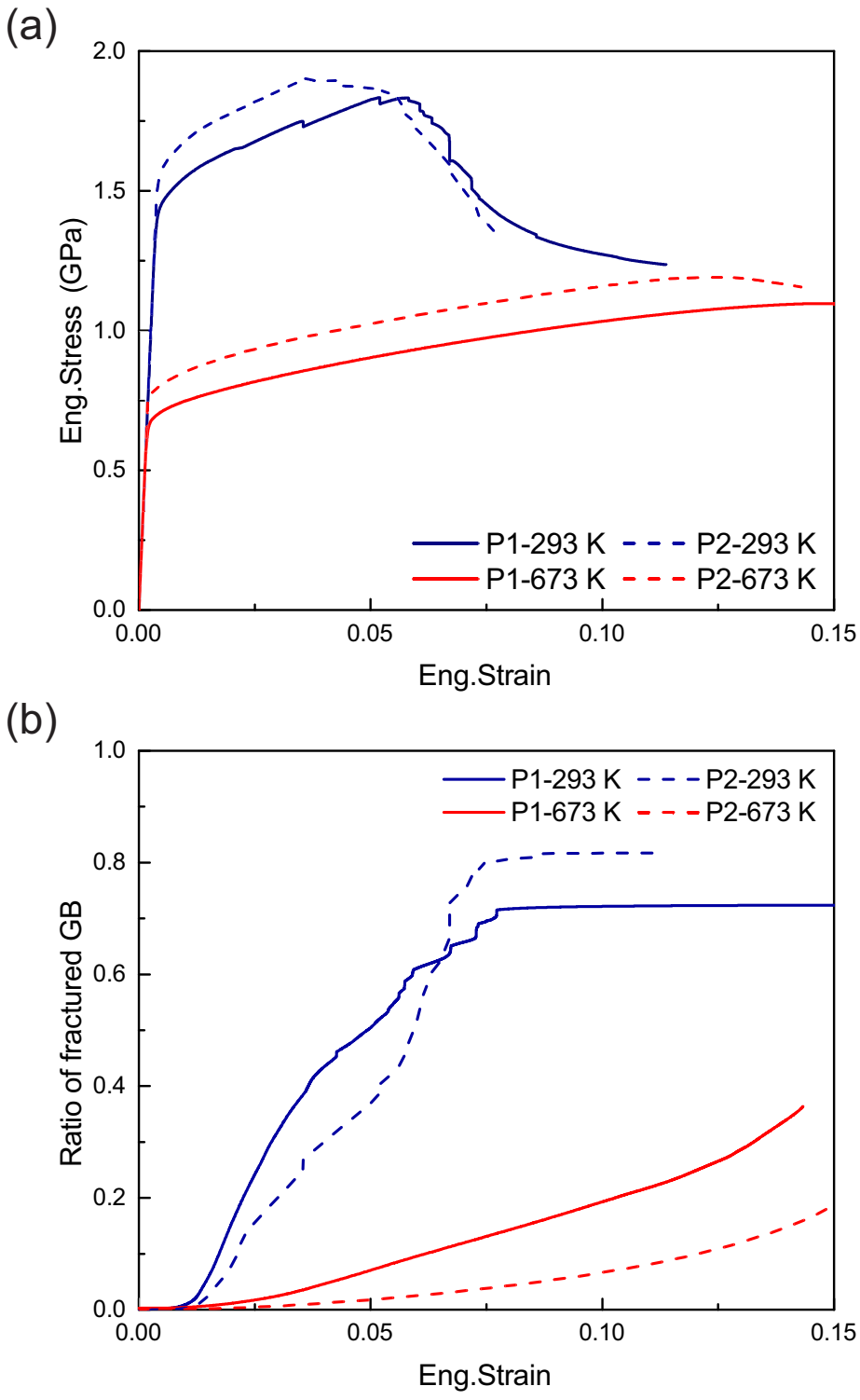

Figure 4.21: (a) True stress-strain responses and (b) GB fracture evolution.

It is shown in Figure 4.21(b), the reduced slenderness and the associated lower flow stress has little effect in delaying crack nucleation but doest retard its propagation. This may attributed to two possible explanations: (1) larger grain size scattering introduces large stress incompatibilities at the grain boundaries which promote the cohesive damage initiation; (2) as shown in Figure 4.22, the grain with the largest size has more resistance to buckling, however, other smaller grains start to show an "S" shape at an early stage of deformation. At 673 K, it is shown that fracture propagation becomes much slower as compared to that of microstructure P1, and at 15 % engineering strain, less than 20 % of grain boundaries are failure. In Figure 4.22, GB delamination is observed on the surface of the pillar.

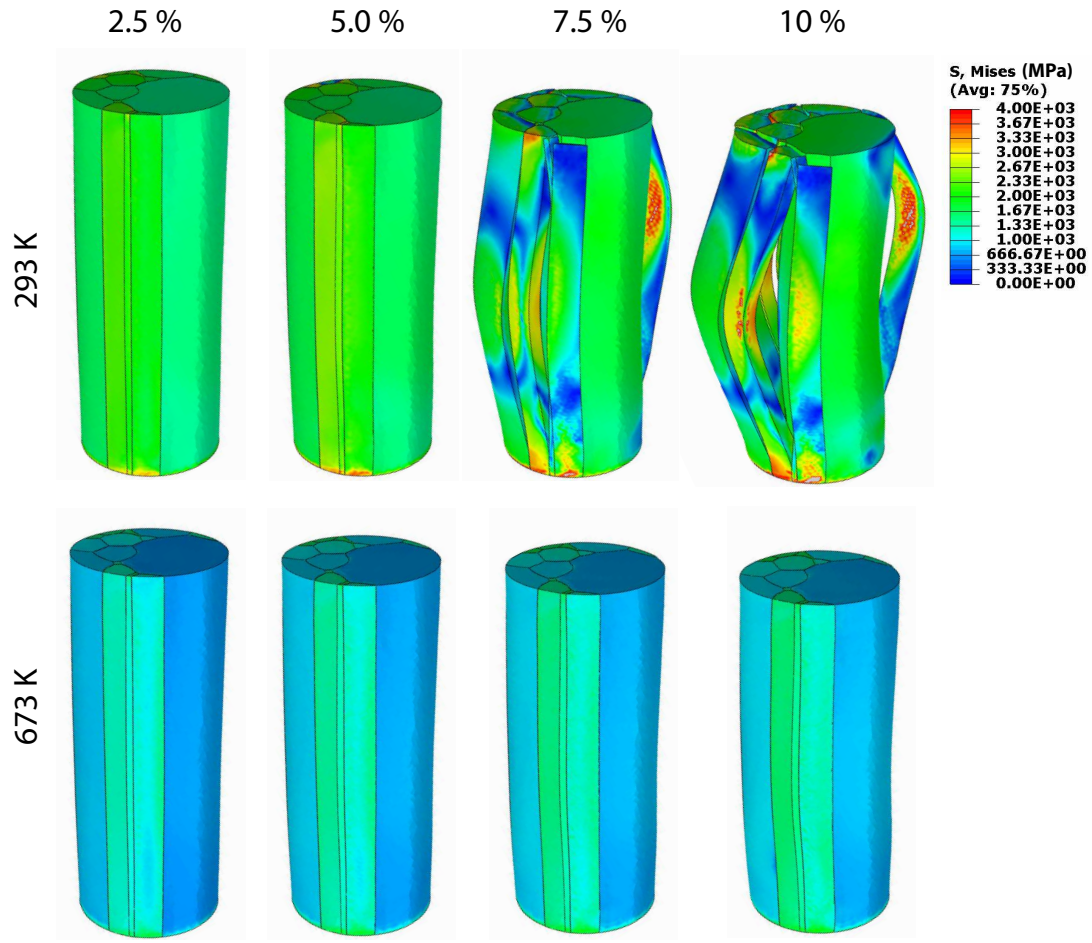

Figure 4.22: Deformation morphologies of pillar P2 at 293 K and 673 K at different engineering strain levels. The punch at the top of the pillar is excluded for better visualization.

4.6.4 Discussion on the Limitations of Current CPFEM Formulations and CZM

In this chapter, the effects of crystallographic orientation and microstructure on the engineering stress-strain responses were discussed, and they were shown to have a major contribution to the observed scattering in the experiments. At room tem-

perature, a variation of crystallographic orientation leads to a $\sim$ 150 MPa flow stress different(at 1% and 2.5% engineering strain as shown in Table 4.6). Furthermore, by changing the microstructure another $\sim$ 150 MPa flow stress variation is observed (as shown in Figure 4.21(a)). These observations indicate the variation in response is an inherent property of the small specimens, which contains only $\sim$ 10 grains, thus a one-to-one matching between experiment and simulation is not possible unless the identical microstructure is used in the simulation as that in the experiments. This could also be rationalized by the concept of property-based statistically equivalent representative volume element (P-SERVE) [212, 219], which indicates a converged material response is only achieved when a larges enough SERVE is used. For those simulations having less grains, increasing amount of scattering are commonly observed as shown by Pinz et al. [220]. On the other hand, from the perspective of calibration, the parameters used in current study is derived from dense polycrystalline tungsten "spherical" grains, and a small adjustment of Hall-Petch coefficient may be needed for the W coating in order to resemble the stress-strain responses in the current experiments. Nevertheless, it will not change the observed deformation modes.

Regarding modeling of the intergranular fracture using CZM, it should be pointed out that three major assumptions were made in the current study. First of all, the voids distributed along GBs are not directly accounted for in the simulations. Instead, they are treated as part of the interface. This treatment helps mitigate the enormous total number of elements that would be required to properly mesh those very small

void features along the grain boundaries. On the other hand, considering the focus of the current study is on the structural response of the micropillars, the major effect of these voids is to weaken the GB, thus, it could be appropriately captured through a modified GB constitutive relationship.

Secondly, a uniform distribution of GB property is assumed in this study, which is due to the inaccessibility to a full 3D high resolution microstructure information of the void distribution in the microstructure. In the future, once such data is available, the distribution of the pre-existing voids could be investigated and its effect can be incorporated into the simulation through a variation of CZM parameters.

At the end, it should be mentioned that there is certain amount of space to improve the current CZM to study the fracture. In the above simulations, damage initiation stress along normal direction is chosen based on the micro-cantilever deflection experiment, whereas damage initiation stresses along two shear directions were assigned a same value as to the normal direction. This assumption works well because the mode I fracture dominates, however, for more complex loading conditions, they should be determined through experimentation. Beyond the above improvements on current triangle-shaped CZM, on the other hand, a more sophisticated CZM might need to be developed to better represent the constitutive response of the GBs in the W coating.

4.7 Summary of the Image-based CPFEM simulations

An image-based CPFEM framework is presented and utilized to investigate the thermo-mechanical responses of the W micro-architectured tungsten coating. The chapter starts with a finite deformation crystal plasticity model, which is based on the kink-pair mechanism and Taylor hardening law, followed by the detailed illustration of its numerical implementation into Abaqus/UMAT. Then, the procedure of Quasi-3D microstructure generation is discussed, which is achieved by extruding 2D microstructure created using the grain size statistics obtained from the EBSD IPFs presented in Chapter 2. A cohesive zone model is incorporated to mimic the constitutive response of the porous grain boundaries in the coating with parameters that were estimated from the micro-mechanical characterization. CPFEM simulations of micro-compression experiments are systematically conducted at various temperatures with different crystallographic textures and microstructures. The simulations show good agreement with our experimental observations, including the mechanical strength, post-yielding response, and failure mode. Thus, they were used to elaborate the interplay between temperature and fracture of the W coating. Moreover, it is believed that the observed scatter in flow stress is primarily attributable to the crystallographic differences among the tested micropillars. Finally, this suggests a

stronger crystallographic texture could help to suppress of the brittle failure at low temperatures.

Chapter 5

Concluding Remarks and Suggested Future Directions

5.1 Summary of Research

The experimental and computational results presented in this thesis offers an in-depth understanding regarding the microstructure and thermo-mechanical properties of the micro-architectured W coating. The key results and findings are summarized here.

The microstructural analysis reveals that the coating is multi-layered and each individual micro-pattern is composed of columnar grains with an mean in-plane diameter of $\sim$1 µm as measured from the top surface. In addition, large number of pre-existing voids are presented at grain boundaries, which are introduced by the con-

trolling the CVD process parameters to alleviate thermal stress buildup during thermal cyclic loading of the coatings by allowing free expansion. At room temperature, by means of microcompression experiments of different micropillar sizes fabricated into the coating, a size-dependent response and transition in deformation modes is observed. Smaller micropillars show a higher strength and large strain burst followed by catastrophic failure governed by intergranular fracture assisted plastic buckling of the limited number of grains that comprise the microcrystal. Larger micropillars also show intergranular fracture, however, they exhibit a continuous hardening response, which is attributed to the restriction in the lateral movement of the columnar grains by other grains in the specimen.

In addition, the thermo-mechanical response is characterized using high temperature *in situ* scanning electron microscopy (SEM) microcompression experiments. The material exhibits a strong temperature dependence in the stress-strain response and deformation mode. The low temperature intergranular fracture and buckling of individual columnar grains is observed to be gradually suppressed with increasing temperature due to the enhanced plasticity. In addition, the catastrophic failure shortly after the onset of yield is shown to transition to steady hardening with further straining. A physics-based model is also proposed to predict the strength of the coating that takes into account for the effect of testing temperature and grain size. Our experiment indicates these micro-architectured coatings demonstrates a great combination of excellent strength, reduced internal thermal stress, and dramatically

improved defect tolerance capability.

Finally, Image-based CPFEM simulations of the thermo-mechanical response of the W coatings were carried out to examine the experimentally observed temperature-dependent deformation mode transition. The simulations successfully capture the stress-strain responses, deformation behaviors reported in our micro-mechanical experiments. Moreover, the effect of temperature, crystallographic orientation, microstructure, etc. on the deformation has been systematically investigated. In the process, grain boundary properties, which is inaccessible through experimentation, were estimated using a cohesive traction-separation law. The simulation suggests improved structural integrity or load bearing capability can be achieved by introducing stronger crystallographic texture with more uniform grain size distribution during the CVD process.

The mechanism-based understanding developed upon this experiment-simulation approach can greatly accelerate future development of such coatings and contribute to the approach of "material by design".

5.2 Suggested Future Directions

The research activities described in this thesis are the very first steps toward developing a comprehensive understanding of such a wide range of micro-architectured refractory coating. Due to the current limitation on microstructral characterization, micro-mechanical testing, and computational power, certain amount of simplification

and idealization were made. In this chapter, a few future activities are proposed toward an improved understanding of such newly developed coating.

5.2.1 3D Microstructural Characterization

Understandings and simulations in current study were developed based on 2D characterization. It has been shown that 3D microstructures will offer richer information that will benefit both experimental understandings and simulations [221]. This could be achieved by tomographic reconstructions which includes micro-machining of the surface, with simultaneous secondary electron (SE), Electron Back Scatter Diffraction (EBSD) and Energy Dispersive Spectroscopy (EDS) analysis [222–224]. Considering the low sputtering rate and small grain size of the coating, a system which is capable of fast material removal and high quality surface finish to allow for rapid high spacial resolution mapping is necessary (e.g., the TriBeam system [94] that combines femto-second laser and FIB inside an SEM). The expected outcomes are:

- obtain a full 3D microstructure of as-processed and plasma exposed W micro-architectured coatings
- determining the statistics of the 3D grain size distributions and crystallographic texture
- determine the characteristics of the grain boundaries and the distribution of grain boundary voids that are formed during the material processing phase

- obtain digitalized 3D meshes of the microstructure for subsequent 3D microstructurally based simulations

5.2.2 Potential Experimental Directions

On the experimental side, we have carried out micro-compression experiments up to 673 K at a quasi-static strain rate of $\sim 10^{-3}$. However, considering its high melting point and cryogenic applications, it is compelling to develop knowledge at a wider temperature and strain rate regime.

Our experiments indicate that the failure is dominate by intergranular fracture, and it is known that W exhibits limited plasticity at low temperatures due to the restricted mobility of screw dislocations. Therefore, it's very likely there is a transition from intergranular to transgranular fracture at cryogenic temperatures. At the same time, it is meaningful to study the deformation at elevated temperatures where multiple mechanisms could be activated, including creep and diffusion. Both activities requires significant further development of the current testing system to address the engineering issues, for example, thermal drift, tip material, oxidization, etc..

Beyond the realm of temperature, understanding the strain-rate dependency is of scientific and practical interest. Although there are certain amount of literature that reports on the behavior for pure tungsten, this knowledge will less likely be directly transfered into the understanding such coating for its unique microstructure. Split-Hopkins pressure bar experiments are widely used to test dynamic mechanical

responses up to a strain rate of 10^3 s^{-1}, however, consider the physical dimensions of the coating, this approach may not turn out to be a practical option. An ideal and direct continuation would be to simply extend the strain rate in micro-compression experiments, and a recent development on th relative apparatus has demonstrated by Guillonneau et al. [66] and has been shown to be able to a strain rate of 100 s^{-1}.

To reach an even higher strain rate regime and mimic those seen in high-speed collisions and particle impingement in aerospace applications, there are a few microscopic high throughput ballistic test that have been developed. Phani and Oliver [68] has demonstrated a novel nanoindentation method using a combination of step and constant loads. For an even higher strain-rate, the recently developed laser induced projectile impact test (LIPIT) could be an promising candidate to an strain rate up to an astonishing 10^8 s^{-1} on micro-sized samples [225, 226]. It has been shown that a number of deformation mechanisms (e.g., for example, amortization and nanocrystallization) beyond dislocation slip start to active at such ultra high strain rates [227].

Finally, it is meaningful to extend the ongoing studies to thermo-mechanical damage after having been exposed to plasma consider its application on the plasma facing components.

5.2.3 Potential Modeling and Simulations Directions

Regarding the simulation, a number of idealizations and approximations were made in this thesis to develop a qualitative connections with our experiments.

Current simulation volumes are obtained by extrusion of 2D EBSD IPFs with 3 assumption: (1) grain boundaries are perfectly straight (2) defects are not explicitly represented in the simulation volume instead they are modeled as the constituent of the brittle "grain boundaries" (3) all grain boundaries have same properties. To make the result better connect to the experiments, a more real description of the complex microstructure and properties of the constituent element is of critical important and the suggested activities were described in Section 5.2.1.

The present crystal plasticity model has demonstrated the capability to capture the deformation observed in experiments. However, the constitutive relations based on kink-pair theory, the Taylor hardening law,the and Mecking-Kocks model is phenomenological and general, which provides limited atomistic level description of W and highly dependent on calibration. Thus, to better model the macroscopic response of tungsten, a few mechanism should be considered including the non-Schmid effects and the thermally-activated screw dislocation slip [228–230]. Incorporating these mechanisms requires better atomistic level understanding from DFT and MD calculations. Finally, the deformation is very inhomogeneous, and thus the effect of geometric necessary dislocations (GNDs) should also be considered [231].

Bibliography

[1] D. Terentyev, X. Xiao, A. Dubinko, A. Bakaeva, and H. Duan. Dislocation-mediated strain hardening in tungsten: Thermo-mechanical plasticity theory and experimental validation. *Journal of the Mechanics and Physics of Solids*, 85:1–15, 2015.

[2] Ultramet. Personal Communications with Dr. Brian Williams. 2013.

[3] D. Rivera, T. Crosby, A. Sheng, and N.M. Ghoniem. Characterization of thermomechanical damage on tungsten surfaces during long-duration plasma transients. *Journal of Nuclear Materials*, 455(1-3):500–506, 2014.

[4] O. Torrents Abad, J.M. Wheeler, J. Michler, A.S. Schneider, and E. Arzt. Temperature-dependent size effects on the strength of Ta and W micropillars. *Acta Materialia*, 103:483–494, 2016.

[5] D. Brunner and V. Glebovsky. The plastic properties of high-purity W single crystals. *Materials Letters*, 42(5):290–296, feb 2000. doi: 10.1016/S0167-577X(99)00200-1.

BIBLIOGRAPHY

[6] NASA. Astroid Initiative, 2013. URL http://www.nasa.gov/mission{_}pages/asteroids/initiative/index.html.

[7] R.J. Cassady, R.H. Frisbee, J.H. Gilland, M.G. Houts, M.R. LaPointe, C.M. Maresse-Reading, S.R. Oleson, J.E. Polk, D. Russell, and A. Sengupta. Recent advances in nuclear powered electric propulsion for space exploration. *Energy Conversion and Management*, 49(3):412–435, 2008.

[8] J.R. Brophy, C.E. Grrner, J.E. Polk, and J.M. Weiss. The ion propulsion system on NASA's space technology 4 champollion comet rendezvous mission. *35th hoint propulsion conference, AIAA*, pages 99–2856, 1999.

[9] C.A. Kluever. Comet Rendezvous Mission Design Using Solar Electric Propulsion Spacecraft. *J. Spacecraft Rockets*, 37:698–700, 2000.

[10] J.R. Brohpoy. Ion propulsion system design for the comet nucleus sample return mission. *35th joint propulsion conference, AIAA*, pages 2000–3414, 2000.

[11] O. Hankins, M. Bourham, O. Auciello, J. Stock, J. Gilligan, and B. Wehring. Parametric studies of high-heat-flux-induced erosion of surfaces in an electrothermal accelerator. In *IEEE International Conference on Plasma Science*, pages 39–40, 1989.

[12] D.G. Fearn. The ultimate performance of gridded ion thrusters for interstellar missions. *AIP Conference Proceedings*, 1-56396-91, 2000.

BIBLIOGRAPHY

[13] A. Kirschner, V. Philipps, M. Rubel, and P. Mertens. Overview of erosion mechanisms, impurity transport, and deposition in TEXTOR and related modeling. *Fusion Science and Technology*, 47(2):146–160, 2005.

[14] J.N. Brooks, D. Alman, G. Federici, D.N. Ruzic, and D.G. Whyte. Erosion/redeposition analysis: status of modeling and code validation for semi-detached tokamak edge plasmas. *Journal of Nuclear Materials*, 267–269:58–66, 1999.

[15] E. Lassner and W-D. Schubert. *Tungsten: Properties, Chemistry, Technology of the Element, Alloys, and Chemical Compounds Erik Lassner and Wolf-Dieter Schubert*. 1999.

[16] Q. Wei, T. Jiao, K. T. Ramesh, E. Ma, L. J. Kecskes, L. Magness, R. Dowding, V. U. Kazykhanov, and R. Z. Valiev. Mechanical behavior and dynamic failure of high-strength ultrafine grained tungsten under uniaxial compression. *Acta Materialia*, 54(1):77–87, 2006.

[17] V. Krstic, U. Erb, G. Palumbo, Krstic V., U. Erb, and G. Palumbo. Effect of porosity on Young's modulus of nanocrystalline materials. *Scripta Metallurgica et Materialia*, (29):1501–1504, 1993.

[18] Q. Wei, H. T. Zhang, B. E. Schuster, K. T. Ramesh, R. Z. Valiev, L. J. Kecskes, R. J. Dowding, L. Magness, and K. Cho. Microstructure and mechanical proper-

ties of super-strong nanocrystalline tungsten processed by high-pressure torsion. *Acta Materialia*, 54(15):4079–4089, 2006.

[19] A. S. Schneider, D. Kaufmann, B. G. Clark, C. P. Frick, P. A. Gruber, R. Mönig, O. Kraft, and E. Arzt. Correlation between critical temperature and strength of small-scale bcc pillars. *Physical Review Letters*, 103(10):105501, 2009.

[20] A.S. Schneider, C.P. Frick, B.G. Clark, P.A. Gruber, E. Arzt, A.S. Schneider, C.P. Frick, B.G. Clark, P.A. Gruber, and E. Arzt. Influence of orientation on the size effect in bcc pillars with different critical temperatures. *Materials Science and Engineering A*, 528(3):1540–1547, 2011.

[21] D. Fuks, A. Kiv, and A. Nemtsoff. Mechanism of strengthening of nanocrystalline tungsten. *Computer Modelling and New Technologies*, 14(3):12–16, 2010.

[22] H.L. Sun, Z.X. Song, D.G. Guo, F. Ma, and K.W. Xu. Microstructure and mechanical properties of nanocrystalline tungsten thin films. *Journal of Materials Science and Technology*, 26(1):87–92, 2010.

[23] M. Ames, J. Markmann, R. Karos, A. Michels, A. Tschöpe, and R. Birringer. Unraveling the nature of room temperature grain growth in nanocrystalline materials. *Acta Materialia*, 56(16):4255–4266, 2008.

[24] K. Zhang, J.R. Weertman, and J.A. Eastman. Rapid stress-driven grain coarsening in nanocrystalline Cu at ambient and cryogenic temperatures. *Applied Physics Letters*, 87(6):061921, 2005.

BIBLIOGRAPHY

[25] T. Chookajorn, H.A. Murdoch, and C.A. Schuh. Design of stable nanocrystalline alloys. *Science*, 337(6097):951–954, 2012.

[26] Y. Huang and T.G. Langdon. Advances in ultrafine-grained materials. *Materials Today*, 16(3):85–93, 2013.

[27] Ultramet. Refractory Metal Coatings & Freestanding Structures. Website, 2009. URL https://ultramet.com.

[28] S. Sharafat, A. Aoyama, B. Williams, and N.M. Ghoniem. Development of micro-engineered textured tungsten surfaces for high heat flux applications. *Journal of Nuclear Materials*, 442(1):S302—-S308, 2013.

[29] S. Sharafat, N.M. Ghoniem, M. Anderson, B. Williams, J. Blanchard, and L. Snead. Micro-engineered first wall tungsten armor for high average power laser fusion energy systems. *Journal of Nuclear Materials*, 347(3):217–243, 2005.

[30] D. Rivera, R.E. Wirz, and N.M. Ghoniem. Experimental measurements of surface damage and residual stresses in micro-engineered plasma facing materials. *Journal of Nuclear Materials*, 486:111–121, 2017.

[31] D. Rivera, Y. Huang, G. Po, and N.M. Ghoniem. A dislocation-based crystal viscoplasticity model with application to micro-engineered plasma-facing materials. *Journal of Nuclear Materials*, 485:231–242, 2017.

[32] C.S.R. Matthes, N.M. Ghoniem, G.Z. Li, T.S. Matlock, D.M. Goebel, C.A. Dod-

son, and R.E. Wirz. Fluence-dependent sputtering yield of micro-architectured materials. *Applied Surface Science*, 407:223–235, 2017.

[33] N.M. Ghoniem, Y. Raitses, R. Shaefer, D. Goebel, I.D. Kaganovich, A. Sehirlioglu, R. Wirz, J.-P. Alain, B. Williams, T. Crosby, Z. Chen, D. Rivera, and R. Conversano. Micro-Engineered Materials for Electric Propulsion and Pulsed Power. Progress report, Air Force Office of Scientific Research, 2012.

[34] G. D. Pettit, J. J. Cuomo, T. H. DiStefano, and J. M. Woodall. Solar absorbing surfaces of anodized dendritic tungsten. *IBM Journal of Research and Development*, 22(4):372–377, 1978.

[35] C.M. Lampert. Coatings for enhanced photothermal energy collection I. Selective absorbers. *Solar Energy Materials*, 1(5-6):319–341, 1979.

[36] S. S. Brenner. Tensile strength of whiskers. *Journal of Applied Physics*, 27(12): 1484–1491, 1956.

[37] S. S. Brenner. Plastic deformation of copper and silver whiskers. *Journal of Applied Physics*, 28(9):1023–1026, 1957.

[38] H. Suzuki, S. Ikeda, and S. Takeuchi. Deformation of Thin Copper Crystals. *Journal of the Physical Society of Japan*, 11(4):382–393, 1956.

[39] S. I. Bulychev, V. P. Alekhin, M. K. Shorshorov, A. P. Ternovskii, and

G. Shnyrev. Determination of Young's Modulus From the Indentor Impression Diagram, 1975.

[40] G.M. Pharr, W.C. Oliver, and F.R. Brotzen. On the generality of the relationship among contact stiffness, contact area, and elastic modulus during indentation. *Journal of Materials Research*, 7(03):613–617, 1992.

[41] W.C. Oliver and G.M Pharr. An improved technique for determining hardness and elastic modulus using load and displacement-sensing indentation systems. *Journal of Materials Research*, 7(6):1564–1583, 1992.

[42] W.C. Oliver and G.M. Pharr. Measurement of hardness and elastic modulus by instrumented indentation: Advances in understanding and refinements to methodology. *Journal of Materials Research*, 19(01):3–20, 2004.

[43] W.D. Nix and H. Gao. Indentation size effects in crystalline materials: A law for strain gradient plasticity. *Journal of the Mechanics and Physics of Solids*, 46(3):411–425, 1998.

[44] M.D. Uchic, D.M. Dimiduk, J.N. Florando, and W.D. Nix. Sample dimensions influence strength and crystal plasticity. *Science*, 305(5686):986–989, 2004.

[45] Michael D. Uchic and Dennis M. Dimiduk. A methodology to investigate size scale effects in crystalline plasticity using uniaxial compression testing. *Materials Science and Engineering: A*, 400-401:268–278, 2005.

BIBLIOGRAPHY

[46] Michael D. Uchic, Paul A. Shade, and Dennis M. Dimiduk. Plasticity of micrometer-scale single crystals in compression. *Annual Review of Materials Research*, 39(1):361–386, 2009.

[47] J.R. Greer and J.Th.M. De Hosson. Plasticity in small-sized metallic systems: intrinsic versus extrinsic size effect. *Progress in Materials Science*, 56(6):654–724, 2011.

[48] G. Dehm, B.N. Jaya, R. Raghavan, and C. Kirchlechner. Overview on micro- and nanomechanical testing: New insights in interface plasticity and fracture at small length scales. *Acta Materialia*, 142:248–282, 2018.

[49] D. Kiener, W. Grosinger, G. Dehm, and R. Pippan. A further step towards an understanding of size-dependent crystal plasticity: In situ tension experiments of miniaturized single-crystal copper samples. *Acta Materialia*, 56(3):580–592, 2008.

[50] Z. W. Shan, Raja K. Mishra, S. A. Syed Asif, Oden L. Warren, and Andrew M. Minor. Mechanical annealing and source-limited deformation in submicrometre-diameter Nicrystals. *Nature Materials*, 7(2):115–119, feb 2008. ISSN 14764660. doi: 10.1038/nmat2085. URL http://www.nature.com/articles/nmat2085.

[51] S.H. Oh, M. Legros, D. Kiener, and G. Dehm. In situ observation of dislocation nucleation and escape in a submicrometre aluminium single crystal. *Nature Materials*, 2009.

BIBLIOGRAPHY

[52] D. Kiener, P. Hosemann, S. A. Maloy, and A. M. Minor. In situ nanocompression testing of irradiated copper. *Nature Materials*, 10(8):608–613, 2011.

[53] S. Lee, J. Im, Y. Yoo, E. Bitzek, D. Kiener, Gu. Richter, B. Kim, and S.H. Oh. Reversible cyclic deformation mechanism of gold nanowires by twinning-detwinning transition evidenced from in situ TEM. *Nature Communications*, 5 (1):3033, 2014.

[54] D. Di Maio and S.G. Roberts. Measuring fracture toughness of coatings using focused-ion-beam-machined microbeams. *Journal of Materials Research*, 20 (02):299–302, 2005.

[55] K. Matoy, H. Schönherr, T. Detzel, T. Schöberl, R. Pippan, C. Motz, and G. Dehm. A comparative micro-cantilever study of the mechanical behavior of silicon based passivation films. *Thin Solid Films*, 518(1):247–256, 2009.

[56] S. Brinckmann, C. Kirchlechner, and G. Dehm. Stress intensity factor dependence on anisotropy and geometry during micro-fracture experiments. *Scripta Materialia*, 127:76–78, 2017.

[57] J. Chen and S.J. Bull. Approaches to investigate delamination and interfacial toughness in coated systems: An overview. *Journal of Physics D: Applied Physics*, 44(3):034001, 2011.

[58] D.E.J. Armstrong, A. J. Wilkinson, and S. G. Roberts. Micro-mechanical mea-

surements of fracture toughness of bismuth embrittled copper grain boundaries. *Philosophical Magazine Letters*, 91(6):394–400, 2011.

[59] Y. Zou, P. Okle, H. Yu, T. Sumigawa, T. Kitamura, S. Maiti, W. Steurer, and R. Spolenak. Fracture properties of a refractory high-entropy alloy: In situ micro-cantilever and atom probe tomography studies. *Scripta Materialia*, 128: 95–99, feb 2017.

[60] S. Lavenstein, B. Crawford, G-D Sim, P.A. Shade, C. Woodward, and J.A. El-Awady. High frequency in situ fatigue response of Ni-base superalloy René-N5 microcrystals. *Acta Materialia*, 144:154–163, feb 2018.

[61] S-W. Lee, Y. Cheng, I. Ryu, and J.R. Greer. Cold-temperature deformation of nano-sized tungsten and niobium as revealed by in-situ nano-mechanical experiments. *Science China Technological Sciences*, 2014.

[62] J.T. Sypek, H. Yu, K.J. Dusoe, G. Drachuck, H. Patel, A.M. Giroux, A.I. Goldman, A. Kreyssig, P.C. Canfield, S.L. Bud'Ko, C.R. Weinberger, and S-W. Lee. Superelasticity and cryogenic linear shape memory effects of CaFe2As2. *Nature Communications*, 8(1):1083, 2017.

[63] J.M. Wheeler, D.E.J. Armstrong, W. Heinz, and R. Schwaiger. High temperature nanoindentation: The state of the art and future challenges. *Current Opinion in Solid State and Materials Science*, 19(6):354–366, dec 2015.

[64] J. M. Wheeler, R. Raghavan, V. Chawla, J. Zechner, I. Utke, and J. Michler. Failure mechanisms in metal-metal nanolaminates at elevated temperatures: Microcompression of Cu-W multilayers. *Scripta Materialia*, 98(15):28–31, 2015.

[65] Q. Li, J. Cho, S. Xue, X. Sun, Y. Zhang, Z. Shang, H. Wang, and X. Zhang. High temperature thermal and mechanical stability of high-strength nanotwinned Al alloys. *Acta Materialia*, 165(15):142–152, 2019.

[66] G. Guillonneau, M. Mieszala, J. Wehrs, J. Schwiedrzik, S. Grop, D. Frey, L. Philippe, J.M. Breguet, J. Michler, and J.M. Wheeler. Nanomechanical testing at high strain rates: New instrumentation for nanoindentation and microcompression. *Materials and Design*, 148:39–48, 2018.

[67] J. M. Wheeler, J. Dean, and T. W. Clyne. Nano-impact indentation for high strain rate testing: The influence of rebound impacts. *Extreme Mechanics Letters*, 26:35–39, 2019.

[68] P. S. Phani and W.C. Oliver. Ultra high strain rate nanoindentation testing. *Materials*, 10(6):663, 2017.

[69] Y. Deng and A. Barnoush. Hydrogen embrittlement revealed via novel in situ fracture experiments using notched micro-cantilever specimens. *Acta Materialia*, 142:236–247, 2018.

[70] B.R.S. Rogne, N. Kheradmand, Y. Deng, and A. Barnoush. In situ microme-

chanical testing in environmental scanning electron microscope: A new insight into hydrogen-assisted cracking. *Acta Materialia*, 144:257–268, 2018.

[71] David S. Sholl and Janice A. Steckel. *Density Functional Theory: A Practical Introduction*. 2009.

[72] P. Cao, X. Ni, F. Tian, L.K. Varga, and L. Vitos. Ab initio study of AlxMoNbTiV high-entropy alloys. *Journal of Physics Condensed Matter*, 27(7): 075401, 2015.

[73] F. Ercolesi and J. B. Adams. Interatomic potentials from first-principles calculations: The force-matching method. *Europhysics Letters*, 26(8):583–588, 1994.

[74] J. Li, K. J. Van Vliet, Ti. Zhu, S. Yip, and S. Suresh. Atomistic mechanisms governing elastic limit and incipient plasticity in crystals. *Nature*, 418:307–310, 2002.

[75] B. Li and E. Ma. Atomic Shuffling Dominated Mechanism for Deformation Twinning in Magnesium. *Physical Review Letters*, 103(3):035503, 2009.

[76] H. Fan, Y. Zhu, J.A. El-Awady, and D. Raabe. Precipitation hardening effects on extension twinning in magnesium alloys. *International Journal of Plasticity*, 106:186–202, jul 2018.

[77] X. Liu, S.K. Schnell, J.M. Simon, P. Krüger, D. Bedeaux, S. Kjelstrup, A. Bardow, and T.J.H. Vlugt. Diffusion coefficients from molecular dynamics simula-

tions in binary and ternary mixtures. *International Journal of Thermophysics*, 34(7):1169–1196, 2013.

[78] M. De Koning, R. Miller, V.V. Bulatov, and F.F. Abraham. Modelling grain-boundary resistance in intergranular dislocation slip transmission. *Philosophical Magazine A*, 82(13):2511–2527, 2002.

[79] Y. Qi and P.E. Krajewski. Molecular dynamics simulations of grain boundary sliding: The effect of stress and boundary misorientation. *Acta Materialia*, 55 (5):1555–1563, 2007.

[80] R. J. Amodeo and N. M. Ghoniem. Dislocation dynamics. {I}. A proposed methodology for deformation micromechanics. *Physical Review B*, 41(10):6958–6967, 1990.

[81] E. Tarleton, D.S. Balint, J. Gong, and A.J. Wilkinson. A discrete dislocation plasticity study of the micro-cantilever size effect. *Acta Materialia*, 88(15): 271–282, 2015.

[82] S. I. Rao, C. Woodward, B. Akdim, E. Antillon, T. A. Parthasarathy, J. A. El-Awady, and D. M. Dimiduk. Large-scale dislocation dynamics simulations of strain hardening of Ni microcrystals under tensile loading. *Acta Materialia*, 164:171–183, feb 2019.

[83] J.A. El-Awady. Unravelling the physics of size-dependent dislocation-mediated plasticity. *Nature communications*, 6:5926, jan 2015.

[84] R.B. Sills, A. Aghaei, and W. Cai. Advanced time integration algorithms for dislocation dynamics simulations of work hardening. *Modelling and Simulation in Materials Science and Engineering*, 24(2):045019, 2016.

[85] F. Ferroni, E. Tarleton, and S. Fitzgerald. GPU accelerated dislocation dynamics. *Journal of Computational Physics*, 272:619–628, 2014.

[86] H. Fan, Z. Li, and M. Huang. Toward a further understanding of intermittent plastic responses in the compressed single/bicrystalline micropillars. *Scripta Materialia*, 66(10):813–816, 2012.

[87] H. Fan, S. Aubry, A. Arsenlis, and J.A. El-Awady. The role of twinning deformation on the hardening response of polycrystalline magnesium from discrete dislocation dynamics simulations. *Acta Materialia*, 92(15):126–139, 2015.

[88] S.G. Ma, S.F. Zhang, J.W. Qiao, Z.H. Wang, M.C. Gao, Z.M. Jiao, H.J. Yang, and Y. Zhang. Superior high tensile elongation of a single-crystal CoCrFeNiAl0.3high-entropy alloy by Bridgman solidification. *Intermetallics*, 54:104–109, 2014.

[89] A. Ma, F. Roters, and D. Raabe. A dislocation density based constitutive model for crystal plasticity FEM including geometrically necessary dislocations. *Acta Materialia*, 54(8):2169–2179, 2006.

[90] Surya R. Kalidindi. A Crystal Plasticity Framework for Deformation Twinning.

In *Continuum Scale Simulation of Engineering Materials*, pages 543–560. Wiley-VCH Verlag GmbH & Co. KGaA, Weinheim, FRG, 2005.

[91] J. Cheng, J. Shen, R.K. Mishra, and S. Ghosh. Discrete twin evolution in Mg alloys using a novel crystal plasticity finite element model. *Acta Materialia*, 149:142–153, 2018.

[92] A. Ma, F. Roters, and D. Raabe. On the consideration of interactions between dislocations and grain boundaries in crystal plasticity finite element modeling - Theory, experiments, and simulations. *Acta Materialia*, 54(8):2181–2194, 2006.

[93] J. Thomas, M. Groeber, and S. Ghosh. Image-based crystal plasticity FE framework for microstructure dependent properties of Ti-6Al-4V alloys. *Materials Science and Engineering A*, 553:164–175, 2012.

[94] M. Echlin, A. Mottura, and T. Pollock. The Tri-Beam System: Femtosecond Laser Based Tomography in a Dual-Beam FIB. *Microscopy and Microanalysis*, 17(S2):958–959, jul 2011.

[95] J. Cheng, A. Shahba, and S. Ghosh. Stabilized tetrahedral elements for crystal plasticity finite element analysis overcoming volumetric locking. *Computational Mechanics*, 57(5):733–753, 2016.

[96] Y. Lv, J. Song, Y. Lian, Y. Yu, X. Liu, and Z. Zhuang. The thermal properties of high purity and fully dense tungsten produced by chemical vapor deposition. *Journal of Nuclear Materials*, 457(2015):317–323, 2015.

[97] J. Hütsch and E.T. Lilleodden. The influence of focused-ion beam preparation technique on microcompression investigations: Lathe vs. annular milling. *Scripta Materialia*, 77:49–51, apr 2014.

[98] D. Frey, J. Wehrs, X. Maeder, J. Michler, G. Guillonneau, J.M. Wheeler, A.A. Taylor, L. Philippe, S. Mischler, and G. Mohanty. Comparison of in situ micromechanical strain-rate sensitivity measurement techniques. *JOM*, 67 (8):1684–1693, 2015.

[99] D. Kiener, C. Motz, M. Rester, M. Jenko, and G. Dehm. FIB damage of Cu and possible consequences for miniaturized mechanical tests. *Materials Science and Engineering A*, 459(1-2):262–272, 2007.

[100] Y. Xiao, V. Maier-Kiener, J. Michler, R. Spolenak, and J. M. Wheeler. Deformation behavior of aluminum pillars produced by Xe and Ga focused ion beams: insights from strain rate jump tests. *To be published*, dec 2019.

[101] Q. Yu, X. Huang, L. Xiao, J. Sun, J. Li, Z-W. Shan, J. Li, X. Huang, L. Xiao, J. Sun, and E. Ma. Strong crystal size effect on deformation twinning. *Nature*, 463(7279):335–338, jan 2010. ISSN 0028-0836. doi: 10.1038/nature08692.

[102] C. Marichal, K. Srivastava, D. Weygand, S. Van Petegem, D. Grolimund, P. Gumbsch, and H. Van Swygenhoven. Origin of anomalous slip in tungsten. *Physical Review Letters*, 113(2):1–5, jul 2014.

[103] D. Kiener, C. Motz, and G. Dehm. Micro-compression testing: A critical discussion of experimental constraints. *Materials Science and Engineering A*, 505 (1-2):79–87, 2009.

[104] J.M. Wheeler, R.A. Oliver, and T.W. Clyne. AFM observation of diamond indenters after oxidation at elevated temperatures. *Diamond and Related Materials*, 19(11):1348–1353, 2010.

[105] J. M. Wheeler and J. Michler. Elevated temperature, nano-mechanical testing in situ in the scanning electron microscope. *Review of Scientific Instruments*, 84(4):045103, apr 2013.

[106] N. M. Everitt, M. I. Davies, and J. F. Smith. High temperature nanoindentation - The importance of isothermal contact. *Philosophical Magazine*, 91(7-9):1221–1244, mar 2011.

[107] P. S. Phani and W. C. Oliver. A direct comparison of high temperature nanoindentation creep and uniaxial creep measurements for commercial purity aluminum. *Acta Materialia*, 111:31–38, 2016.

[108] I.N. Sneddon. The relation between load and penetration in the axisymmetric boussinesq problem for a punch of arbitrary profile. *International Journal of Engineering Science*, 3(1):47–57, 1965.

[109] J.R. Greer, W.C. Oliver, and W.D. Nix. Size dependence of mechanical prop-

erties of gold at the micron scale in the absence of strain gradients. *Acta Materialia*, 53(6):1821–1830, apr 2005.

[110] R. Raghavan, T.P. Harzer, V. Chawla, S. Djaziri, B. Phillipi, J. Wehrs, J.M. Wheeler, J. Michler, and G. Dehm. Comparing small scale plasticity of copper-chromium nanolayered and alloyed thin films at elevated temperatures. *Acta Materialia*, 93:175–186, 2015.

[111] A. Giannattasio, Z. Yao, E. Tarleton, and S.G. Roberts. Brittle–ductile transitions in polycrystalline tungsten. *Philosophical Magazine*, 90(30):3947–3959, 2010.

[112] A.A.N. Németh, J. Reiser, D.E.J Armstrong, and M. Rieth. The nature of the brittle-to-ductile transition of ultra fine grained tungsten (W) foil. *International Journal of Refractory Metals and Hard Materials*, 50:9–15, may 2015.

[113] V. Vitek. Core structure of screw dislocations in body-centred cubic metals: Relation to symmetry and interatomic bonding. *Philosophical Magazine*, 84 (3-5):415–428, 2004.

[114] R. Fritz, D. Wimler, A. Leitner, V. Maier-Kiener, and D. Kiener. Dominating deformation mechanisms in ultrafine-grained chromium across length scales and temperatures. *Acta Materialia*, 140:176–187, 2017.

[115] D. Brunner. Temperature dependence of the plastic flow of high-purity tungsten

single crystals. *International Journal of Materials Research*, 101(8):1003–1013, 2010.

[116] J. W. Christian. Some surprising features of the plastic deformation of body-centered cubic metals and alloys. *Metallurgical Transactions A*, 14(7):1237–1256, 1983.

[117] H. Conrad, S. Feuerstein, and L. Rice. Effects of grain size on the dislocation density and flow stress of niobium. *Materials Science and Engineering*, 2(3): 157–168, 1967.

[118] T. Narutani and J. Takamura. Grain-size strengthening in terms of dislocation density measured by resistivity. *Acta Metallurgica Et Materialia*, 39(8):2037–2049, 1991.

[119] H. Conrad. Grain-size dependence of the flow stress of Cu from millimeters to nanometers. *Metallurgical and Materials Transactions A: Physical Metallurgy and Materials Science*, 35 A(9):2681–2695, 2004.

[120] Dieter Brunner. Comparison of flow-stress measurements on high-purity tungsten single crystals with the kink-pair theory, 2000.

[121] R. Lowrie and A.M. Gonas. Single-Crystal Elastic Properties of Tungsten from 24° to 1800°C. *Journal of Applied Physics*, 38(11):4505–4509, oct 1967.

[122] T.A. Parthasarathy, S.I. Rao, D.M. Dimiduk, M.D. Uchic, and D.R. Trinkle.

Contribution to size effect of yield strength from the stochastics of dislocation source lengths in finite samples. *Scripta Mater.*, 56(4):313–316, 2007.

[123] S. I. Rao, D. M. Dimiduk, T. A. Parthasarathy, M. D. Uchic, M. Tang, and C. Woodward. Athermal mechanisms of size-dependent crystal flow gleaned from three-dimensional discrete dislocation simulations. *Acta Material*, 56(13): 3245–3259, 2008.

[124] S-W. Lee and W.D. Nix. Size dependence of the yield strength of fcc and bcc metallic micropillars with diameters of a few micrometers. *Philosophical Magazine*, 92(10):1238–1260, 2012. ISSN 14786435. doi: 10.1080/14786435.2011.643250.

[125] G. K. Williamson and R. E. Smallman. III. Dislocation densities in some annealed and cold-worked metals from measurements on the X-ray Debye-Scherrer spectrum. *Philosophical Magazine*, 1(1):34–46, jan 1956.

[126] V. G. Glebovsky and V. N. Semenov. Perfection of tungsten single crystals grown from the melt and solid state. *Vacuum*, 53(1-2):71–74, may 1999.

[127] T. P. Weihs, S. Hong, J. C. Bravman, and W. D. Nix. Mechanical deflection of cantilever microbeams: A new technique for testing the mechanical properties of thin films. *Journal of Materials Research*, 3(5):931–942, 1988.

[128] D.E.J Armstrong, A.J. Wilkinson, and S.G. Roberts. Measuring anisotropy in

Young's modulus of copper using microcantilever testing. *Journal of Materials Research*, 24(11):3268–3276, 2009.

[129] F. Iqbal, J. Ast, M. Göken, and K. Durst. In situ micro-cantilever tests to study fracture properties of NiAl single crystals. *Acta Materialia*, 60(3):1193–1200, 2012.

[130] Johannes Ast, Mathias Göken, and Karsten Durst. Size-dependent fracture toughness of tungsten. *Acta Materialia*, 138:198–211, 2017.

[131] G. I. Taylor. Plastic strain in metals. *Journal of the Institute of Metals*, 62: 307–324, 1938.

[132] G. Sachs. Plasticity problems in metals. *Transactions of the Faraday Society*, 24:84, 1928.

[133] Bernard Budiansky and TAI TE Wu. Theoretical prediction of plastic strains of polycrystals. *Proc. Fourth U.S. National Congress of Applied Mechanics*, 1: 1175–1185, 1962.

[134] R. Hill. Continuum micro-mechanics of elastoplastic polycrystals. *Journal of the Mechanics and Physics of Solids*, 13(2):89–101, 1965.

[135] R. Hill. A self-consistent mechanics of composite materials. *Journal of the Mechanics and Physics of Solids*, 13(4):213–222, 1965.

[136] A. Molinari, G.R. Canova, and S. Ahzi. A self consistent approach of the large deformation polycrystal viscoplasticity. *Acta Metallurgica*, 35(12):2983–2994, 1987.

[137] E. H. Lee. Elastic-Plastic Deformation at Finite Strains. *Journal of Applied Mechanics*, 36(1):1, 1969.

[138] R. J. Asaro and J. R. Rice. Strain localization in ductile single crystals. *Journal of the Mechanics and Physics of Solids*, 25(5):309–338, 1977.

[139] J. W. Hutchinson. Bounds and self-consistent estimates for creep of polycrystalline materials. *Proceedings of the Royal Society A: Mathematical, Physical and Engineering Sciences*, 348(1652):101–127, feb 1976.

[140] J. Pan and J.R. Rice. Rate sensitivity of plastic flow and implications for yield-surface vertices. *International Journal of Solids and Structures*, 19(11):973–987, 1983.

[141] D. Peirce, R. J. Asaro, and A. Needleman. Material rate dependence and localized deformation in crystalline solids. *Acta Metallurgica*, 31(12):1951–1976, 1983.

[142] H. Lim, C.C. Battaile, J.D. Carroll, B. L. Boyce, and C.R. Weinberger. A physically based model of temperature and strain rate dependent yield in BCC metals: Implementation into crystal plasticity. *Journal of the Mechanics and Physics of Solids*, 74:80–96, 2015.

[143] M. G. Lee, H. Lim, B. L. Adams, J. P. Hirth, and R. H. Wagoner. A dislocation density-based single crystal constitutive equation. *International Journal of Plasticity*, 26(7):925–938, 2010.

[144] J. Hu, Y. N. Shi, X. Sauvage, G. Sha, and K. Lu. Grain boundary stability governs hardening and softening in extremely fine nanograined metals. *Science*, 355(6331):1292–1296, 2017.

[145] E O Hall. The deformation and ageing of mild steel: {III} discussion of results. *Proceedings of the Physical Society. Section B*, 64:747–753, 1951.

[146] N.J. J Petch. The cleavage strength of polycrystals. *Journal of the Iron and Steel Institute*, 174:25–28, 1953. ISSN 00354511.

[147] H. Mecking and U.F. F Kocks. Kinetics of flow and strain-hardening. *Acta Metallurgica*, 29(11):1865–1875, 1981.

[148] I. J. Beyerlein and C. N. Tomé. A dislocation-based constitutive law for pure Zr including temperature effects. *International Journal of Plasticity*, 24(5): 867–895, 2008.

[149] K. Ito and V. Vitek. Atomistic study of non-Schmid effects in the plastic yielding of bcc metals. *Philosophical Magazine A: Physics of Condensed Matter, Structure, Defects and Mechanical Properties*, 81(5):1387–1407, 2001.

[150] C. Woodward and S. I. Rao. Ab-initio simulation of isolated screw dislocations

in bcc Mo and Ta. *Philosophical Magazine A: Physics of Condensed Matter, Structure, Defects and Mechanical Properties*, 81(5):1305–1316, 2001.

[151] A. Seeger. The temperature and strain-rate dependence of the flow stress of body-centered cubic metals: A theory based on kink-kink interactions. *Zeitschrift fur Metallkunde*, 1981.

[152] Alfred Seeger. Peierls barriers, kinks, and flow stress: Recent progress. *Zeitschrift für Metallkunde*, 93(8):760–777, aug 2002.

[153] A. Seeger and U. Holzwarth. Slip planes and kink properties of screw dislocations in high-purity niobium. *Philosophical Magazine*, 86(25-26):3861–3892, 2006.

[154] D. Caillard and J.L. Martin. *Thermally activated mechanisms in crystal plasticity*, volume 54. 2003.

[155] J.P. Hirth and J. Lothe. *Theory of dislocations.* John Wiley & Sons, New York, 2nd edition, 1982.

[156] A. Argon. *Strengthening Mechanisms in Crystal Plasticity*, volume 9780198516. 2007.

[157] J.D. Eshelby. The interaction of kinks and elastic waves. *Proceedings of the Royal Society A: Mathematical, Physical and Engineering Sciences*, 266(1325): 222–246, 1962.

BIBLIOGRAPHY

[158] J E Dorn and S Rajnak. Nucleation of kink pairs and the Peierls' mechanism of plastic deformation. *Transactions of The Metallurgical Society of AIME*, 230 (5):1052–1064, 1964.

[159] H. Koizumi, H.O.K. Kirchner, and T. Suzuki. Kink pair nucleation and critical shear stress. *Acta Metallurgica Et Materialia*, 41(12):3483–3493, 1993.

[160] V. Celli, M. Kabler, T. Ninomiya, and R. Thomson. Theory of dislocation mobility in semiconductors. *Physical Review*, 131(1):58–72, 1963.

[161] P. Gumbsch, J. Riedle, Al. Hartmaier, and H.F. Fischmeister. Controlling factors for the brittle-to-ductile transition in tungsten single crystals. *Science*, 282(5392):1293–1295, 1998.

[162] S. R. Kalidindi, C. A. Bronkhorst, and L. Anand. Crystallographic texture evolution in bulk deformation processing of FCC metals. *Journal of the Mechanics and Physics of Solids*, 40(3):537–569, 1992.

[163] Srihari Balasubramanian. *Polycrystalline Plasticity: Application to Deformation Processing of Lightweight Metals*. PhD thesis, 1998.

[164] G.I. Barenblatt. The formation of equilibrium cracks during brittle fracture. General ideas and hypotheses. Axially-symmetric cracks. *Journal of Applied Mathematics and Mechanics*, 23(3):622–636, 1959.

BIBLIOGRAPHY

[165] D.S. Dugdale. Yielding of steel sheets containing slits. *Journal of the Mechanics and Physics of Solids*, 8(2):100–104, 1960.

[166] J. W. Hutchinson and a. G. Evans. Mechanics of materials: top-down approaches to fracture. *Acta Materialia*, 48(1):125–135, jan 2000.

[167] A. Hillerborg, M. Modéer, and P. E. Petersson. Analysis of crack formation and crack growth in concrete by means of fracture mechanics and finite elements. *Cement and Concrete Research*, 6(6):773–781, nov 1976.

[168] I. Simonovski and L. Cizelj. Cohesive element approach to grain level modelling of intergranular cracking. *Engineering Fracture Mechanics*, 110:364–377, 2013.

[169] P. Rahulkumar, A. Jagota, S. J. Bennison, and S. Saigal. Cohesive element modeling of viscoelastic fracture: Application to peel testing of polymers. *International Journal of Solids and Structures*, 37(13):1873–1807, 2000.

[170] G.T. Camacho and M. Ortiz. Computational modelling of impact damage in brittle materials. *International Journal of Solids and Structures*, 33(20-22): 2899–2938, 1996.

[171] J. Jang, M. Sung, S. Han, and W.R. Yu. Prediction of delamination of steel-polymer composites using cohesive zone model and peeling tests. *Composite Structures*, 160(15):118–127, 2017. ISSN 02638223. doi: 10.1016/j.compstruct.2016.10.025.

BIBLIOGRAPHY

[172] X.P. Xu and A. Needleman. Numerical simulations of fast crack growth in brittle solids. *Journal of the Mechanics and Physics of Solids*, 42(9):1397–1434, 1994.

[173] B. Yang, S. Mall, and K. Ravi-Chandar. A cohesive zone model for fatigue crack growth in quasibrittle materials. *International Journal of Solids and Structures*, 38(22-23):3927–3944, 2001. ISSN 00207683. doi: 10.1016/S0020-7683(00)00253-5.

[174] C. Shet and N. Chandra. Analysis of energy balance when using cohesive zone models to simulate fracture processes. *Journal of Engineering Materials and Technology*, 124(4):440–450, 2002.

[175] A. Needleman. A continuum model for void nucleation by inclusion debonding. *Journal of Applied Mechanics*, 54(3):525, 1987.

[176] A. Needleman. An analysis of tensile decohesion along an interface. *Journal of the Mechanics and Physics of Solids*, 38(3):289–324, 1990.

[177] V. Tvergaard and J.W. Hutchinson. The influence of plasticity on mixed mode interface toughness. *Journal of the Mechanics and Physics of Solids*, 41(6):1119–1135, jun 1993.

[178] P.H. Geubelle and J.S. Baylor. Impact-induced delamination of composites: a 2D simulation. *Composites Part B: Engineering*, 29(5):589–602, 1998.

[179] K. Park, G.H. Paulino, and J.R. Roesler. A unified potential-based cohesive model of mixed-mode fracture. *Journal of the Mechanics and Physics of Solids*, 57(6):891–908, 2009.

[180] Z. Li, S. Ghosh, N. Getinet, and D.J. O'Brien. Micromechanical modeling and characterization of damage evolution in glass fiber epoxy matrix composites. *Mechanics of Materials*, 99:37–52, 2016.

[181] X. Zhang, D.J. O'Brien, and S. Ghosh. Parametrically homogenized continuum damage mechanics (PHCDM) models for composites from micromechanical analysis. *Computer Methods in Applied Mechanics and Engineering*, 346: 456–485, 2019. ISSN 00457825. doi: 10.1016/j.cma.2018.12.005.

[182] ABAQUS. ABAQUS, 2012.

[183] I. Simonovski and L. Cizelj. Cohesive zone modeling of intergranular cracking in polycrystalline aggregates. *Nuclear Engineering and Design*, 283:139–147, mar 2015.

[184] M. L. Benzeggagh and M. Kenane. Measurement of mixed-mode delamination fracture toughness of unidirectional glass/epoxy composites with mixed-mode bending apparatus. *Composites Science and Technology*, 56(4):439–449, 1996.

[185] F. Ackermann, H. Mughrabi, and A. Seeger. Temperature- and strain-rate dependence of the flow stress of ultrapure niobium single crystals in cyclic deformation. *Acta Metallurgica*, 31(9):1353–1366, 1983.

[186] M. Werner. Temperature and strain-rate dependence of the Flow Stress of Ultrapure Tantalum Single Crystals. *physica status solidi (a)*, 104(2):63–78, 1987.

[187] A Seeger and U Holzwarthy. Philosophical Magazine Slip planes and kink properties of screw dislocations high-purity niobium Slip planes and kink properties of screw dislocations in high-purity niobiumzin. *Philosophical Magazine*, 86: 25–26, 2006.

[188] L. Hollang, M. Hommel, and A. Seeger. The flow stress of ultra-high-purity molybdenum single crystals. *Physica Status Solidi (A) Applied Research*, 160 (2):329–354, 1997.

[189] D. Brunner and V. Glebovsky. Plastic properties of high-purity W single crystals. *Materials Letters*, 42(5):290–296, 2000.

[190] V. G. Glebovsky, V. V. Lomeyko, and V. N. Semenov. Unit for electron-beam zone melting of refractory materials. *Journal of The Less-Common Metals*, 117 (1-2):385–389, 1986.

[191] V. G. Glebovsky, V. N. Semenov, and V. V. Lomeyko. Influence of the crystallization conditions on the structural perfection of molybdenum and tungsten single crystals. *Journal of Crystal Growth*, 87(1):142–150, 1988.

[192] V. G. Glebovsky and V. N. Semenov. Electron-beam floating zone melting

of refractory metals and alloys: Art and Science. *International Journal of Refractory Metals and Hard Materials*, 12(5):295–301, 1993.

[193] C.R. Weinberger, B.L. Boyce, and C.C. Battaile. Slip planes in bcc transition metals. *International Materials Reviews*, 58(5):296–314, jun 2013.

[194] L. Kaun, A. Luft, J. Richter, and D. Schulze. Slip Line Pattern and Active Slip Systems of Tungsten and Molybdenum Single Crystals Weakly Deformed in Tension at Room Temperature. *physica status solidi (b)*, 26(2):485–499, 1968.

[195] P. Beardmore and D. Hull. Deformation and fracture of tungsten single crystals. *Journal of The Less-Common Metals*, 9(3):168–180, 1965.

[196] H.W. Schadler. Deformation behavior of zone-melted tungsten single crystals. *Transactions of The Metallurgical Society of AIME*, 218:649–655, 1960.

[197] J.Y. Kim, D. Jang, and J.R. Greer. Tensile and compressive behavior of tungsten, molybdenum, tantalum and niobium at the nanoscale. *Acta Materialia*, 58(7):2355–2363, apr 2010.

[198] D. Kiener, R. Fritz, M. Alfreider, A. Leitner, R. Pippan, and V. Maier-Kiener. Rate limiting deformation mechanisms of bcc metals in confined volumes. *Acta Materialia*, 166:687–701, 2019.

[199] A. Leitner, V. Maier-Kiener, and D. Kiener. Extraction of flow behavior and

Hall–Petch parameters using a nanoindentation multiple sharp tip approach. *Advanced Engineering Materials*, 19(4):1600669, 2017.

[200] I. Mohammed and K.M. Liechti. Cohesive zone modeling of crack nucleation at bimaterial corners. *Journal of the Mechanics and Physics of Solids*, 48(4): 735–764, apr 2000.

[201] Q. D. Yang, M. D. Thouless, and S. M. Ward. Numerical simulations of adhesively-bonded beams failing with extensive plastic deformation. *Journal of the Mechanics and Physics of Solids*, 47(6):1337–1353, 1999. ISSN 00225096. doi: 10.1016/S0022-5096(98)00101-X.

[202] A.P. Awasthi, D.C. Lagoudas, and D.C. Hammerand. Modeling of graphene-polymer interfacial mechanical behavior using molecular dynamics. *Modelling and Simulation in Materials Science and Engineering*, 17(1):015002, 2009. ISSN 09650393. doi: 10.1088/0965-0393/17/1/015002.

[203] C.R. Dandekar and Y.C. Shin. Molecular dynamics based cohesive zone law for describing Al-SiC interface mechanics. *Composites Part A: Applied Science and Manufacturing*, 42(4):355–363, 2011.

[204] S.C. Chowdhury and J.W. Gillespie. Silica–silane coupling agent interphase properties using molecular dynamics simulations. *Journal of Materials Science*, 52(22):12981–12998, 2017.

[205] V. Yamakov, E. Saether, D.R. Phillips, and E.H. Glaessgen. Molecular-dynamics simulation-based cohesive zone representation of intergranular fracture processes in aluminum. *Journal of the Mechanics and Physics of Solids*, 54(9):1899–1928, sep 2006.

[206] X. W. Zhou, J. A. Zimmerman, E. D. Reedy, and N. R. Moody. Molecular dynamics simulation based cohesive surface representation of mixed mode fracture. *Mechanics of Materials*, 2008. ISSN 01676636. doi: 10.1016/j.mechmat.2008.05.001.

[207] J. T. Lloyd, J. A. Zimmerman, R. E. Jones, X. W. Zhou, and D. L. McDowell. Finite element analysis of an atomistically derived cohesive model for brittle fracture. *Modelling and Simulation in Materials Science and Engineering*, 19 (6), 2011. ISSN 09650393. doi: 10.1088/0965-0393/19/6/065007.

[208] Y.J. Wei and L. Anand. Grain-boundary sliding and separation in polycrystalline metals: application to nanocrystalline fcc metals. *Journal of the Mechanics and Physics of Solids J. Mech. Phys. Solids*, 52(52):2587–2616, 2004.

[209] D. Kupka, N. Huber, and E.T. Lilleodden. A combined experimental-numerical approach for elasto-plastic fracture of individual grain boundaries. *Journal of the Mechanics and Physics of Solids*, 64(1):455–467, 2014.

[210] P. Camanho and C.G. Davila. Mixed-mode decohesion finite elements in for

the simulation composite of delamination materials. *Technical Report Nasa*, TM-2002-21(June):1–37, 2002.

[211] J.D. Murphy, A. Giannattasio, Z. Yao, C.J.D. Hetherington, P.D. Nellist, and S.G. Roberts. The mechanical properties of tungsten grown by chemical vapour deposition. *Journal of Nuclear Materials*, 386-388:583–586, 2009.

[212] X. Tu, A. Shahba, J. Shen, and S. Ghosh. Microstructure and property based statistically equivalent RVEs for polycrystalline-polyphase aluminum alloys. *International Journal of Plasticity*, 115:268–292, 2018. ISSN 0749-6419. doi: 10.1016/J.IJPLAS.2018.12.002.

[213] M.A. Groeber and M.A. Jackson. DREAM.3D: a digital representation environment for the analysis of microstructure in 3d. *Integrating Materials and Manufacturing Innovation*, 3(1):5, dec 2014.

[214] Simmetrix Inc. - Mesh Generation, Geometry Access. URL http://www.simmetrix.com/.

[215] Claude A. Klein and Gregory F. Cardinale. Young's modulus and Poisson's ratio of CVD diamond. *Diamond and Related Materials*, 2(5-7):918–923, 1993.

[216] H. Zhang, B. E. Schuster, Q. Wei, and K. T. Ramesh. The design of accurate micro-compression experiments. *Scripta Materialia*, 54(2):181–186, 2006.

[217] Dassault Systèmes Simulia. Abaqus Unified FEA - SIMULIA™ by Dassault Sys-

tèmes®, 2018. URL https://www.3ds.com/products-services/simulia/products/abaqus/.

[218] R. Soler, J. M. Molina-Aldareguia, J. Segurado, J. Llorca, R. I. Merino, and V. M. Orera. Micropillar compression of LiF [111] single crystals: Effect of size, ion irradiation and misorientation. *International Journal of Plasticity*, 36: 50–63, 2012. ISSN 07496419. doi: 10.1016/j.ijplas.2012.03.005.

[219] M.P. Echlin, W.C. Lenthe, and T.M. Pollock. Three-dimensional sampling of material structure for property modeling and design. *Integrating Materials and Manufacturing Innovation*, 3:21, 2014. ISSN 2193-9764.

[220] M. Pinz, G. Weber, W. C. Lenthe, M. D. Uchic, T. M. Pollock, and S. Ghosh. Microstructure and property based statistically equivalent RVEs for intragranular γ-γ' microstructures of Ni-based superalloys. *Acta Materialia*, 157:245–258, 2018.

[221] A. Khorashadizadeh, D. Raabe, S. Zaefferer, G. S. Rohrer, A. D. Rollett, and M. Winning. Five-parameter grain boundary analysis by 3D EBSD of an ultra fine grained CuZr alloy processed by equal channel angular pressing. *Advanced Engineering Materials*, 13(4):237–244, 2011.

[222] M. A. Groeber, B. K. Haley, M. D. Uchic, D. M. Dimiduk, and S. Ghosh. 3D reconstruction and characterization of polycrystalline microstructures using a

FIB-SEM system. *Materials Characterization*, 57(4-5):259–273, 2006. ISSN 10445803. doi: 10.1016/j.matchar.2006.01.019.

[223] P. J. Konijnenberg, S. Zaefferer, and D. Raabe. Assessment of geometrically necessary dislocation levels derived by 3D EBSD. *Acta Materialia*, 99(15):402–414, 2015.

[224] G. Stechmann, S. Zaefferer, P. Konijnenberg, D. Raabe, C. Gretener, L. Kranz, J. Perrenoud, S. Buecheler, and A.N. Tiwari. 3-Dimensional microstructural characterization of CdTe absorber layers from CdTe/CdS thin film solar cells. *Solar Energy Materials and Solar Cells*, 151:66–80, 2016. ISSN 09270248. doi: 10.1016/j.solmat.2016.02.023.

[225] R. Thevamaran, O. Lawal, S. Yazdi, S.J. Jeon, J.H. Lee, and E.L. Thomas. Dynamic creation and evolution of gradient nanostructure in single-crystal metallic microcubes. *Science*, 354(6310):312–316, oct 2016.

[226] K.A. Nelson, G. Saini, M. Retsch, J.P. Singer, E.L. Thomas, J-H. Lee, D. Veysset, and T. Pezeril. High strain rate deformation of layered nanocomposites. *Nature Communications*, 3(1):1164, 2012.

[227] S. Zhao, B. Kad, C.E. Wehrenberg, B.A Remington, E.N. Hahn, Karren L More, M.A. Meyers, and B.A. Remington. Generating gradient germanium nanostructures by shock-induced amorphization and crystallization. *Proceedings of the National Academy of Sciences*, 114(37):9791–9796, 2017.

[228] A. Patra, T. Zhu, and D.L. McDowell. Constitutive equations for modeling non-Schmid effects in single crystal bcc-Fe at low and ambient temperatures. *International Journal of Plasticity*, 59:1–4, 2014.

[229] D. Cereceda, M. Diehl, F. Roters, D. Raabe, J.M. Perlado, and Jaime Marian. Unraveling the temperature dependence of the yield strength in single-crystal tungsten using atomistically-informed crystal plasticity calculations. *International Journal of Plasticity*, 78:242–265, 2016.

[230] S. Narayanan, D.L. McDowell, and T. Zhu. Crystal plasticity model for BCC iron atomistically informed by kinetics of correlated kinkpair nucleation on screw dislocation. *Journal of the Mechanics and Physics of Solids*, 65:54–68, 2014.

[231] L.P. Evers, W.A.M. Brekelmans, and M.G.D. Geers. Non-local crystal plasticity model with intrinsic SSD and GND effects. *Journal of the Mechanics and Physics of Solids*, 52(10):2379–2401, 2004.

Vita

Quan Jiao was born in Shenyang, China in 1988. He did his undergraduate studies at Dalian Jiaotong University and received a Bachelor of Science degree in Civil Engineering and Software Engineering in 2011. He subsequently pursued a master's degree in Computational Mechanics at Carnegie Mellon University (CMU) with Professor Jacobo Bielak. He subsequently joined Department of Mechanical Engineering at Johns Hopkins University (JHU) in Fall 2019 to purse a doctoral degree under the guidance of Professor Jaafar El-Awady. His Ph.D. research focuses on developing and utilizing small-scale testing experiments and computational methods to investigate the deformation behavior of of metallic materials at elevated temperatures.

VITA

List of Publications from this PhD work:

- Q. Jiao, G.-D. Sim, H. Fan, J.A. El-Awady. Micro-mechanical characterization of micro-architectured tungsten coatings. *Materials Science and Engineering A*, 705:366-375, 2017

- Q. Jiao, G.-D. Sim, M. Komarasamy, R.S. Mishra, P.K. Liaw, J.A. El-Awady. Thermo-mechanical response of single-phase face-centered-cubic AlxCoCrFeNi high-entropy alloy microcrystals. *Materials Research Letters*, 6(5):300-306, 2018

- Q. Jiao, J. Cheng, G.-D. Sim, S. Ghosh, J.A. El-Awady. In situ micro-mechanical characterization and multi-scale modeling of thermo-mechanical properties of micro-architectured tungsten coatings. *To be submitted.*

- X. Ma, Q. Jiao, L.J. Kecskes, J.A. El-Awady, T.P. Weihs. Effect of basal precipitates on pyramidal slip and tension twinning: microcompression and electron microscopy study of a Mg-Al binary alloy. *To be submitted.*